Friction in Wheel - Rail Contacts

Radu Popovici

This research was supported by the Dutch rail operator (NS) and the Dutch network infrastructure manager (ProRail).

De promotiecommissie is als volgt samengesteld:
prof.dr. F. Eising, Universiteit Twente, voorzitter en secretaris
prof.dr.ir. D.J. Schipper, Universiteit Twente, promotor
prof.dr.ir. A. de Boer, Universiteit Twente
prof.dr.ir. A.J. Huis in't Veld, Universiteit Twente
prof.dr.ir. S. Cretu, Universiteit Gh. Asachi, Roemenië
prof.dr.ir. P. De Baets, Universiteit Gent, België
dr.ir. A.H. van den Boogaard

Popovici, Radu Ionut
Friction in Wheel - Rail Contacts
ISBN 978-90-365-2957-0
Ph.D. Thesis, University of Twente, Enschede, The Netherlands
February 2010
Keywords: wheel - rail contact, mixed lubrication, friction model, Stribeck curve, traction curve, wheel - rail friction measurement.

Cover designed by Xiao Ma, Enschede

Printed by Wöhrmann Printing Service, Zutphen

FRICTION IN WHEEL - RAIL CONTACTS

PROEFSCHRIFT

ter verkrijging van
de graad van doctor aan de Universiteit Twente,
op gezag van de rector magnificus,
prof. dr. H. Brinksma,
volgens besluit van het College voor Promoties
in het openbaar te verdedigen
op vrijdag 19 februari 2010 om 15.00 uur

door

Radu Ionuţ Popovici
geboren op 13 oktober 1978
te Iaşi, Roemenie.

Dit proefschrift is goedgekeurd door de promotor:
prof.dr.ir. D.J. Schipper

in memoria bunicului, Barbu

Summary

In the autumn, railroad traffic is often interrupted due to the occurrence of slippery tracks. The Dutch main operator (NS) and the infrastructure manager (ProRail) struggle with repeated delays. The layer between wheel and rail causing this phenomenon has not yet been identified, but can be quantified by rheological properties determined by correlating the measured friction between wheel and rail and the developed friction model.

To this end, the research described in this thesis is twofold: theoretical; in which the wheel - rail contact is modelled in terms of contact and friction, and experimental; in which the friction between wheel and rail is measured to validate the developed model.

The contact model between wheel and rail is approximated to be elliptical, which is shown to be accurate for the described purpose. The low friction situation is assumed to be caused by an interfacial layer, which is acting like a lubricant.

Combining the previous two assumptions, a mixed lubrication friction model is developed for the Hertzian elliptical contact situation in which the interfacial layer is acting as a lubricant governed by the Eyring model. The mixed lubrication friction model results in the so-called Stribeck curve and/or the traction curve, which both take frictional heating and starved conditions into consideration. In addition, the changes in attack angle are also taken into account and a general viscoelastic model is proposed for both interfacial and boundary layers. In this way, most of the situations occurring in the wheel - rail contacts are covered, with the recommendation that future research should include the effect of spin.

The validation of the friction model was performed by conducting laboratory experiments on general elliptical contacts in the presence of a lubricant. Field experiments are conducted for extracting the rheological properties of the interfacial layer causing the low friction by using the presented model.

For the field experiments, two pioneer devices were developed and successfully used on the real track. One is a sliding sensor which measures the coefficient of friction between a curved shaped specimen pressed against and sliding along the rail, i.e. simple sliding conditions. A second device is developed and mounted on a train for measuring traction curves between a measuring wheel and the head (top) of the rail, i.e. rolling/sliding conditions, at velocities of up to 100 km/h. The measuring campaign was scheduled over 20 nights during the autumn of 2008 on three tracks of the Dutch rail network (Hoekselijn, Zeeuwselijn and Utrecht - Arnhem - Zwolle). Five characteristic traction curves were identified by the use of a statistical approach and rheological properties were extracted for the layer causing the low friction situation. Most of the approximately 6000 measured traction curves showed good agreement with the friction model, in which the

interfacial layer is represented by the Eyring behaviour. However, for some of them, viscoelasticity had to be taken into account.

Based on the results from the measuring campaign combined with the modelled wheel - rail friction model, conclusions were drawn and important recommendations made to both the Dutch train operator (NS) and the rail infra manager (ProRail) from theoretical and practical points of view.

Samenvatting

Gedurende de herfst wordt het treinverkeer vaak verstoord als het gevolg van gladde sporen. De Nederlandse Spoorwegen en de beheerder van de infrastructuur ProRail hebben daardoor problemen met herhaalde vertragingen. De samenstelling van de laag tussen treinwiel en spoorrails die ten grondslag ligt aan dit probleem is nog onbekend, maar kan met behulp van rheologische eigenschappen gekwantificeerd worden door de gemeten wrijving tussen wiel en spoor te correleren aan het ontwikkelde wrijvingsmodel.

Teneinde dit te bereiken is het onderzoek in dit proefschrift tweeledig: enerzijds theoretisch, waarbij het contact en de wrijving in het wiel-rail contact worden gemodelleerd, en anderzijds experimenteel, waarbij de wrijving tussen wiel en spoorrails wordt gemeten om het model te kunnen valideren.

Het contact tussen wiel en rail is bij benadering elliptisch, deze benadering is accuraat voor de beschreven toepassing. Het wordt aangenomen dat het optreden van lage wrijving veroorzaakt wordt door een grenslaag/tussenlaag tussen het wiel en de rail die zich gedraagt als een smeermiddel.

Door het combineren van deze twee aannames is een model ontwikkeld dat de gemengde smering en de wrijving in een elliptisch Hertz contact beschrijft, waarbij de tussenlaag zich gedraagt als een smeermiddel volgens Eyring. Dit gemengde smerings- en wrijvingsmodel resulteert in de zogenaamde Stribeck-curve en/of de tractie-curve, beide met inachtname van wrijvings geïnduceerde verhitting en schrale smeringscondities. Daarbij worden ook de veranderingen in wiel stand t.o.v. rail (hoek) acht genomen en wordt een visco-elastisch model voorgesteld voor zowel de interface als de grenslagen. Op deze manier wordt het merendeel van de optredende situaties in wiel-spoor contacten beschreven, met de aanbeveling dat toekomstig onderzoek de effecten van 'spin', of rotatie in het contact vlak, zou moeten meenemen.

Het wrijvingsmodel is gevalideerd met behulp van laboratorium experimenten aan algemeen elliptische contacten in de aanwezigheid van een smeermiddel. Daarnaast zijn veldtesten uitgevoerd om met behulp van het gepresenteerde model de rheologische eigenschappen van de tussenlaag, die resulteert in lage wrijving, te bepalen.

Voor de veldtesten zijn twee tribotesters ontwikkeld die succesvol zijn toegepast in het dagelijkse spoorbedrijf. De ene is een glijdende sensor die de wrijvingscoëfficiënt meet wanneer een gekromd proefstuk tegen het spoor wordt gedrukt, ofwel glijdende condities. Een tweede opstelling is ontworpen en gemonteerd op een trein voor het meten van tractiecurves tussen een meetwiel en de kop (bovenkant) van het spoor, resulterend in een combinatie van rollende en glijdende condities, met snelheden tot 100 kilometer per uur. De metingen werden

uitgevoerd gedurende een periode van 20 nachten in het najaar van 2008 op drie trajecten van het Nederlandse spoornet: de Hoekselijn, de Zeeuwselijn en de driehoek Utrecht - Arnhem - Zwolle. Met behulp van een statistische benadering zijn vijf karakteristieke tractiecurves geïdentificeerd, waarmee de rheologische eigenschappen van de tussenlaag die de lage wrijving veroorzaakt bepaald kunnen worden. Het meerendeel van de bij benadering 6000 tractiecurves vertoonde een goede overeenstemming met het wrijvingsmodel waarin de tussenlaag wordt beschreven met behulp van Eyring gedrag. Voor een enkele curves moest visco-elastisch gedrag ook in beschouwing genomen worden.

Gebaseerd op zowel de resultaten behaald gedurende de meetperiode als het model voor de wrijving in het wiel-rail contact zijn conclusies getrokken en belangrijke aanbevelingen gedaan aan de Nederlandse Spoorwegen en ProRail, zowel vanuit een theoretisch als een praktisch oogpunt.

Acknowledgements

As the project I worked on was very large, the number of people who I wish to thank is significant.

The root of any PhD research lies in the project proposal made by those who open the eyes of the people working in industry, convincing them of the importance of research. The two men who accomplished this in the case of my project are Frans Kokkeler and Dik Schipper. Thank you both, for giving me the chance to work for my doctoral degree on such an exciting topic.

The AdRem group was rather large and I shall first acknowledge the people from both NS and ProRail for the support they showed. Full credit must go to the project managers: to Marco Sala for his continuous challenges and to Marcel Vos for his genuine interest, but especially for answering the phone at 1:00 a.m. when we encountered a logistical problem, and to Frank Koster for being with us throughout these four years.

Thanks to Felix Chang, Erik Sikma and Robert van Ommeren for hosting all our meetings and for being the link with the railroad world. Special thanks go to Peter Paul Mittertreiner who was always willing to help and to share his experience and for being with us all the four years.

I shall not forget the colleagues within the projects, who I worked with side by side, and who were equally focused on the same task. They are: Oscar Arias-Cuevas, Niels van Steenis and Sander van der Krol. Thank you for easing our common tasks and for making our meetings friendlier.

Thanks to the two persons who opened the door into the field experiments: Ton Weel and Roland Bongenaar. They were the first who dared to actually attach one of our devices onto a locomotive running at 50 km/h and they did that after just two meetings. Thank you for that.

I shall move to the more extensive field measurements, and address thanks to Frans van Boekel and Rian de Jong for designing and building the tribometer we used for the real track measurements. I am grateful to Dietmar Serbée, for trusting in my concept and spending many white nights on our measurements. I am sure that if you had not taken on the task, no one else would. Thank you also to Marjan Schotsman, the only lady in our project, for fitting our measuring train through the night traffic.

I am grateful to Dik Schipper, my promoter, for his patience, for his countless good advice, for carefully reading my reports and especially for taking the pressure off my shoulders when it mounted up.

My gratitude goes also to Prof. Spiridon Cretu for making it possible for me to study at the University of Twente and for sharing his work with me. Also to Prof. Dumitru Olaru for the role he played in my education. Thank you.

The working environment in the tribology department goes beyond highest expectations and everyone should be jealous. This is all down to the people working there as permanent staff members: Belinda, Marc, Mathijn, Erik, Walter, Willie as well as the PhD colleagues: Noor, Rob, Gerrit, Ioan, Adeel, Mahdiar, Martijn, Dinesh, Ellen, Jamari and Jan Willem. Thank you all so much!

Special thanks to Xiao, who was able to let me down on several occasions without any remorse but still managed to be a good friend at the same time. I will definitely not remember our very interesting conversations. Also thanks for designing the beautiful cover of this thesis.

A huge thank you goes to Natalia for putting colours in our room and bringing the tribology group closer. I will definitely miss you next to my working desk. Thank you!

Table of contents

Nomenclature

a, b = half widths of the contact area (a in rolling, x, direction) [m]

A_C = real contact area [m^2]

A_{Ci} = contact area of pair i of asperities, $i = 1 \ldots N$ [m^2]

A_H = hydrodynamic area [m^2]

A_{nom} = nominal contact area (Hertz) [m^2]

B_c = width of the equivalent cylinder [m]

c_i = specific heat at constant temperature of body i, $i = 1,2$ [J/kg/K]

C = film thickness correction factor for frictional heating [-]

$D = \eta v^+ / (2aG')$ Deborah number [-]

E' = combined elasticity modulus [Pa]

$E(m)$ = elliptical integral of the first kind of modulus m [-]

f = coefficient of friction [-]

f_C = coefficient of friction in BL [-]

F_C = load carried by asperities [N]

F_f = friction force [N]

F_H = load carried by lubricant [N]

F_N = total normal load [N]

$F_{f,\,BL}$ = friction force in the contacting asperities [N]

$F_{f,\,EHL}$ = friction force in the lubricant [N]

$F_{f,\,ML}$ = friction force in ML regime [N]

$G = \alpha E'$ dimensionless lubricant number [-]

G' = shear modulus of the lubricant [Pa]

G_C' = shear modulus of the boundary layer [Pa]

h = film thickness [m]

$\overline{h} = h / R_x$ dimensionless film thickness [-]

h_C = thickness of the boundary layer [m]

h_s = separation [m]

h_c = central film thickness [m]

$H = \overline{h} U_\Sigma^{-1/2}$ dimensionless film thickness [-]

H_{oil} = dimensionless oil inlet thickness [-]

H_{Cff} = dimensionless film thickness in fully flooded conditions [-]

H_{C0^o} = film thickness for the entrance angle of 0º, [-]
H_{C90^o} = film thickness for the entrance angle of 90º, [-]
k_i = diffusivity of body i, i = 1,2 [m^2/s]
K_i = thermal conductivity of body i, i = 1,2 [W/m/K]
K_{eff} = effective thermal conductivity [W/m/K]
K_{lub} = thermal conductivity of the lubricant [W/m/K]
$K(m)$ = elliptical integral of the second kind of modulus m [-]
$L = GU_{\Sigma}^{1/4}$ lubricant number [-]
$M = WU_{\Sigma}^{-3/4}$ load number [-]
n = rheological index [-]
$\overline{n}$ = density of asperities [m^{-2}]
N = number of contacting asperities [-]
p = pressure [Pa]
p_0 = maximum Hertzian pressure [Pa]
p_0^* = reference pressure for τ_0 [Pa]
p_a = ambient pressure [Pa]
p_{Ci} = contact pressure with pair i of asperities, $i = 1 \ldots N$ [Pa]
p_{NH} = maximum contact pressure (Non-Hertzian) [Pa]
p_m = mean contact pressure [Pa]
P_C = pressure carried by asperities [Pa]
P_H = pressure carried by lubricant [Pa]
P_N = pressure exerted by the normal load [Pa]
p_r = constant $\left(p_r = 1.962 \times 10^8\right)$ [Pa]
p_e = Peclet number ratio [-]
P_{ei} = Peclet number of body i, i = 1,2
Q_F = rate of heat flow [W]
$r' = H_{oil}/H_{cff}$ relative oil supply thickness [-]
R_c = radius of the equivalent cylinder [m]
R_{ij} = radius of body i in j direction, i = 1,2 and j = x(rolling),y [m]
R_x = combined radius in x (rolling/sliding) direction [m]
R_y = combined radius in y direction [m]
R_{wy} = wheel profile curvature (y direction) [m]

R_{ry} = rail profile curvature (y direction) [m]

$\Re$ = Chevalier film thickness reduction factor (starvation) [-]

S_0 = viscosity - temperature index [-]

$S = 2v^{dif}/v^{+}$ slip [-]

$S_{\Phi} = 2v_{\Phi}^{dif}/v_{\Phi}^{+}$ slip including the attack angle Φ [-]

S_{ep} = slip at the transition from elastic to plastic behaviour of the boundary layer [-]

t = transit time of the lubricant through the contact area [s]

T = temperature [°C]

T_i = oil inlet temperature [°C]

T_f = oil temperature within the contact [°C]

Q = Thermal load parameter

$U = v^{+}/2$ mean rolling velocity [m/s]

$U_{\Sigma} = \eta_0 v^{+}/(E' R_x)$ dimensionless velocity number [-]

v_0^{*} = reference velocity for τ_0 [m/s]

v_i = velocity of body i, i = 1,2 [m/s]

$v^{+} = v_1 + v_2$ sum velocity [m/s]

$v^{dif} = |v_1 - v_2|$ sliding velocity [m/s]

v_{Φ}^{+} = sum velocity when the attack angle is Φ [m/s]

v_{Φ}^{dif} = sliding velocity when the attack angle is Φ [m/s]

$W = F_N/(E' R_x^2)$ dimensionless load number [-]

$x^{+} = a\sqrt{1-(y/b)^2}$ maximum x coordinate which a point inside the contact ellipse can have for a given y [m]

$X^{+} = x^{+}/a$ dimensionless maximum x coordinate which a point inside the contact ellipse can have for a given y [m]

z = viscosity - pressure index [-]

Greek symbols

α = viscosity - pressure coefficient [Pa^{-1}]

$tg(\alpha_v)$ = slope of the Eyring shear stress function of velocity [-]

$tg(\alpha_p)$ = slope of the Eyring shear stress function of pressure [-]

$tg(\alpha_0)$ = slope of the traction curve at zero slip [-]

β = average radius of asperities [m]

β_0 = temperature coefficient of viscosity [K^{-1}]

γ = parameter in the reduction film factor of Chevalier, $\Re$ (starvation) [-]

$\dot{\gamma} = \dot{\gamma} = v^{dif}/h$ shear rate [1/s]

$\dot{\gamma}_\Phi = v_\Phi^{dif}/h$ shear rate at attack angle Φ [1/s]

η = viscosity [Pa·s]

η_0 = viscosity at ambient pressure [Pa·s]

η_i = oil inlet viscosity [Pa·s]

η_∞ = constant ($\eta_\infty = 6.315\times10^{-5}$) [Pa·s]

$\kappa = a/b$ ratio of the contact ellipse, a in x (rolling) direction [-]

$\phi = b/a = 1/\kappa$ ratio of contact ellipse (Bos), a in x (rolling) direction [-]

Φ = attack angle [º]

φ_i = angle between the principal direction x of the contact ellipse and the rolling body i, i = 1,2 [º]

σ = standard deviation of surface [m]

σ_s = standard deviation of asperities [m]

τ = shear stress [Pa]

τ_0 = Eyring shear stress [Pa]

τ_{0C} = Eyring shear stress of the boundary layer [Pa]

τ_C = shear stress of the boundary layer [Pa]

τ_{Ci} = shear stress of the boundary layer between pair i of asperities, i = 1…N [Pa]

τ_L = Limiting shear stress [Pa]

$\bar{\tau} = \tau/\tau_{0,L}$ dimensionless shear stress [-]

τ_0^* = reference shear stress [Pa]

τ_H = shear stress of the lubricant [Pa]

θ_i = dimensionless flash temperature of body i [-]

θ = angle between the lubricant entrance vector and the minor axis of the contact ellipse [º]

ρ = density [kg/m^3]

ρ_i = density of body i, i = 1,2 [kg/m^3]

ξ = $\eta_0 \dot{\gamma} / \tau_{0,L}$ dimensionless parameter [-]

$\gamma_{1,2}$ = Johnson's factors [-]

ϑ = R_x / R_y ratio of the reduced radius of curvatures [-]

Abbreviations

BL = Boundary Lubrication

ML = Mixed Lubrication

EHL = Elasto Hydrodynamic Lubrication

RI = Rigid/Isoviscous asymptote

EI = Elastic/Isoviscous asymptote

RP = Rigid/Piesoviscous asymptote

EP = Elastic/Piesoviscous asymptote

Chapter 1

Slippery tracks

Each year sees an increase in rail traffic across the globe. As a direct consequence, the acceleration and braking demands of the rail vehicles also increase significantly. This means a shorter braking distance and higher acceleration in order to travel at cruising velocity for longer distances as are possible. Of course, this has caused drivers to experience the limitations of the wheel - rail traction capabilities more frequently.

The friction between wheel and rail has a major impact on maintenance and logistics because it determines the wheel and rail wear, in case it is too high, and reduces the ability to brake and to accelerate properly, in case friction is too low. The wear and the traction are the most important aspects from an economic perspective. However, the security point of view in which the friction levels are very low, with the result that a train might not be able to brake within the available distance, is of even higher importance. The optimum balance still has to be found between the lower limit, which assures a low wear of both wheel and rail and the higher one, which makes fast accelerations possible and, subsequently, accurate timetables. But the low friction situation in which the braking manoeuvre is failing represents the highest priority in the railroad industry of today: it is a security issue.

What are the factors that determine low friction, when this occurs and where, and how can measures be taken to counteract it? These are questions that still need answers and this thesis is meant to assist engineers in finding them.

1.1 Side effects

Extremely low friction values between the wheel and the rail are reported worldwide, leading to severe delays and sometimes even to accidents. The United

Kingdom alone reports losses due to low friction amounting to roughly 50 million British Pounds a year [1]. In the Netherlands, the problem went so far that in the autumn of 2002 slippery tracks caused an almost complete failure of train services. An important part of the rolling stock of the Dutch train operator (NS-Reizigers) suffered flat wheels due to excessive sliding, leaving thousands of travellers stranded overnight on their way home. In the following week, thorough maintenance was carried out on the rolling stock, but the lack of available rolling stock made it impossible for the operator to run on schedule in the ensuing week.

In general, on a larger scale, low friction is a very nasty phenomenon to happen on the railroads. Another side effect is the behaviour of the driver. Because it is up to the drivers, and because they shoulder great responsibility, drivers tend to be overly cautious on the base of their "feeling" concerning the condition of the track. When one driver encounters a slippery track during braking or accelerating, he will immediately communicate to other drivers that they ought to exert caution. Of course, such behaviour is 'over-safe' when the friction levels are at acceptable limits, leading undoubtedly to delays.

1.2 Interfacial layer

Slippery tracks occur at specific times of the year, especially during autumn, when correlated with different reasons (more rain, lower temperatures, high humidity etc.). The interfacial layer is thought to consist of fallen leaves (so-called "black layer"), water, rust, microbacterial growth, industrial pollution, etc. [2]. Of course, knowing the consistency would significantly increase the effectiveness of measures to tackle the problem, but since the interfacial layer is still not clearly quantified, a rheological approach would be more appropriate. So the assumption is that the interfacial layer is acting as a lubricant. This assumption stands because, as is well known, lubricants have the property of reducing friction.

Following such an approach the behaviour of the interfacial layer can be described by making use of one of the available shear models used in lubricated tribo-systems. For the situation in which the friction is low, it is considered to be caused by shearing the interfacial layer solely.

1.3 Mitigation

Nowadays, there is still no solution found to overcome the problem caused by low friction (slippery tracks). But investigations have been conducted going back more than 150 years. The most common solution used till today has been to spread sand at the front of the wheel-rail contact (Fig. 1.1). Of course, the lasting effect of sand is small and due to the air flow underneath the train, only part of the sand actually reaches the contact [1]. Sand also increases the risk of rail insulation, resulting in a dangerous situation in which a train cannot be detected by the signalling equipment [1, 3].

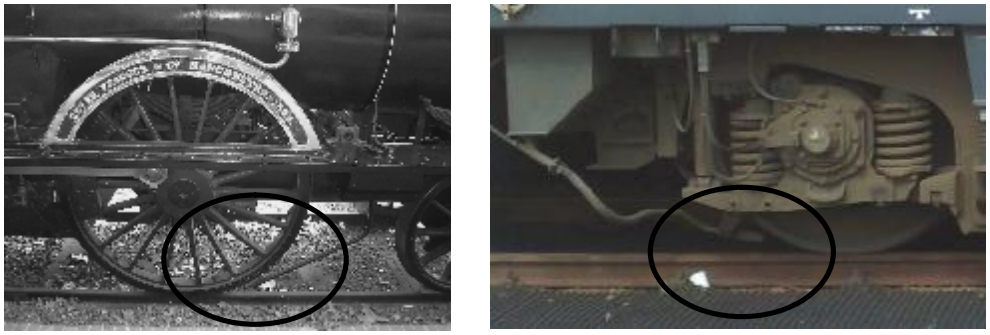

Fig. 1.1 Sand spreader mounted on Type 4.4.0 steam locomotive 1862 (left) and Class 1700 electric locomotive 1990 (right).

To overcome these issues, the sand is often mixed with metal particles and is delivered by a gel paste, the final mixture being referred as “Sandite” [4]. Other so-called VHPF (Very High Positive Friction) modifiers [5] are under development and may in the future be put to use. These can be applied on to the rail by track side applicators (Fig. 1.2) [6]. Other proactive solutions include cleaning the rail by, for example, high pressure water jetting (Fig. 1.3) [1].

Fig. 1.2 Track side applicator of friction modifier.

Fig. 1.3 High pressure water jetting.

More severe methods include vegetation management, i.e. cutting down the trees along the tracks, which is to be avoided due to its environmental impact.

The brakes on new modern rolling stock incorporates Wheel Slide Protection (WSP) systems, by which the slip during braking is controlled in such way it prevents the wheel from freezing (not rotating) while the train still moves, so it prevents the formation of flats on wheels ("square wheels") [7]. A similar system is also through equipping the traction control of the motor, to prevent high slip during traction and subsequently severe wear to wheel and rail.

1.4 Theoretical solutions

Measures taken against the low friction problem mainly focus on "trial and error" experiments [1], because there is no friction model available for the wheel - rail contact. Such model should contain rheological properties of the interfacial layer as well as the operational conditions of the wheel-rail tribo-system, i.e. train velocity, slip between wheel and rail, attack angle, wheel and rail profiles (or local contact radii), surface topography of wheel and rail, etc.

Prior to understanding the mechanisms involved in the friction between wheel and rail, the contact between wheel and rail has to be known, which is complex due to the elastic deforming the contacting profiles. Finding the contact area and pressure distribution requires complex programming and long computing time.

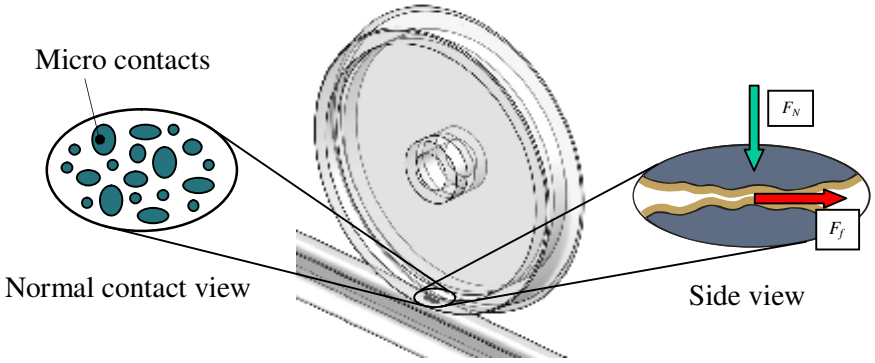

Fig. 1.4 Wheel-rail contact and friction.

The contact can be approximated by an elliptical Hertzian contact (see chapter 2), and will be used in this thesis.

At microscopic scale, the two contacting bodies (wheel running band and top of the rail) are rough and contact take place on roughness level and can be calculated based on a deterministic microcontact model. As stated earlier, the wheel - rail contact is considered to be "lubricated" for the low friction case so the friction force is to be calculated by using adequate shear models for the interfacial layer present in the microcontacts and remaining macrocontact.

Wheel - rail contacts are sliding/rolling contacts (Fig. 1.5), meaning that the peripheral velocity of the wheel is comparable within limits with the total velocity of the train.

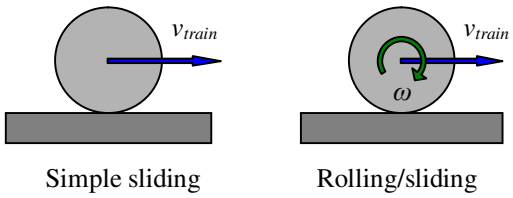

Fig. 1.5 Rolling/sliding wheel - rail contact.

From pure rolling ($v_{train} = v_{wheel}$) to simple sliding ($v_{wheel} = 0$ and $v_{train} \neq 0$) the coefficient of friction between the wheel and the rail would increase from zero (pure rolling) up to a friction value caused by shearing corresponding to the considered lubrication situation. Such variation represents the so-called traction curve. Other dependency of the coefficient of friction is given by varying the rolling velocity between the wheel and the rail. With increasing the velocity, the

coefficient of friction decreases due to lift-off of the wheel because of pressure built up in the interfacial layer. This variation, i.e. coefficient of friction as a function of sum velocity, is the so-called Stribeck curve.

Apart from the theoretical modelling of the friction between wheel and rail, equally substantial insight is given by directly measuring the friction between a contacting probe and the counterpart (wheel and top of rail). Such equipment is of use to validate a friction model.

1.5 Aim of thesis

With a focus on two directions, theoretical and experimental, this thesis will describe the frictional behaviour of the “lubricated” wheel - rail contact on the assumption that the contact is Hertzian and elliptical, chapter 2.

A friction model is developed and will predict the coefficient of friction between wheel and rail as a function of sum velocity (Stribeck curve), slip and attack angle (Traction curve), interfacial layer supply thickness (starvation model) and will also include frictional heating, chapter 3.

Experimentally, results of laboratory experiments will be shown for validating the general friction model for elliptical contacts in the presence of a mineral oil and/or grease, chapter 4.

For validating the model for the wheel - rail contact situation, field measurements are required. For this purpose, two train-borne tribometers are designed and are described in detail as well as their performance and measurement results, chapter 5.

Findings of both model and measurements are discussed and based on these findings, the train operator and network manager will be given advice, in order to take measures when low friction (slippery tracks) is present, chapter 6 and 7.

Chapter 2

Background

This work will apply the lubrication theories to the wheel - rail contact. As will be shown further, lubricated contacts are studied for simple defined geometries of the bodies in contact (flats, cylinders, ellipsoids, balls or combinations of these) giving relatively simple contact areas (line, point or ellipse) when they are pressed against each other. In practice, such contacts are encountered in ball bearings, gears, plain or journal bearings, piston rings - cylinder assemblies, etc. On the other hand, wheel - rail contacts are not such a simple shape, so the modelling of friction in such lubricated contact is more complex.

2.1 Wheel - rail contact models

The wheel - rail contact was mainly of interest for the vehicle system dynamic problems. In this respect, the contact forces along and perpendicular to the rolling direction are of maximum interest. This problem was first solved by Carter [8] by regarding the wheel - rail contact as a cylinder rolling over a plane (a two-dimensional problem). Three decades later, de Pater and Johnson solved the spherical (three-dimensional) case by using the Hertz solution for predicting the shape and size of the contact area and pressure distribution. For the complete formulation, the reader is referred to [9]. More approximate solutions for the elliptical contact situation were presented by Haines and Ollerton [10] followed shortly by Vermeulen and Johnson [11].

Apart from the approximated solutions, the general case for modelling the wheel - rail contact must be solved numerically. Kalker [12] was the first to solve the general wheel - rail contact, for which purpose he developed the program CONTACT. The program is widespread and even today it is most frequently used

for the wheel - rail contact problem. For vehicle dynamics problems, where the external contact parameters change continuously, i.e. lateral position between wheel and rail profiles, normal load, attack angle, the program CONTACT cannot be used due to the high computational time. To overcome this, Kalker proposed an approximate elastic deformation based contact model for the contacting bodies called FASTSIM [13]. A survey of these methods is made in [14].

Finite element methods are also applied to the wheel - rail contact problem and significant simulations and developments have been recently made [15].

The state-of-the-art papers of Knothe et al. [16] and Piotrowski and Chollet [17] discuss in more detail the above methods of contact mechanics applicable for wheel - rail contact.

2.1.1 Non-Hertzian elastic contact

More recent work on the elastic non-Hertzian contact was made by Cretu [18] who solved the contact between two randomly shaped bodies described as half spaces by using the Papkovici - Boussinesq solution. The developed numerical program is called NON-HERTZ and its solving algorithm uses the Conjugate Gradient Method using the Discrete Convolution with the process of zero padding and wrap-around order associated with FFT for regarding the displacement as a convolution of pressure with elastic response. The inputs are: separation between the two bodies, normal load, material properties, coefficient of friction in the principal direction and surface roughness. This model is used to study the contact between the wheel and the rail for different lateral shifts of the wheelset relative to the track.

The two considered counterparts are a S1002 wheel profile and a UIC60 rail. The wheel has a radius in rolling direction of 460 mm and the rail is inclined at 1/40. The inner gauge of the wheelset is 1360 mm and the track gauge is standard, i.e. 1435 mm. The definitions of the standard profiles and some other parameters related to the wheel - rail contact setup are given in Appendix F.

When the wheelset is in perfect alignment with the track, the above dimensions would result in a lateral shift between the left wheel and rail of 3 mm. Of course, during train movement, the wheelset changes its relative position to the rail. Considering different lateral shifts between the wheelset and the track, the contact point positions in both rail and wheel coordinates were determined, as well as the radii of curvature of both profiles in the contact points (Table 2.1 and Fig. 2.1).

In Table 2.1, Δy is the lateral shift of wheelset relative to the track and Δy_r is the lateral position of the wheel relative to the rail. y_{CR} is the lateral coordinate of the contact point in rail coordinates and y_{CW} the lateral coordinate of the contact point in wheel coordinates. And the important radii of curvature at the contact point location: R_{wy} is the wheel curvature, R_{ry} is the rail curvature and R_y is the equivalent profile curvature.

Table 2.1: Input contact parameters for the wheel - rail contact. All dimensions in mm.

Δy	Δy_R	y_{CR}	y_{CW}	R_{wy}	R_{ry}	R_y
3	6.063	-4.21	-7.21	-890	300	452
2	5.063	-3.55	-5.55	-655	300	553
1	4.063	-2.44	-3.44	-506	300	736
0	3.063	-0.28	-0.28	-390	300	1294
-1	2.063	11.33	12.33	-199	80	132
-2	1.063	12.05	14.05	-180	80	141
-3	0.063	12.92	15.92	-160	80	156
-4	-0.937	14.045	18.05	-138	80	182
-5	-1.937	15.755	20.76	-112	80	260

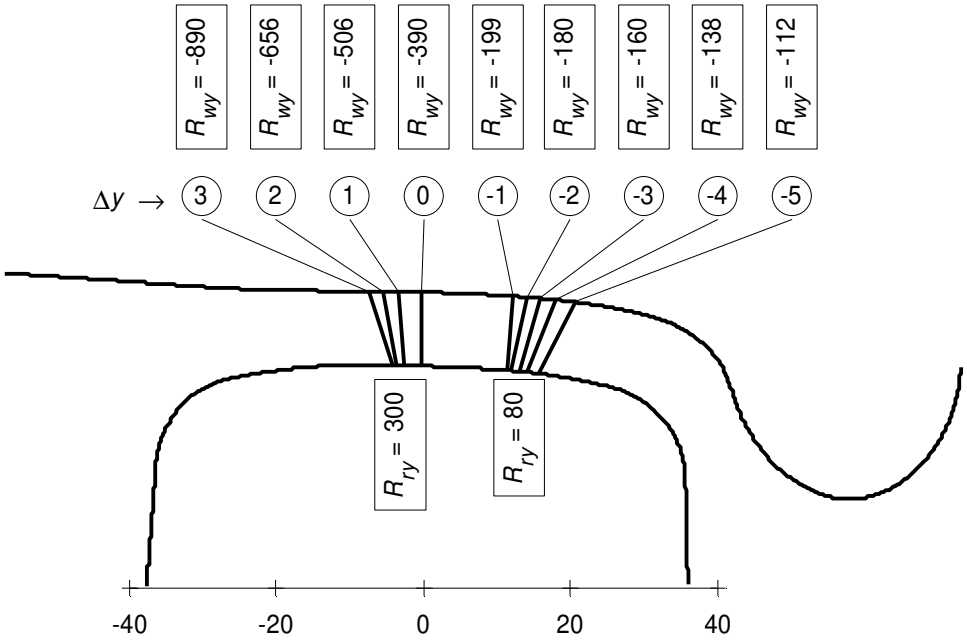

Fig. 2.1 Contact point positions and profile curvatures for different lateral shifts of the wheelset relative to the track, values in mm.

The contact point position was determined by simply calculating the minimum distance between the profiles in vertical direction. The curvature of the profile was calculated using the coordinate of the contacting point and two neighbours in its close proximity (Eq. 2.1).

$$R_{wy,ry} = -\frac{d_y^{\,2}}{z_{i-1} - 2 \cdot z_i + z_{i+1}} \tag{2.1}$$

Where, d_y is the distance in lateral y-axis between the contact point and one of its considered neighbours, z_i is the z-coordinate of the contact point and z_{i-1}, z_{i+1} are the z-coordinates of the neighbours (Fig. 2.2).

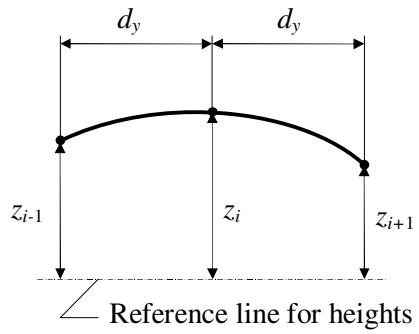

Fig. 2.2 Calculation of curvature at the contact point.

The curvatures can also be calculated using the second derivative of the polynomial description of the profiles. Once these are determined for every considered lateral shift of the wheelset between +3 (right) and -5 (left), the Hertz formulas were used to determine the semi-axes of the contact ellipse and the contact pressure. For the same contact position, using the polynomial description of the profiles, an estimated target domain was meshed and the separation matrix was used as input into the NON-HERTZ code. The results for the left wheel - rail pair are visualized in Fig. 2.3 and values summarized in Table 2.2.

Table 2.2: Results for wheel - rail contact with Hertz and the code NON-HERTZ [18].

Δy	a [mm]	b [mm]	p_0 [MPa]	p_{NH} [MPa]
3	6.5	6.4	1028	1030
2	6.3	7.1	961	964
1	6.0	8.2	879	873
0	5.4	10.7	746	932
-1	7.8	3.4	1617	1261
-2	7.7	3.5	1574	1449
-3	7.6	3.7	1515	1494
-4	7.4	4.1	1425	1425
-5	7.1	4.9	1246	2364

In Table 2.2, the values a, b represent the semi-axes of the contact ellipse along and perpendicular to the rolling direction, p_0 is the maximum Hertzian contact pressure and p_{NH} is the maximum contact pressure from the NON-HERTZ program.

From Fig. 2.3, one immediately may see that, in some of the positions, the contact area calculated with the numerical code is almost identical with the one predicted by the Hertz theory. Also, the maximum contact pressures are basically identical for the positions 3, 2, 1, -3 and -4 with errors of maximal 1.5% in maximum pressure. In cases where the wheelset is shifted by -2 mm relative to the track, give also a good correlation between the two methods in terms of pressure, with errors of less than 10%.

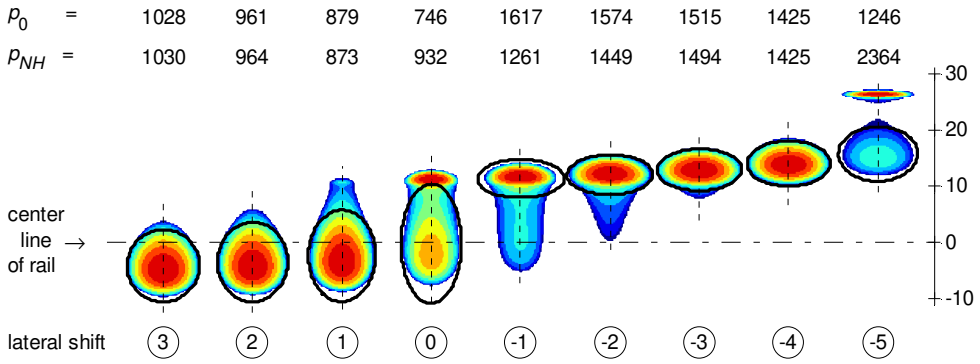

Fig. 2.3 Contact area and pressure distribution of left wheel - rail pair for different lateral shift of the wheelset relative to the rail using the Hertz theory (indicated with the ellipse) and the code NON-HERTZ [18].

A shift of the wheelset by -5 mm to the left would result in a secondary distinctive contact area between the wheel flange and the gauge part of the rail. Because this secondary contact area (on the flange side) is making a significant angle with the horizontal plane, spin in the contact becomes very important with respect to friction modelling. This case will not be discussed in this thesis.

The remaining contact situations to be discussed from Fig. 2.3 are 0 and -1 lateral shift of the wheelset. The contact areas are not Hertzian because of secondary contact points which appear due to the elastic deformation of the two bodies in contact. It is concluded, just by visualizing Fig. 2.3, that the real contact area (predicted by the NON-HERTZ code) is different than the contact ellipse (predicted by Hertz formulas) when the last one is calculated at the contact point considering the local radii of curvature.

Apart from these two and the -5 mm shift cases, the Hertz theory gives very good approximation of the real contact area and the contact between wheel and rail is to be considered as an elliptical one without any fitting of the contact area with an

equivalent ellipse but by predicting the contact ellipse at those contact points considering the local curvatures of both profiles.

The next section deals with establishing the parameters of an equivalent Hertzian contact for the contact situations "0" and "-1".

2.1.2 Equivalent elliptical contact

As previously shown, when a train runs in perfect alignment with the track, the contact area is non-Hertzian. Numerical calculations using the program NON-HERTZ of Cretu [18] predicts the contact area and pressure distribution as shown in Fig. 2.4 (c). The same inputs as in the previous section were also used here, i.e. wheelset of S1002 wheels of 460 mm in diameter, with the inner gauge of 1360 mm rolling over track of UIC60 rails inclined at 1/40, with the standard gauge of 1435 mm, see Fig. 2.4 a.

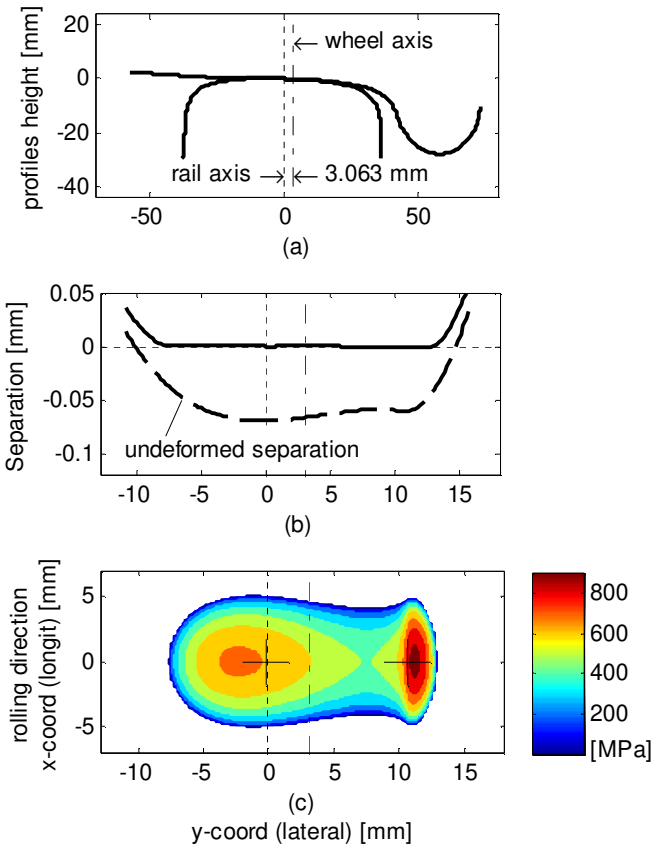

Fig. 2.4 Two contact point situation, when the wheelset is in perfect alignment with the track: (a) wheel and rail profile position, (b) profile separation and (c) contact area and pressure distribution.

Fig. 2.4 (b) clearly shows a secondary minimum in the separation at approximately 11 mm from the primary contact point resulting in the calculated pressure distribution Fig. 2.4 (c).

2.1.2.1 Contact area as a pair of equivalent ellipses

Without making use of such numerical code as NON-HERTZ or CONTACT, Sauvage made a first estimation of the contact area by estimating it with a pair of equivalent ellipses (work not published but mentioned by Pascal and Sauvage [19] and Piotrowski and Chollet [17]). The existence of a secondary contact point was determined by subtracting the penetration/deformation from the profiles. If the new minimum approach between the adjusted profile is at a different location than the main contact point coordinate, then the contact area can be approximated with two contact ellipses (Fig. 2.5).

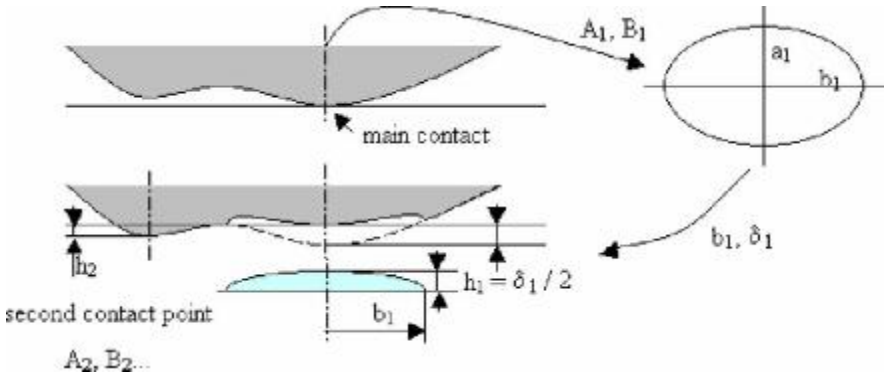

Fig. 2.5 Determination of secondary contact point using Sauvage's method. Reproduced from [17].

The penetration can be either geometrical (from the profiles), Hertzian or Boussinesq deformation. Further, the two contacting ellipses are determined by using the Hertzian theory locally as will be shown further to the case in Fig. 2.4 used here as an example.

Considering the two proximities as independent of each other, two Hertzian problems were solved simultaneously by loading simultaneously the two contacts with a total normal load as used in the numerical code. The equivalent situation is schematically presented in Fig. 2.6.

The problem was solved iteratively by modifying the total approach between the two bodies until the summation between the forces F_1 and F_2 produced by the individual indentations, δ_1 and δ_2, becomes equal with F_N.

$$F_N = F_1(\delta_1) + F_2(\delta_2) \tag{2.2}$$

where, $F_i(\delta_i)$ is the load necessary to create the indentation δ_i at the contact point

$i,\ i=1,2$. Eq. 2.3 is derived from the Hertz formula for calculating the indentation of an elliptical contact (Eq. E.3, Appendix E).

$$F_i(\delta_i)=\sqrt{\frac{8\cdot R_e\cdot E'^2}{9}\left(\frac{\delta_i}{\delta^*}\right)^3} \tag{2.3}$$

Where, δ^* is given by Eq. E.9, Appendix E.

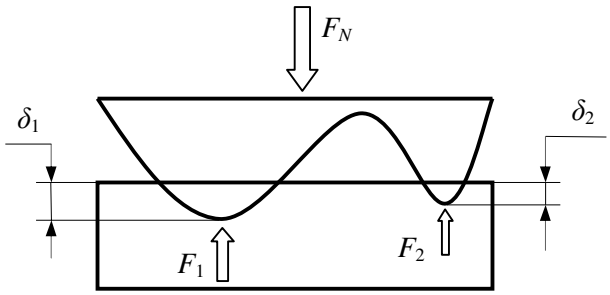

Fig. 2.6 Scheme of the two contact point situation solved with Hertz formulas.

Results for the practical problem of the wheelset in perfect alignment with the track are shown in Table 2.3 and the calculated contact ellipses are plotted in Fig. 2.7.

Table 2.3: Contact ellipses calculated for the two contact points and equivalent situations, for the example given in Fig. 2.4.

Contact point	y (coord.) [mm]	F_i [kN]	Ry [mm]	a [mm]	b [mm]	δ [mm]	p_0 [MPa]
1	-0.22	62.5	1295	4.78	9.43	0.06	661
2	10.67	27.5	126	5.27	2.24	0.05	1113
e	3.12	90.0	-	6.16	9.24	-	755

2.1.2.2 The equivalent ellipse

To simplify the contact area even more, Pascal and Sauvage [20], used a method to calculate only one equivalent contact ellipse at the wheelset central position by which the ratio of the equivalent ellipse is the weighted mean of the ratios of the two ellipses which approximates the real contact.

$$\kappa_e=\frac{\kappa_1 F_1+\kappa_2 F_2}{F_1+F_2} \tag{2.4}$$

Where $\kappa_i=a_i/b_i$ is the ratio of the ellipse $i,\ i=1,2,e$. From the load balance, Eq. 2.2, shows that the area of equivalent ellipse has to be equal with the summation of

the two areas calculated at the two contacting points:

$$\pi \cdot a_e b_e = A_{Hz1} + A_{Hz2} \tag{2.5}$$

And from the last two Eq. 2.4 and 2.5, the semi-axes of the equivalent contact ellipse are determined as:

$$a_e = \sqrt{\kappa_e \left(a_1 b_1 + a_2 b_2\right)} \quad \text{and} \quad b_e = \frac{a_e}{\kappa_e} \tag{2.6}$$

The coordinate of the equivalent ellipse, y_e, is calculated here as the weighted mean of the coordinates of the two contact points [20]:

$$y_e = \frac{y_1 F_1 + y_2 F_2}{F_1 + F_2} \tag{2.7}$$

The calculated equivalent ellipse from the example in Fig. 2.4 is visualized in Fig. 2.7 and the values are given in Table 2.3. The results are similar to the ones in [21].

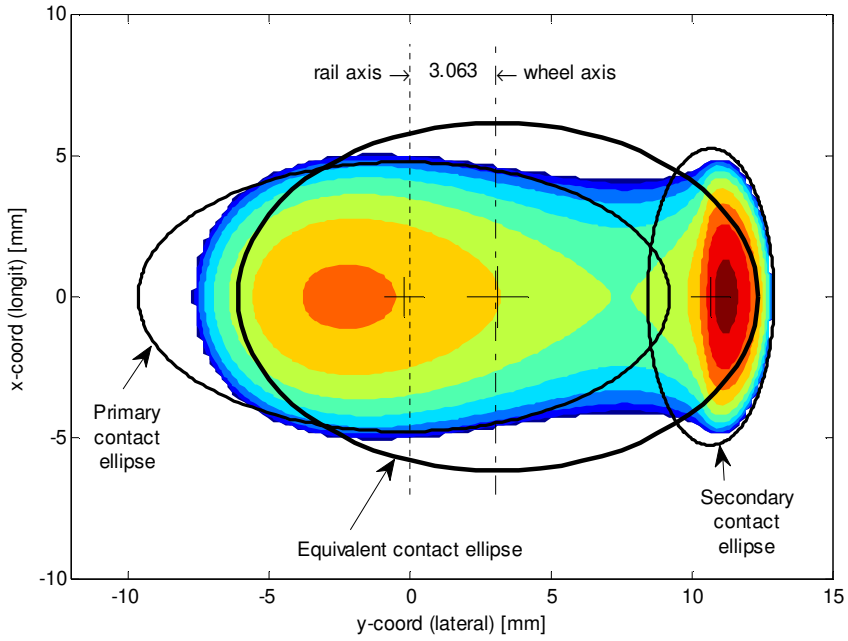

Fig. 2.7 Equivalent contact ellipse for the wheelset positioned in the centre of the track, see Fig. 2.4.

2.1.2.3 Other approximations

A wheel - rail contact model is mainly used for vehicle dynamic simulation problems. In such calculations, the contact parameters, i.e. normal load, lateral shift, attack angle, etc., change every step of the simulation. So a numerical contact model as CONTACT and NON-HERTZ would increase the computational time significantly. To overcome this situation, accurate analytical contact models were developed by, for instance, Arnold et al. [22] and Ayasse et al. [23] to approximate the contact area by using the Hertzian theory.

Since in the present work, the interest in the wheel - rail contact is establishing a relation between the non-Hertzian and elliptical Hertzian contact problems, these models will not be detailed further, the ones mentioned in the previous two sections give enough insight into the phenomenon.

2.1.3 Conclusions on the contact models

Based on the existing wheel - rail contact models, described in this section, it is concluded that the equivalent elliptical contact gives a good approximation for the real case, as long as no flange contact occurs between wheel and rail. Therefore, the friction model for the wheel - rail contact will be developed for the elliptical contact situations.

2.2 Wheel - rail friction models

Accurate estimation of wheel - rail friction levels is of extreme importance in train simulations. The software programs for vehicle dynamic simulations use built-in friction data based on optimum conditions, i.e. the tracks are dry, so the train makes use of its maximum power during acceleration. Timetables are built on these kinds of programs.

The available friction models applicable to the wheel - rail contact situation are described in the next subsections.

2.2.1 Friction in dry contacts

The friction force between two bodies in contact during sliding is defined as the lateral applied force necessary to maintain constant motion. The coefficient of friction is defined as the friction force divided by the normal force which loads the system. Friction in dry contacts takes place at micro level and is generated in the microcontacts of surface roughness. In simple sliding tribo-systems the coefficient of friction is often referred to as Coulomb type.

In rolling/sliding contacts, i.e. wheel - rail, the coefficient of friction is not of Coulomb type anymore and a more complex modelling is required due to so-called adhesion and interfacial slip regions which appear in the contact area (Fig. 2.8).

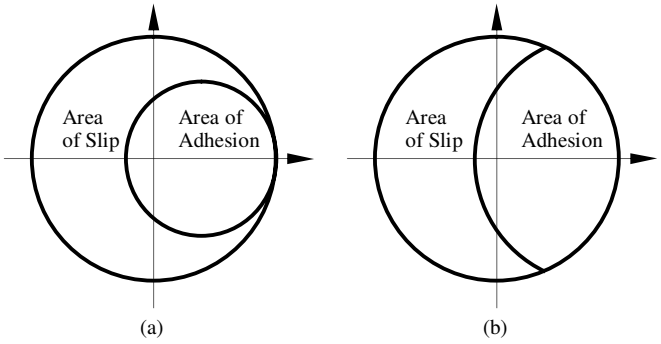

Fig. 2.8 Division of the contact area (adhesion and slip) of a rolling/sliding contact after (a) Kalker [24] and (b) Haines and Ollerton [10].

Such models require numerical computation over the meshed contact area and the first applicable to wheel - rail contacts was developed in 1966 by Kalker [24]. These models evolved over time ending with the numerical evaluation of the coefficient of friction as a function of material properties and load by Popov et al. [25] and recent multiscale simulations of Bucher et al. [26].

2.2.2 Friction in contaminated contacts

Friction models for lubricated contacts are found more often in the literature. The pioneer of the full film lubrication was Reynolds 1886 [27] who described the relation between the film shape and the pressure distribution as a function of viscosity of the lubricant (contaminant) and sum velocity between the contacting bodies. Then Stribeck [28] described the influence of the velocity and load between the contacting surfaces for plain and roller bearings. Based on his findings, researchers [29] concluded that for lubricated contacts, three lubrication regimes can be distinguished (Fig. 2.9): the boundary lubrication (BL) regime, at low velocity the load is carried solely by interacting asperities of the opposing surfaces and friction is controlled by shearing the surface layers present on these solid surfaces, the elasto-hydrodynamic lubrication (EHL) regime, at high velocity, where the load is carried by the pressure generated in the lubricant (in this case friction is controlled by shearing the lubricant) and the transition regime between these two lubrication modes is represented by the mixed lubrication (ML) regime where the load is carried by the interacting asperities as well as the pressure generated in the lubricant.

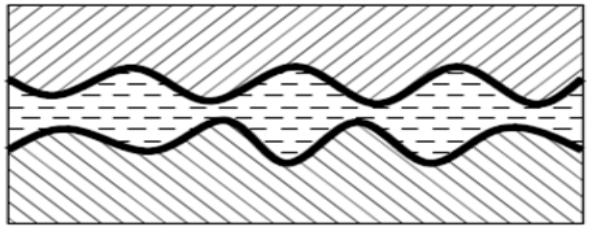

(a) EHL

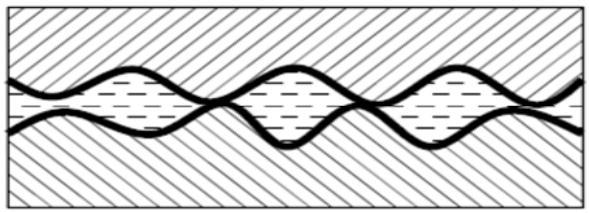

(b) ML

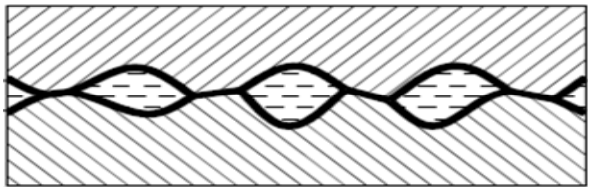

(c) BL

Fig. 2.9 The three lubrication regimes: a) Elasto-hydrodynamic lubrication (EHL), b) Mixed lubrication (ML), c) Boundary lubrication (BL), (thick line represents boundary layer on surfaces).

Friction is a result of shearing the lubricant and the surface layers. The variation of the coefficient of friction with velocity, over the above presented lubrication regimes, is represented by the so-called generalized Stribeck curve [28] which will be discussed extensively in chapter 3.

The contaminated wheel - rail contact must be modelled as a Mixed Lubricated friction model. In the next subsections, some existing models applicable to the wheel - rail contact situation are briefly described.

2.2.2.1 Known wheel - rail friction models

Due to the increasing interest in the low friction phenomenon between wheel and rail, more models were developed for the situation when the rail is contaminated, with theories apart from Kalker's [24] being adopted.

Beagley

Among the first models to predict the friction in the lubricated wheel - rail contact studying the rheological properties of solid contaminants when mixed with water is the model by Beagley [30]. It assumes there is not interfacial slip in the contact zone, and uses the film thickness formula for line contacts of Baglin and Archard [31] adjusted for starved conditions with a correction factor proposed by Wolveridge et al. [32]. The coefficient of friction was calculated by considering Newtonian rheological behaviour for the sheared layer. The results are summarized in Table 2.4.

Table 2.4: Results of the Beagley model [30].

Material	Vickers pyramid number	Shear Strength [N/m^2]	Resultant Thickness mm		Coefficient of friction	
			Load 5×10^4 N	Load 10^5 N	Load 5×10^4 N	Load 10^5 N
Precipitated Fe_2O_3	60	10^8	8.3	6.4	0.3	0.2
Fe_2O_3 +7.5% oil	25	4.2×10^7	3.5	2.7	0.13	0.08
Leaf Debris Sample 1	15	2.5×10^7	2.1	1.6	0.08	0.05
Fe_2O_3/H_2O mix 90% solid		2.2×10^5	1.8×10^{-2}	1.4×10^{-2}	6.6×10^{-4}	4.4×10^{-4}
Fe_2O_3/H_2O mix 80% solid		1.4×10^3	1.2×10^{-4}	9.0×10^{-5}	Friction depends on flow properties	
Fe_2O_3/H_2O mix 70% solid		38	3.2×10^{-6}	2.4×10^{-6}		
Fe_2O_3/H_2O mix 60% solid		3.8	3.2×10^{-7}	2.4×10^{-7}		
Fe_2O_3/H_2O mix 50% solid		0.85	7.1×10^{-8}	5.4×10^{-8}		

Tomberger et al.

Nowadays, lubricated wheel - rail friction is predicted using more complex models. The latest one is the model of Tomberger et al. [33]. The calculation is based on the Hertzian contact model and it computes the local mechanical and thermal stress distributions and resulting traction curves. The model considers Newtonian interfacial fluids, surface roughness and contact temperatures.

The outputs of the model are shown in Fig. 2.10 in terms of traction coefficient as a function of creepage (slip) [%] for different rolling velocities and lubrication conditions, i.e. dry and water, (left figure) and of maximum traction coefficient as a function of rolling velocity [m/s] for different roughnesses (right figure).

In Fig. 2.10, the k_r parameter is defined in [33] as a so-called roughness-parameter ranged between 0 and 1. The 0 value corresponds to very 'smooth' surfaces and 1 value to very 'rough'. BL refers to Boundary Lubrication over the entire rolling velocity range.

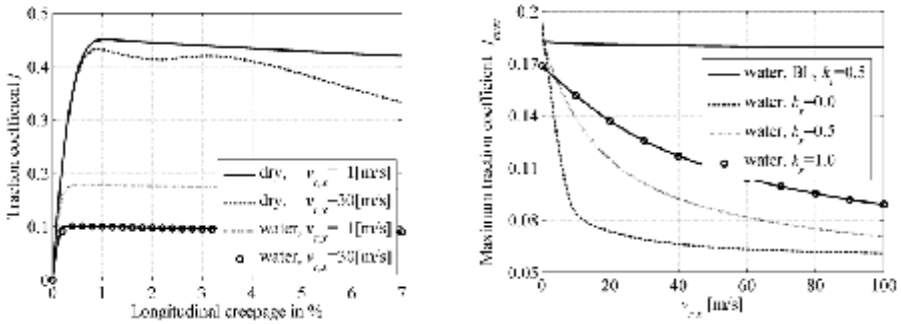

Fig. 2.10 Results of the model of Tomberger et al. [33].

The model predicts Stribeck and traction types of curves for the wheel - rail contact in presence of a Newtonian type of fluid, i.e. water.

2.2.2.2 Other friction models

Other models for predicting the friction in the ML regime, which could be applied to the wheel - rail contact are the friction models for mixed lubricated line or point contacts. Gelinck and Schipper [34] developed a Mixed Lubrication friction model for the line contact by assuming a viscous behaviour of the lubricant. And a similar model was proposed by Liu et al. [35], particularly for the point contact situations (example result is given in Fig. 2.11). Both models consider a Hertzian pressure distribution and statistical Gaussian surface roughness height distribution.

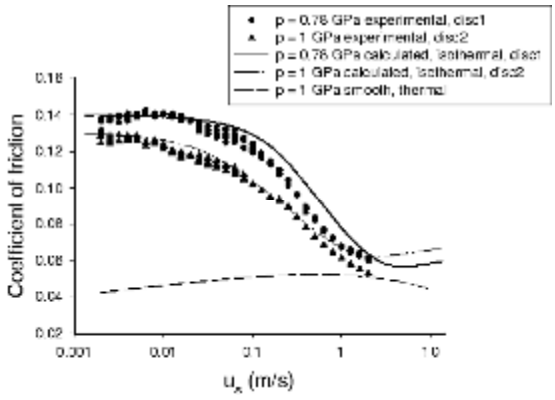

Fig. 2.11 Stribeck curve predicted and measured for the point contact situation [35].

2.2.3 Conclusions on the friction models

The applicability of presented existing models to the "lubricated" wheel - rail contact is based on simplifications on either the contact area (line or point) or the interfacial layer rheological properties and behaviour (Newtonian). Therefore, a more accurate method is required for prediction of the coefficient of friction in the present situation, i.e. elliptical contact and non-Newtonian (viscoelastic) behaviour of the interfacial layer.

2.3 Conclusions

Based on the literature studied it is concluded that the wheel - rail contact can be regarded as a simplified equivalent elliptical one, simplification made for preparing the friction calculation.

For an accurate prediction of the friction levels in the presence of an interfacial layer of non-Newtonian behaviour, a new Mixed Lubrication friction model for the elliptical contact situation must be developed.

Chapter 3

Friction model

The "tool" which controls friction between interacting surfaces is lubrication, which has the effect of decreasing friction and makes a lubricated mechanism more reliable. In another perspective, lubrication may turn negative in systems where friction should be high, like force controlled traction systems and wheel - rail contacts.

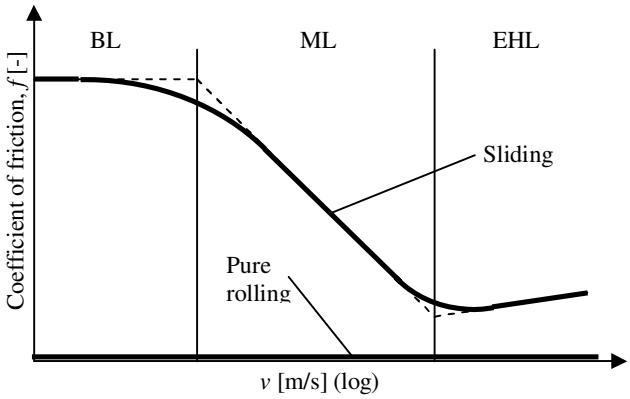

Fig. 3.1 Generalized Stribeck curve.

The three regimes described in section 2.2.2 (Fig. 2.9) are schematically visualized in Fig. 3.1 in which the coefficient of friction is depicted as a function of the (sum) velocity of the contacting bodies.

3.1 Isothermal mixed lubrication model

For the prediction of the Stribeck curve, i.e. friction as a function of velocity, for line contacts, Gelinck and Schipper [34] used the elastic contact model of Greenwood and Williamson [36] for the asperity contact and Moes function fit [37] for the central film thickness in EHL. The model was further extended to highly loaded line contacts by Faraon [38], where the asperity friction component was calculated by using Zhao's elasto-plastic model [39] and the separation was calculated by using the definition of the film thickness according to Johnson et al. [40].

In the present chapter, the aforementioned model is extended to elliptical contacts including the slip component over the entire lubrication regimes. Next, by using an elastic plastic shear model for the boundary layer, traction curves are predicted in which the coefficient of friction is represented as a function of roll/slide (slip) ratio.

3.1.1 Elastohydrodynamic component

For the hydrodynamic component, the first parameter to calculate is the film thickness. In order to simplify the calculation and to have a small number of variables, dimensionless numbers were introduced.

The first set of dimensionless numbers is defined after Dowson and Higginson [41]:

$$G = \alpha E' ;\ \bar{h} = \frac{h}{R_x} ;\ U_\Sigma = \frac{\eta_0 v^+}{E' R_x} ;\ W = \frac{F_N}{E' R_x^{\,2}} \tag{3.1}$$

where the number G is referred to the lubricant, $\bar{h}$ to the film thickness, U_Σ to the velocity and W to the load respectively.

The second set consists of three numbers and are defined after Moes [37]:

$$H = \bar{h} U_\Sigma^{-\frac{1}{2}} ;\ M = W U_\Sigma^{-\frac{3}{4}} ;\ L = G U_\Sigma^{\frac{1}{4}} \tag{3.2}$$

where H is the film thickness number, M is the load number and L is the lubricant number.

Using these numbers, the system of three equations which describes an EHL elliptic contact (Reynolds equation, elastic deformation equation and load balance) was solved numerically by Nijenbanning et al. [42] resulting in a film shape and pressure distribution.

It must be mentioned that in the Reynolds equation, the viscosity of the lubricant was considered to vary with pressure according to Roelands equation [43], which reads:

$$\eta(p)=\eta_0 \exp\left\{\left[\left(1+\frac{p}{p_r}\right)^z-1\right]\ln\left(\frac{\eta_0}{\eta_\infty}\right)\right\} \tag{3.3}$$

After computing the results, an equation for the central film thickness was derived by curve fitting the numerical results using the dimensionless numbers [42]:

$$H_C=\left\{\left[H_{RI}{}^{\frac{3}{2}}+\left(H_{EI}{}^{-4}+H_{00}{}^{-4}\right)^{-\frac{3}{8}}\right]^{\frac{2s}{3}}+\left(H_{RP}{}^{-8}+H_{EP}{}^{-8}\right)^{-\frac{s}{8}}\right\}^{\frac{1}{s}} \tag{3.4}$$

$$s=1.5\left[1+\exp\left(-1.2\frac{H_{EI}}{H_{RI}}\right)\right] \tag{3.5}$$

where, H_{00} is a constant, H_{RI} is the rigid-isoviscous asymptote, H_{EI} the elastic-isoviscous asymptote, H_{RP} the rigid-piezoviscous asymptote and H_{EP} the elastic-piezoviscous asymptote.

$$H_{00}=1.8\cdot\vartheta^{-1} \tag{3.6}$$

$$H_{RI}=145\cdot\left(1+0.796\cdot\vartheta^{\frac{14}{15}}\right)^{-\frac{15}{7}}\vartheta^{-1}M^{-2} \tag{3.7}$$

$$H_{EI}=3.18\cdot\left(1+0.006\cdot\ln\vartheta+0.63\cdot\vartheta^{\frac{4}{7}}\right)^{-\frac{14}{25}}\vartheta^{-\frac{1}{15}}M^{-\frac{2}{15}} \tag{3.8}$$

$$H_{RP}=1.29\cdot\left(1+0.691\cdot\vartheta\right)^{-\frac{2}{3}}L^{\frac{2}{3}} \tag{3.9}$$

$$H_{EP}=1.48\cdot\left(1+0.006\cdot\ln\vartheta+0.63\cdot\vartheta^{\frac{4}{7}}\right)^{-\frac{7}{20}}\vartheta^{-\frac{1}{24}}M^{-\frac{1}{12}}L^{\frac{3}{4}} \tag{3.10}$$

where $\vartheta=R_x/R_y$ is the ratio of the reduced radius of curvatures in and perpendicular to the rolling/sliding direction.

3.1.2 Asperity component

If a surface is measured with, for instance, an interferometer, asperities can be determined, to be used in the microcontact model, by using the 9-points summit definition [44], i.e. a point is regarded as a summit if its 8 surrounding points are

lower. Every asperity is computed as an ellipsoid determined by height z_i and two radii of curvature in the main directions (in and perpendicular to rolling/sliding direction). The contact between asperities and the counter surface is assumed to be elastic and the contact area and normal load is determined according to the Hertz theory (Appendix E).

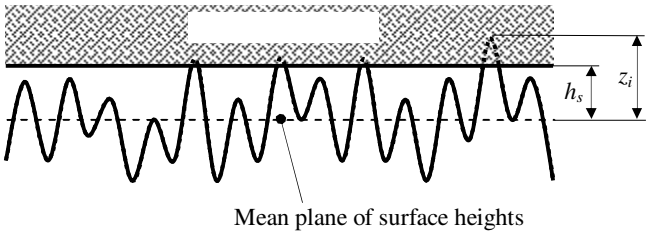

Fig. 3.2 Contact between a smooth and a rough surface.

The asperity contact area A_C and the load carried by asperities F_C are given by summation of the individual contributions of each microcontact:

$$F_C = \sum_{i=1}^{N} F_i(\delta_i) \tag{3.11}$$

$$A_C = \sum_{i=1}^{N} A_i(\delta_i) \tag{3.12}$$

where $\delta_i = z_i - h_s$ is the asperity indentation or deformation depth and N is the number of asperities in contact.

3.1.3 Separation

Johnson et al. [40] proposed a relation between the separation of two rough surfaces and the mean film thickness. He approximated the film thickness with the cross-sectional area of the gap between two undeformed Gaussian distributed profiles, divided by the gap length. Looking at Fig. 3.2, the statistical formulation of the above-mentioned film thickness reads [40]:

$$h_c = \int_{-\infty}^{h_s} (h_s - z) f(z) dz \tag{3.13}$$

where h_c is the film thickness, h_s is the separation and $f(z)$ is the Gaussian height distribution. With this definition, the deformed cross-sectional area of the two profiles is ignored, by limiting the surface points coordinate to a maximum equal with the separation, h_s.

As previously stated, the microcontact model of the present work is deterministic, making direct use of the measured surface heights. In this case the film thickness is

equal with the volume between the two surfaces divided by the nominal contact area. The deterministic formulation is:

$$h_c = \frac{1}{n}\sum_{j=1}^{n}\left(h_s - z_j\right) \tag{3.14}$$

where n is the number of measured points and z_j is the height relative to the mean plane of surface heights (Fig. 3.2). Here, the volume described by the deformed material is taken into account, assuming that the material is incompressible and its volume preserves as well. This assumption is made only for calculating the separation. The asperity contact model is calculated according to the Hertz theory.

The truncation method of Johnson et al. [40] (the surface points are limited to a maximum equal with h_s) is applicable to the situation when the separation becomes negative. A short discussion on how the two approaches influence the result is given in Appendix A.

3.1.4 The friction model

Mixed lubrication is the transition regime between BL and EHL. Here, the coefficient of friction takes values between the coefficient of friction of the other regimes and the load is carried by the BL and the EHL force component:

$$F_N = F_C + F_H \tag{3.15}$$

Where F_C is the load carried by asperities and F_H is the load carried by the lubricant. In terms of pressure, Eq. 3.15 is written as [40] (Fig. 3.3):

$$P_N = P_C + P_H \tag{3.16}$$

in which $P_i = F_i / A_{nom}$, $i = N, H$ or C and A_{nom} is the nominal contact area.

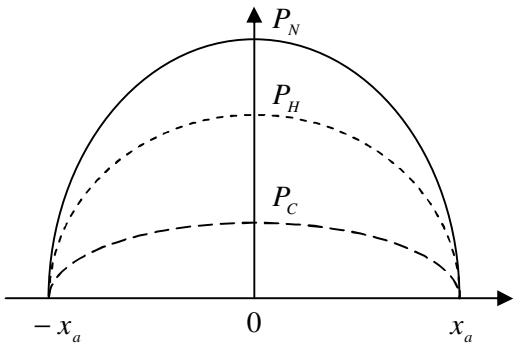

Fig. 3.3 Normalized pressure distribution in an ML contact [40].

Based on this equation (3.16), two coefficients γ_1 and γ_2 are introduced [40]:

$$\gamma_1 = \frac{F_N}{F_H} = \frac{P_N}{P_H} \text{ and } \gamma_2 = \frac{F_N}{F_C} = \frac{P_N}{P_C} \tag{3.17}$$

The above defined coefficients are mutually dependent through Eq. 3.18.

$$\frac{1}{\gamma_1} + \frac{1}{\gamma_2} = 1 \tag{3.18}$$

Using these two coefficients and combining a deterministic multi-asperity contact model with the EHL theory, the entire Stribeck curve can be computed.

The hydrodynamic component is calculated using the γ_1 coefficient. Making the substitutions [40], $F_N \to F_N/\gamma_1$ and $E' \to E'/\gamma_1$ in Eq. 3.4 - 3.5 the central film thickness for an elliptical contact becomes:

$$H_C = \gamma_1^{\frac{1}{2}} \left\{ \left[\gamma_1^{\frac{9}{4}} H_{RI}^{\frac{3}{2}} + \left(\gamma_1^{-\frac{2}{5}} H_{EI}^{-4} + H_{00}^{-4} \right)^{-\frac{3}{8}} \right]^{\frac{2s}{3}} + \left[\gamma_1^{4} \left(H_{RP}^{-8} + H_{EP}^{-8} \right) \right]^{-\frac{s}{8}} \right\}^{\frac{1}{s}} \tag{3.19}$$

$$s = 1.5 \left[1 + \exp\left(-1.2 \frac{H_{EI}}{H_{RI}} \gamma_1^{-\frac{7}{5}} \right) \right] \tag{3.20}$$

The constant H_{00} and the four asymptotes H_{RI}, H_{EI}, H_{RP} and H_{EP} remain the same as presented in Eq. 3.6 - 3.10. The dimensionless film thickness H_C is given by Eq. 3.2.

To calculate the load carried by asperities F_C, the load carried by the lubricant F_H and the film thickness h_c a system of three equations has to be solved:

- Load balance Eq. 3.15.
- Film thickness Eq. 3.19.
- Load carried by asperities (from the microcontact model) Eq. 3.11, by using the separation, h_s, calculated from Eq. 3.14 (making h_c equal with the value derived from Eq. 3.19).

Solving this system of three equations with three unknowns, the coefficient of friction in ML can be computed as presented further. The solution scheme of the solver is presented in Appendix B.

3.1.5 Friction force

The velocity between two moving surfaces can be regarded as a superposition of a pure rolling and a pure sliding motion [45]. In Fig. 3.4 (a), the individual velocities of the moving surfaces are plotted as well as their sum $v^+ = v_1 + v_2$ and their difference or the sliding velocity $v^{dif} = |v_1 - v_2|$. In Fig. 3.4 (b), a velocity diagram

is given showing lines for constant sliding velocity, constant sum velocity and constant slip are drawn. The slip or slide-to-roll ratio is defined as:

$$S = \frac{2 \cdot v^{dif}}{v^{+}} = \frac{2 \cdot |v_1 - v_2|}{v_1 + v_2} \tag{3.21}$$

In Fig. 3.4 (b), if the coefficient of friction is plotted perpendicular to the velocity field, each constant slip line in the velocity field represents a Stribeck curve. A traction curve (most frequently used in EHL) represents the coefficient of friction evolution by varying the slip, while keeping the sum velocity constant.

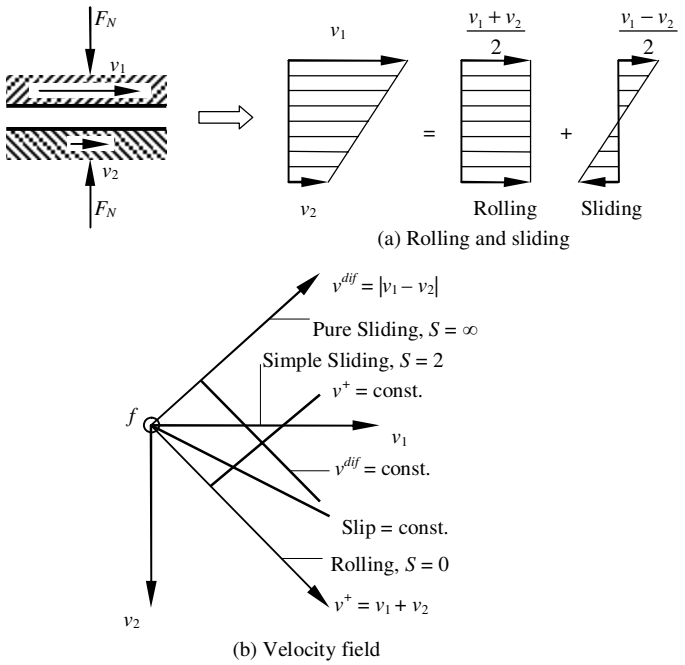

Fig. 3.4 Velocity field for two moving surfaces [45].

The friction force in EHL lubricated contacts is caused by shearing the lubricant. In BL, the friction force is caused by shearing the boundary layer existing between the contacting asperities. The level of friction is often expressed by the so-called shear rate $\dot{\gamma}$ defined as:

$$\dot{\gamma} = \frac{v^{dif}}{h_c} \tag{3.22}$$

where h_c is the film thickness.

3.1.5.1 Friction in EHL

In the EHL regime, friction is caused by shearing the lubricant in the contact. The shear stress τ_H in the lubricant is defined as a function of the shear rate $\dot{\gamma}$ and using the Eyring model, this is:

$$\tau_H = \tau_0 \operatorname{arcsinh}\left(\frac{\eta\dot{\gamma}}{\tau_0}\right) \tag{3.23}$$

Integrating the shear stress over the contact area, the friction force is obtained:

$$F_{f,EHL} = \iint_{A_H} \tau_H(\dot{\gamma}) dA_H \tag{3.24}$$

where $A_H = A_{nom} - A_C$ is the hydrodynamic contact area and A_C is the asperity contact area (Eq. 3.12). The friction force generated by the EHL component is expressed by:

$$F_{f,EHL} = \tau_0 A_H \operatorname{arcsinh}\left(\frac{\eta S v^+}{2\tau_0 h_c}\right) \tag{3.25}$$

3.1.5.2 Friction in BL

The friction in the BL regime is caused by shearing the boundary layer between the contacting asperities. Integrating the shear stress τ_C over the asperity contact area, the friction force generated by a pair of asperities in contact is obtained. So, the friction force in the boundary lubrication regime is equal with the sum of all contacting asperities:

$$F_{f,BL} = \sum_{i=1}^{N} \iint_{A_{Ci}} \tau_{Ci} dA_{Ci} \tag{3.26}$$

Considering the friction force in the asperity contact to be of Coulomb type i.e. $\tau_{Ci} = f_{Ci} \cdot p_{Ci}$, with a constant value of the coefficient of friction $f_{Ci} = f_C$, the friction force in the BL regime for the simple sliding situation is written:

$$F_{f,BL} = f_C \sum_{i=1}^{N} \iint_{A_{Ci}} p_{Ci} dA_{Ci} = f_C F_C \tag{3.27}$$

where the Coulomb coefficient of friction, f_C, is experimentally determined.

Eq. 3.27 gives the value of the friction force in BL for simple sliding contacts. However, in rolling to sliding contacts, taking into account the slip in the BL regime, there is no theoretical model. The slip is incorporated in the shear rate, but since in the presented model the friction in the asperity component is considered to be of Coulomb type, the shear stress of the boundary layer does not change with

the shear rate. Therefore, also used in this thesis, an arctangent function fit is proposed and used by Gelinck [46] for the frictional behaviour of a rolling/sliding contact operating in BL regime for line contacts.

$$f = f_C \frac{2}{\pi} \arctan\left(\frac{\pi}{2} \frac{S}{S_{ep}}\right) \tag{3.28}$$

A generalized traction curve calculated with Eq. 3.28 is shown in Fig. 3.5.

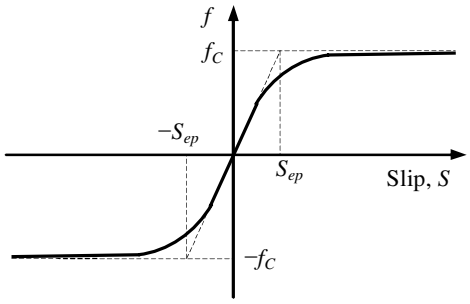

Fig. 3.5 Schematic traction curve in BL.

When operating in the BL regime and increasing the slip, while the sum velocity is kept constant, the coefficient of friction will increase from zero when $S = 0$ (pure rolling) to the Coulomb value f_C when $S = 2$ (simple sliding). A parameter S_{ep} is introduced, which is a measure for the transition from elastic to plastic behaviour of the boundary layer. This parameter is determined experimentally.

Combining Eq. 3.27 and Eq. 3.28 will result in an expression for the friction force in the BL regime:

$$F_{f,BL} = f_C F_C \frac{2}{\pi} \arctan\left(\frac{\pi}{2} \frac{S}{S_{ep}}\right) \tag{3.29}$$

3.1.5.3 Friction in ML

The friction force in the ML regime is given by summing the friction force generated by the asperities in contact and the friction generated by shearing the lubricant:

$$F_{f,ML} = F_{f,BL} + F_{f,EHL} \tag{3.30}$$

Substituting Eq. 3.25 and Eq. 3.29 in Eq. 3.30 and, $f = F_f / F_N$, the formula for the coefficient of friction in ML is determined:

$$f = \frac{f_C F_C \frac{2}{\pi} \arctan\left(\frac{\pi}{2}\frac{S}{S_{ep}}\right) + \tau_0 A_H \operatorname{arcsinh}\left(\frac{\eta S v^+}{2\tau_0 h_c}\right)}{F_N} \tag{3.31}$$

After solving the ML regime (load carried by asperities, load carried by lubricant and the separation), the coefficient of friction can be computed using Eq. 3.31 over the entire range of lubrication regimes.

If the slip S is kept constant and the sum velocity v^+ is varied, the result of the presented ML friction model, finalized with Eq. 3.31, is a Stribeck curve. If the sum velocity is kept constant and the slip is varied, the output of the model is the traction curve.

3.1.6 Results and discussions

3.1.6.1 Stribeck curve

The results of the friction calculations are presented in Fig. 3.7. For comparison, the calculation is given for a line contact, for the same contact pressure. The line contact is validated with experiments [38]. Different results can be obtained from the model as real contact area, number of asperities in contact, load carried by the asperities, load carried by the lubricant, separation between the surfaces and, most importantly, the variation of the coefficient of friction as a function of velocity, viscosity, roughness, etc.

The input parameters used in the calculation are presented in Table 3.1.

Table 3.1: Reference input parameters.

Property	Value	Unit	Description
n	1.1×10^{11}	m^{-2}	Density of asperities
β	8.3×10^{-6}	m	Average radius of asperities
σ_s	7.6×10^{-8}	m	Standard deviation of asperities
E'	231	GPa	Combined elasticity modulus
η_0	0.02	Pa·s	Viscosity at ambient pressure
τ_0	2.5	MPa	Eyring shear stress
α	2×10^{-8}	Pa^{-1}	Viscosity – pressure coefficient
z	0.679	-	Viscosity – pressure index
R_x	10×10^{-3}	m	Radius in x (rolling) direction
R_y	40×10^{-3}	m	Radius in y direction
F_N	100	N	Normal load
f_C	0.13	-	Coefficient of friction in BL
S_{ep}	0.015	-	Slip at the transition from elastic to plastic behaviour

In the following, Stribeck curves plot the coefficient of friction (left y axis) and dimensionless separation, h_c/σ , σ is the standard deviation of the roughness, (right y axis) as a function of velocity within the specified range. In general, the coefficient of friction decreases in the ML regime as the film thickness increases with velocity.

Comparison with equivalent line contact

Nijenbanning [42] proposed an equivalent line contact for comparing the film thickness given by Eq. 3.4 with the film thickness calculated for line contacts [37]. A similar model is proposed here but slightly different. For a given elliptical contact, the equivalent line contact is the contact having the same half width in the rolling/sliding direction and the same mean contact pressure at the same normal load (Fig. 3.6).

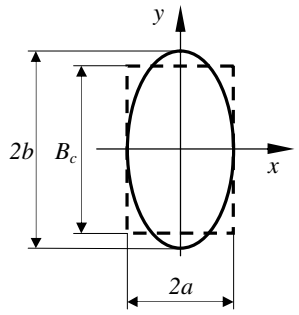

Fig. 3.6 Equivalent line contact (dashed line).

So for given R_x, R_y and F_N, the equivalent line contact will be calculated as follows:

$$B_c = \frac{F_N}{2 \cdot a \cdot p_m} \tag{3.32}$$

$$R_c = \frac{\pi \cdot E' \cdot a}{16 \cdot p_m} \tag{3.33}$$

Using the above dimensions for the line contact with the same normal load as used in the elliptical situation, the mean contact pressures and the half widths in rolling/sliding direction in both situations will be equal. The dimensions of the equivalent cylinder for the input geometry from Table 3.1, according to Eq. 3.32 and 3.33 are: $B_c = 0.6$ mm and $R_c = 10.8$ mm.

Fig. 3.7 plots the coefficient of friction given by Eq. 3.31, in which the load carried by asperities, F_C, and film thickness, h_c, are calculated with the model described in section 3.1.4, against the (sum) velocity together with the equivalent

line contact (Eq. 3.32 and 3.33), for the standard case given in Table 3.1.

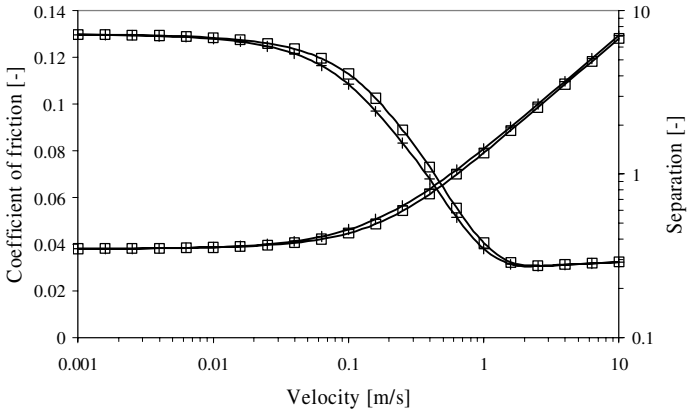

Fig. 3.7 Comparison between the elliptical contact (□) and the equivalent line contact (+).

The results are very close. There is a small difference for the coefficient of friction at the transition between BL and ML regime.

Influence of load

As can be noticed in Fig. 3.8, the transition between the different lubrication regimes is hardly influenced by the normal load, the ML regime, however, extends over a wider velocity range and the coefficient of friction is lower with increasing load in the low velocity region.

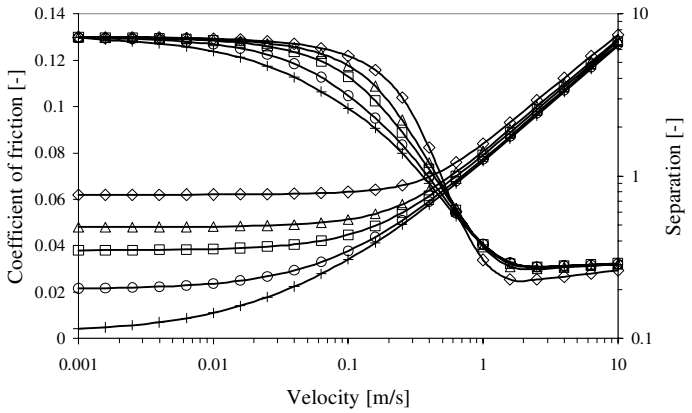

Fig. 3.8 Stribeck curve and separation (h_c/σ) for different normal loads: ◊ 10 N (281 MPa), Δ 50 N (481 MPa), □ 100 N (606 MPa), ○ 200 N (764 MPa) and + 300 N (874 MPa).

Influence of roughness

In order to study the influence of the surface roughness on the coefficient of friction and separation curve, several surfaces with a Gaussian height distribution were randomly generated and associated with the same macro geometry and external factors as presented in Table 3.1.

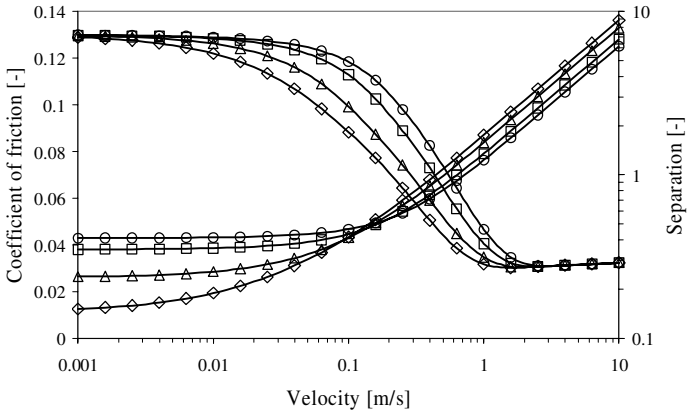

Fig. 3.9 Effect of the statistical roughness parameter, σ, on Stribeck curve and dimensionless separation (h_c/σ); standard deviation of roughness of: ◊ 0.06, Δ 0.07, □ 0.08 and ○ 0.09 μm respectively.

In Fig. 3.9 it can be noticed that the Stribeck curve shifts to the right with increasing roughness, which makes sense because when the standard deviation of the roughness increases, then the separation between the two surfaces has to be larger to have lift off (full separation between the surfaces).

Because the presented model is deterministic, the roughness influence discussion is possible with different generated surfaces using as input the standard deviation. In which case, for each generated surface, the average radius of the summits is decreasing with decreasing the standard deviation of the asperity heights distribution. In the four situations presented above, the average radius of the summits decreased from 11 microns for the smooth surface to 7 microns for the rough one.

Influence of viscosity

The same surface and inputs were chosen as given in Table 3.1 to study the effect of viscosity on the Stribeck curve for elliptical contacts (Fig. 3.10).

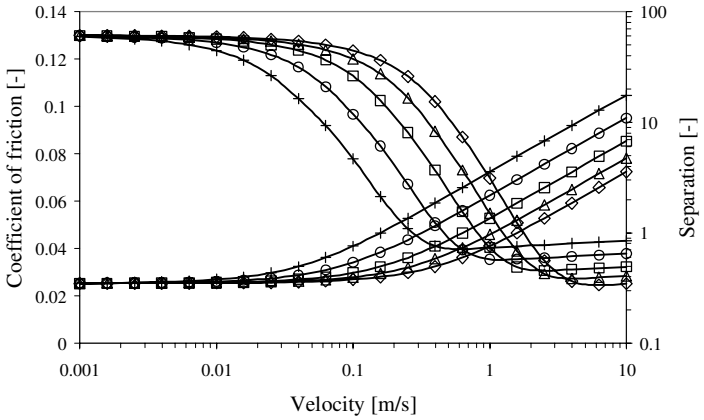

Fig. 3.10 Influence of viscosity η_0 on the Stribeck curve and separation (h_c/σ). Viscosity of: ◊ 0.008, Δ 0.012, □ 0.02, ○ 0.04 and + 0.08 Pas respectively.

As expected, the film thickness at the same velocity is higher when a more viscous lubricant is considered. Therefore, the ML regime shifts to the left while the friction in the EHL regime increases due to an increase in viscosity.

3.1.6.2 Traction curve

In Fig. 3.11 the coefficient of friction is plotted as a function of slip for different values of sum velocity.

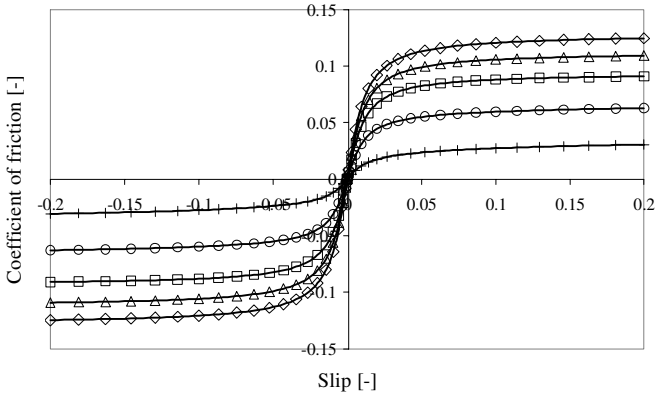

Fig. 3.11 Traction curves for different sum velocities of ◊ 0.01, Δ 0.1, □ 0.2, ○ 0.4 and + 1 m/s respectively.

The input parameters for this calculation are given in Table 3.1.

As can be seen, the coefficient of friction is increasing from 0 (pure rolling) until it reaches the corresponding value for simple sliding as the computed Stribeck curve Fig. 3.7 - Elliptical contact. At low velocity (0.01 m/s), the coefficient of friction is increasing from zero to 0.13 after the slip is exceeding approximately 5%.

3.1.7 Conclusions

A mixed lubrication friction model is developed for lubricated elliptical contacts. A good agreement is found between the presented elliptical model and the proposed equivalent line contact. Different parameters were varied in order to study their influence on the Stribeck curve and separation. In the present case, the variations noticed were similar to the existing friction model for line contacts, i.e. Gelinck [34] and Faraon [38]. The most significant influences in the Stribeck curve are in the ML regime which shifts to the left (the coefficient of friction decreases) with increasing the viscosity of the lubricant and with decreasing of surface roughness. The normal load hardly influences the transition between different regimes. However, the ML regime extends over a wider velocity range. Not less important is the EHL regime, which shifts up with increasing both normal load and viscosity of the lubricant. Of course, the roughness in EHL regime has no influence on the friction level. Finally, since the friction in BL regime is of Coulomb type, none of the above parameters influences the friction level in that regime.

3.2 Frictional heating

As described in the previous section, when the velocity between the contacting bodies varies enough, lubricated concentrated contacts can function in three lubrication regimes (Fig. 3.12).

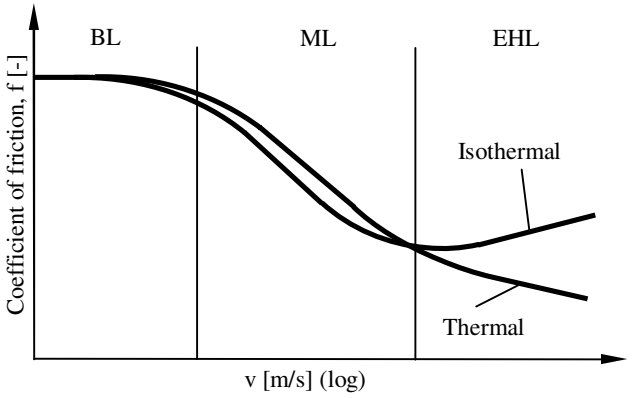

Fig. 3.12 Stribeck curve. Schematically isothermal and thermal.

It is well known that where friction occurs, heat is generated. In this section, the friction model presented in section 3.1 is extended by taking into account the temperature generated in contact due to frictional heating. Because the level of friction in the EHL is controlled by the lubricant properties and their variation with pressure and temperature, friction is influenced by the contact temperature. The coefficient of friction in BL regime is obtained by measurement and is considered to be of Coulomb type.

When frictional heating is taken into account, a decrease in friction is expected in the EHL regime due to decreasing viscosity (Fig. 3.12).

The same effect is noted also when traction curves are plotted at high velocities, i.e. EHL regime (Fig. 3.13), the coefficient of friction decreases with increasing slip value (or increasing sliding velocity).

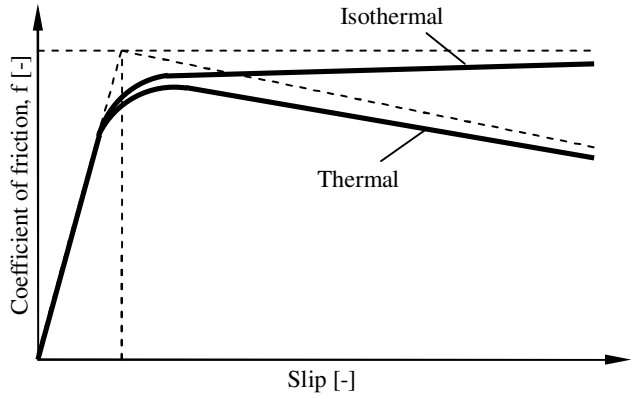

Fig. 3.13 Temperature influence on the Traction curve.

3.2.1 The frictional heating model (Bos and Moes)

From the very start of lubrication applications until today, researchers studied the thermal effects on the elastohydrodynamic concentrated contacts [47], [48] and [49]. In a rolling-sliding elliptical contact, the heat is developed at high sum velocities combined with high slip values. The thermal model used in the present study is the model of Bos and Moes [49] which is summarized below.

In the quasi steady state situation, the bulk temperatures of the bodies are not affected by heat transfer. Considering a stationary elliptical contact situation with low velocity and a stationary heat source, the oil temperature within the contact will be:

$$T_f = T_i + \frac{Q_F}{K_{eff}\sqrt{ab}} \tag{3.34}$$

Where, T_i is the oil inlet temperature and a, b are the semi axis of the contact ellipse (with a in rolling/sliding direction). The rate of heat flow, F, is:

$$Q_F = F_f \cdot v^{dif} \tag{3.35}$$

Where, F_f is the friction force in contact and $v^{dif} = |v_1 - v_2|$ is the sliding velocity. The last parameter in Eq. 3.34 is the effective thermal conductivity which reads:

$$K_{eff} = \frac{K_1}{\theta_1} + \frac{K_2}{\theta_2} \tag{3.36}$$

K_1, K_2 are the thermal conductivity and θ_1, θ_2 are the dimensionless flash temperatures factors/numbers of the two bodies respectively. For the calculation of θ_1 and θ_2, the reader is referred to Appendix C.

3.2.2 Temperature influence on viscosity

The main parameter influenced by the temperature is the viscosity of the lubricant which is calculated according to Roelands [43]:

$$\eta = \eta_i \exp\left\{\ln\left(\frac{\eta_i}{\eta_\infty}\right)\left[\left(\frac{135+T_i}{135+T_f}\right)^{S_0}\left(1+\frac{p}{p_r}\right)^{z}-1\right]\right\} \tag{3.37}$$

In which, T_f is the oil temperature within the contact and p is the hydrodynamic pressure, $p \equiv P_H$.

3.2.3 The film thickness

The heat generated in the EHL regime is caused by shearing of the lubricant. The film thickness is influenced by the inlet temperature (inlet viscosity) of the lubricant. Considering only small changes in the oil temperature, a model of inlet shear heating was proposed by Greenwood [50] and further a reduction factor for the film thickness due to inlet shear heating. Without actual calculation of the inlet shear heating, in later papers [51] [52] [53], authors developed other methods for calculating the film thickness considering changes in viscosity due to operational conditions. In fact, the models propose reduction factors for the thermal film thickness of EHL line contacts.

In the absence of a reduction factor for the elliptical contact situation, the film thickness calculated as in Eq. 3.19 will be corrected with a reduction factor as proposed in [51] and [53].

Using the equivalent line contact introduced in section 3.1.6.1, the comparison with the elliptical contact showed a very close result in terms of film thickness and friction. The results calculated with the two correction factors will be checked according to the hypothesis that the difference between the two film thicknesses (line [37] and elliptical contacts [42]) remains constant for both isothermal and thermal cases.

The two considered film thickness reduction factors according to Pandey [51] and Wilson [53] read as follows:

$$C = \frac{1}{1+0.113\cdot Q^{0.71}\cdot\left(1+5.650\cdot S^{0.96}\right)} \tag{3.38}$$

$$C = \frac{1}{1+0.241\cdot Q^{0.64}\cdot\left(1+8.325\cdot S^{0.83}\right)} \tag{3.39}$$

Where, S is the slip or sliding/rolling ratio (Eq. 3.21) and Q is the so-called thermal load parameter:

$$Q = \frac{\beta_0 \cdot \eta_i \cdot \left(v^+\right)^2}{4K_{\text{lub}}} \tag{3.40}$$

Where, β_0 is the temperature coefficient of viscosity, η_i is the inlet viscosity and K_{lub} is the thermal conductivity of the lubricant. Because the film thickness (Eq. 3.19) is calculated considering the viscosity of the lubricant varying with temperature according to Roelands [43], β_0 is approximated by [48]:

$$\beta_0 = \ln\left(\frac{\eta_i}{\eta_\infty}\right)\frac{S_0}{135 + T_i} \tag{3.41}$$

To study the influences of the correction factors on the film thickness, the reference for calculation is chosen as given in Table 3.1.

After calculating the film thicknesses between the elliptical contact and the equivalent line contact, i.e. $B_c = 0.6$ and $R_c = 10.8$ mm, for different sum velocities and constant slip, the calculated relative difference in [%] (having the line contact as the baseline) is shown in Fig. 3.14.

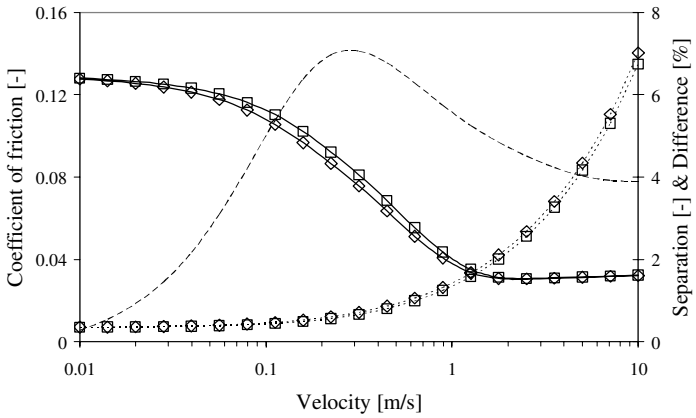

Fig. 3.14 The isothermal Stribeck curve (—) on left axis and separation, h_c/σ, (· ·) & relative film difference (– –) on right axis for □ elliptical and ◊ equivalent line (reference for the calculated relative difference) contacts.

In Fig. 3.14, the separation is defined as the ratio of the calculated film thickness over roughness, σ. The calculated relative difference does not overshoot 10%, which gives good correlation between the two film thickness formulas [37] and [42]. Further, the film thickness of the equivalent line is corrected using Eq. 3.38 and 3.39. The result is compared with the elliptical contact, using the same reduction factors and plotted in Fig. 3.15.

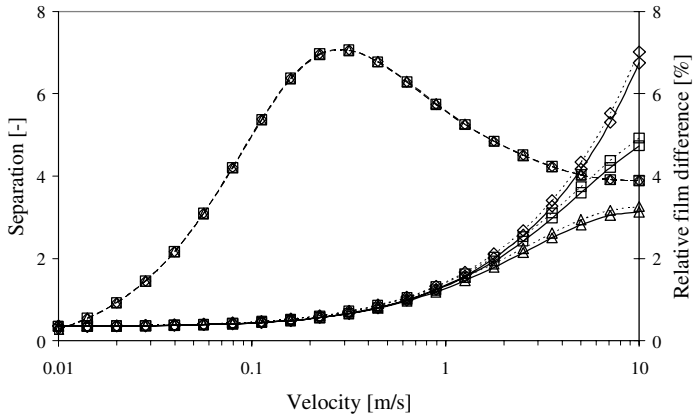

Fig. 3.15 The relative difference (– –) and separation (h_c/σ) for elliptical (—) and equivalent line (reference for the calculated relative difference, (· ·)) contacts. ◊ isothermal, □ Pandey (Eq. 3.38) and Δ Wilson (Eq. 3.39).

The relative film difference practically remains unchanged, meaning that the correction factors can be used for both elliptical and line contacts.

3.2.4 The friction model

The friction force in a Mixed Lubrication (ML) contact is calculated with Eq. 3.30, in which the friction force in the EHL regime, $F_{f,EHL}$, is sensitive to temperature changes because of its viscosity dependency and is calculated according to the Eyring shear model used for the lubricant (Eq. 3.25). In Eq. 3.30, friction in the BL regime is considered to be of Coulomb type and the model includes traction by introducing a so-called slip at the transition from elastic to plastic behaviour of the boundary layer, S_{ep} (Eq. 3.29).

In Eq. 3.25 and 3.29, parameters dependent on the temperature are the viscosity (depending on the oil temperature within the contact), $\eta = \eta\left(P_H, T_f\right)$, and the film thickness (depending on the inlet viscosity of the lubricant), $h_c = h_c\left(\eta_i\left(T_i\right)\right)$. The viscosity of the oil within the contact is dependent on the frictional heating which, as shown in Eq. 3.34, is influenced by the friction force in the contact, F_f. Therefore, a mutual dependency between the two parameters (T_f and F_f) must be solved. The solution scheme for solving the system is shown in Appendix D.

The Stribeck curve and the thermal corrected film thickness calculated for the elliptical contact are shown in Fig. 3.16.

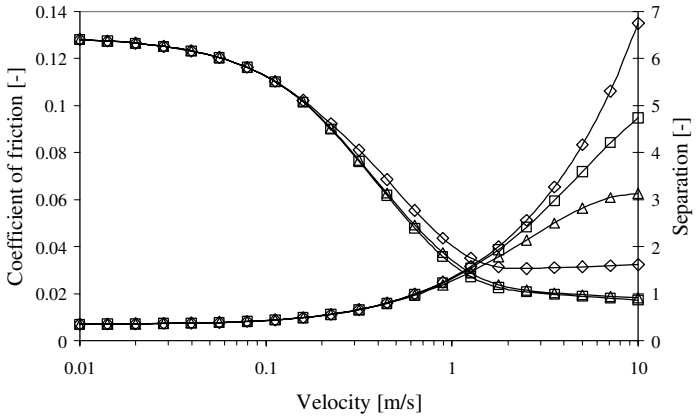

Fig. 3.16 Stribeck curve and film thickness (h_c/σ) reduction from ◊ isothermal to thermal using □ Pandey (Eq. 3.38) and Δ Wilson (Eq. 3.39) reduction factors.

Noting that, in terms of friction, there is no significant difference in the Stribeck curve (Fig. 3.16), for further results and discussions the correction factor of Pandey (Eq. 3.38) will be used, showing a less drastic reduction of the film thickness.

3.2.5 Results and discussions

For the interpretation of the results obtained with the previously described model, a tribo-system is chosen with the input parameters as shown in Table 3.1. For the frictional heating model, extra thermal parameters are needed for the contacting bodies and lubricant. These are given in Table 3.2.

Table 3.2: Thermal input parameters.

Property	Value	Unit	Description
K_{lub}	0.12	W/m/K	Thermal conductivity of the lubricant
$K_1 = K_2$	45	W/m/K	Thermal conductivity of the contacting bodies (steel)
$\rho_1 = \rho_2$	7.85×10^3	kg/m^3	Density of the contacting bodies (steel)
$c_1 = c_2$	477	J/kg/K	Specific heat at constant temperature of the two contacting bodies (steel)

3.2.5.1 Stribeck curve

In the correction factor used (Eq. 3.38), the thermal load parameter (Eq. 3.40) is a function of the temperature coefficient of viscosity, β_0, which has the approximated form given by Johnson [48]. Therefore, out of Eq. 3.41, the temperature increase into the contact has no influence on the film thickness (Fig. 3.17). This is in

agreement with the adopted model of Bos [49] for calculating the temperature increase due to frictional heating, which states that bulk temperatures of the bodies are not affected by the heat transfer.

There are four types of temperature numbers describing different situations for the temperature rise and heat source. They are given in Appendix C, Table C.1. A comparison between the types of numbers on the Stribeck curve is shown in Fig. 3.17.

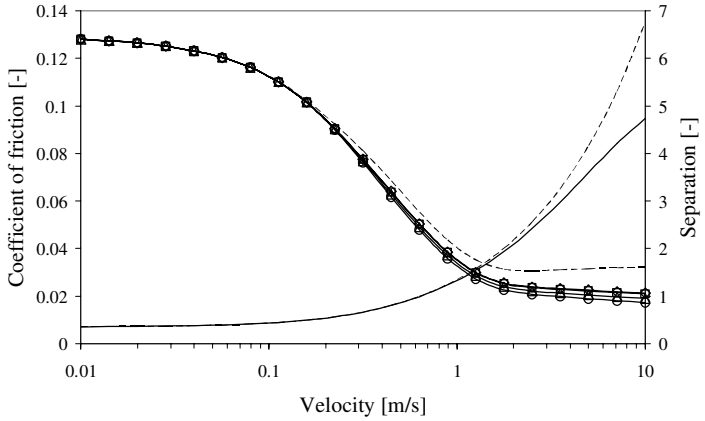

Fig. 3.17 The influence of temperature numbers (Table 3.2 and Table C.1) on the Stribeck curve in terms of (heat source – temperature rise): ◊ no frictional heating, Δ uniform - average, □ uniform - maximum, ○ ellipsoidal - average and + ellipsoidal - maximum.

When the maximum temperature rise is considered in the calculation, the coefficient of friction in EHL regime is slightly lower than in the case of an average temperature rise, for both types of heat source. There is no significant difference for a comparison between the heat source types, i.e. uniform or elliptical.

Moreover, when taking into consideration the maximum temperature rise for the elliptical heat source, the influence of the viscosity - temperature index, S_0, on the Stribeck curve is plotted in Fig. 3.18 for an inlet oil temperature of 20 ºC. Thermal effects on the film thickness reduction factor (Eq. 3.38) immediately became visible with increasing viscosity - temperature index, S_0. Subsequently, due to frictional heating, the coefficient of friction in the EHL regime is also decreasing due to a decrease of the η/h_c ratio (Eq. 3.25).

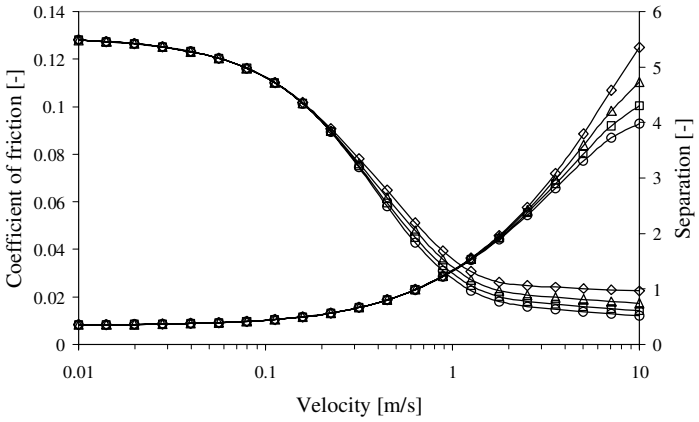

Fig. 3.18 The influence of the viscosity index, S_0, on the Stribeck curve and on the film thickness (h_c/σ) for an inlet temperature of the lubricant of 20 °C: ◊ 0.5, Δ 1, □ 1.5 and ○ 2.

The same discussion is proposed for a lubricant inlet temperature of 40 ºC (Fig. 3.19). Because the viscosity of the lubricant in the inlet decreases with temperature according to Eq. 3.37, the film thickness drops significantly, resulting in a lower separation between the two surfaces. Therefore the Stribeck curve shifts to the right. However, the friction force in EHL regime decreases due to a more severe decrease of viscosity than the film thickness (η/h_c in Eq. 3.25 is decreasing).

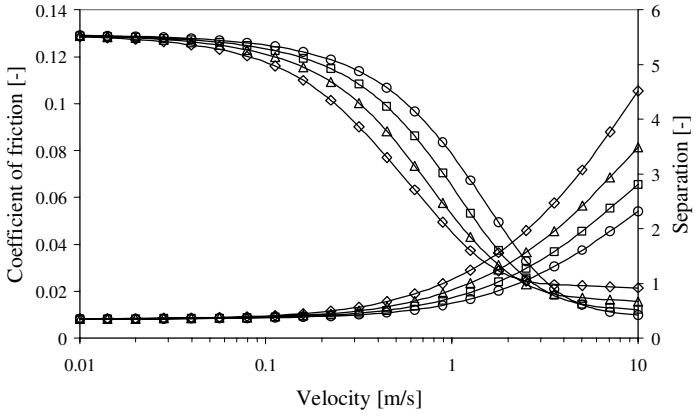

Fig. 3.19 The influence of the viscosity index, S_0, on the Stribeck curve and on the film thickness (h_c/σ) for an initial temperature of the lubricant of 40 °C: ◊ 0.5, Δ 1, □ 150 and ○ 2.

The same effect is noticed when the inlet temperature is increased, considering a lubricant with a viscosity - temperature index $S_0 = 1$ (Fig. 3.20).

In both of the latter situations, the thermal effect on the film thickness reduction factor (Eq. 3.38) is much less significant than the drop in film thickness due to the low inlet viscosity.

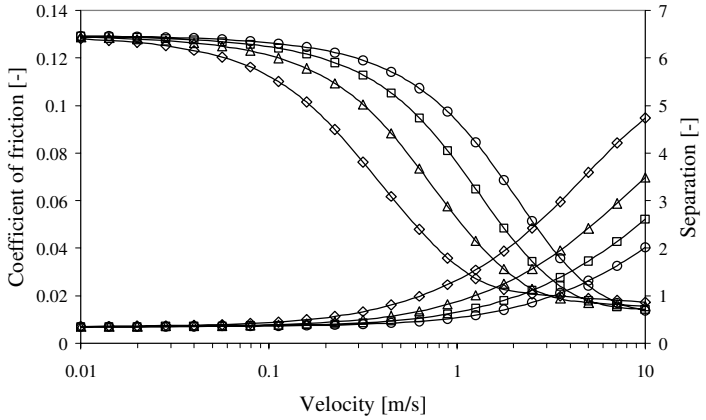

Fig. 3.20 The inlet temperature influence on the Stribeck curve and film thickness (h_c/σ) for $S_0 = 1$: ◊ 20, Δ 40, □ 60 and ○ 80 °C.

A final factor influencing the film thickness reduction factor (Eq. 3.38) in the EHL regime is the slip value (Eq. 3.21). Stribeck curves calculated for different slip values under the same input conditions as in previous discussions are plotted in Fig. 3.21.

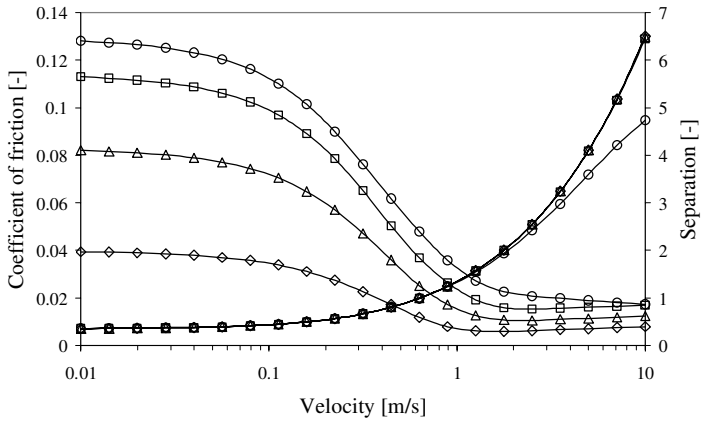

Fig. 3.21 Stribeck curve and film thickness (h_c/σ) reduction for different input slip values ($S_0 = 1$): ◊ 0.005, Δ 0.015, □ 0.05 and ○ 2.

The film thickness reduction factor (therefore the film thickness) decreases with increasing slip. Frictional heating effects become significant at high slip values (high differential velocity) where a decrease in friction is noted.

Other studies on the frictional heating influences on the coefficient of friction will be done when discussing the traction curves.

3.2.5.2 Traction curve

In section 3.1.6.2 the traction curve was introduced as the variation of the coefficient of friction with the slip (Eq. 3.21). The coefficient of friction is increasing from 0 (pure rolling) until it reaches the corresponding slip value as used in computing the Stribeck curve (Fig. 3.21). Several traction curves are plotted in Fig. 3.22, using different sum velocities as input.

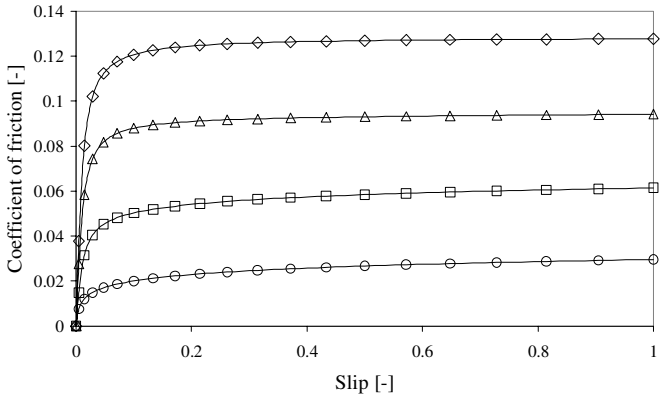

Fig. 3.22 Traction curve for different sum velocities: ◊ 0.01, Δ 0.2, □ 0.5 and ○ 10 m/s; for other input parameters, see Table 3.1.

For studying the frictional heating effect of the traction curve, traction curves are plotted under different loading conditions and lubricant properties at high velocity in order to achieve EHL. The same input parameters are used as given in Table 3.1 and Table 3.2. The heat source was considered to be elliptical and maximum temperature rise was adopted. In Fig. 3.23, for both isothermal and thermal cases, the coefficients of friction and separation are plotted as a function of slip, which was varied from 0 (pure rolling) until 2 (simple sliding). In the isothermal case, the coefficient of friction increases with increasing slip until it reaches its corresponding value on the Stribeck curve for simple sliding. The effect of normal load is that by increasing it, the traction curve shifts to the left for the isothermal situation. At simple sliding, the coefficient of friction has the tendency to increase when increasing the normal load at low loads and it tends to decrease at high loads. However, the variation in coefficient of friction at high loads is really small (see

Fig. 3.8). Of course, the film thickness stays constant for the whole slip range. In the thermal case, the normal load effect is similar (shifts the traction curve to the left around pure rolling point). On the high slip region, the increase in normal load has the effect of decreasing the coefficient of friction due to the film thickness reduction and to frictional heating influence on the viscosity when the friction force is calculated (Eq. 3.25).

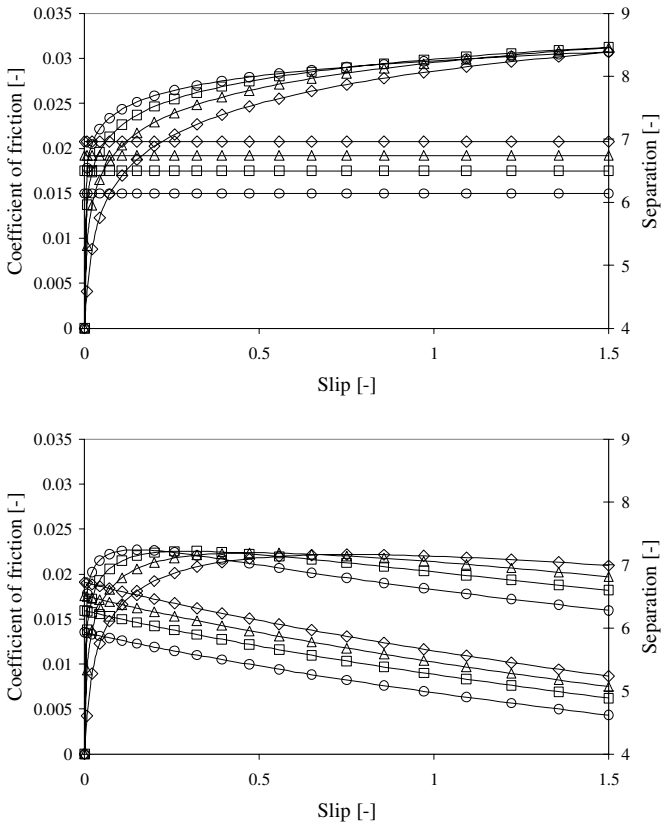

Fig. 3.23 Load influence of the traction curve and film thickness for isothermal (top) and thermal (bottom) cases (S_0 = 1): ◊50 (481), Δ 100 (606), □ 200 (763) and ○ 500 (1036) N (MPa).

Further, the influence of the temperature - viscosity index in the Roelands Eq. 3.37, S_0, is plotted in Fig. 3.24. Increasing the temperature - viscosity index results in a decrease in friction with increasing slip due to a decrease of the η/h_c factor.

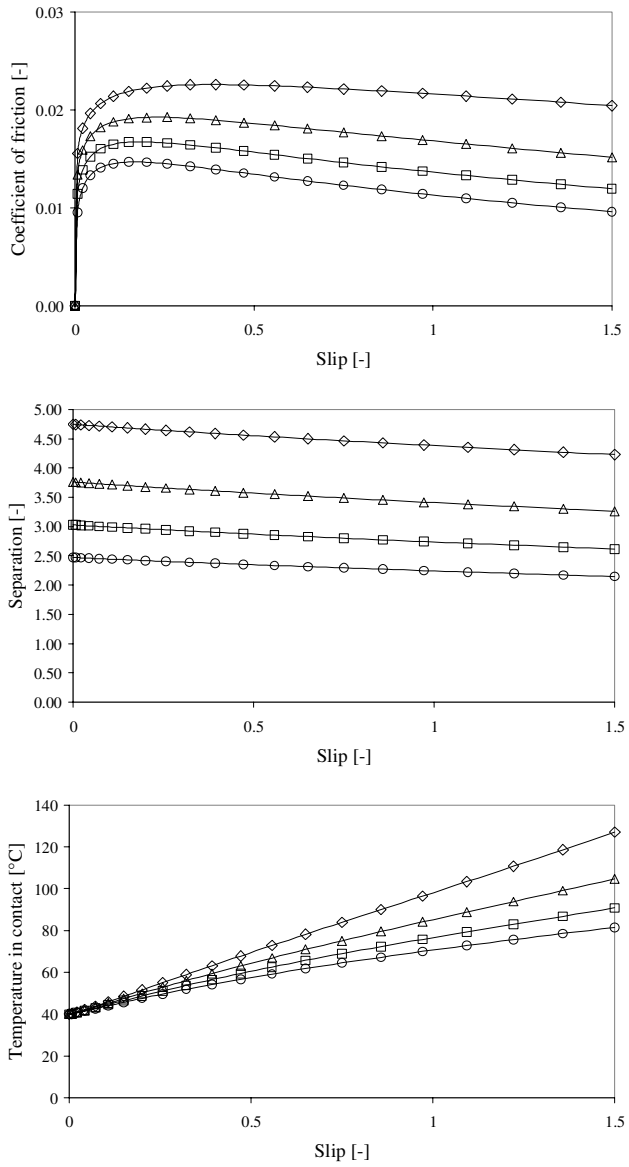

Fig. 3.24 Traction curve, film thickness and lubricant contact temperature for different temperature - viscosity index of the lubricant (T_i = 40; F_N = 500 N): ◊ 0.5, Δ 1, □ 1.5 and ○ 2.

The influence of frictional heating is observed by the negative slope at high slip values, when the temperature - viscosity index is high enough. This happens because the rate of heat flow (Eq. 3.35) is directly proportional with the differential

velocity and therefore with the slip. By increasing the slip, the frictional heating increases, so the viscosity in Eq. 3.37 decreases, leading to a drop in the coefficient of friction. When the initial oil temperature is included in the discussion, for a constant temperature - viscosity index, the results are different (Fig. 3.25).

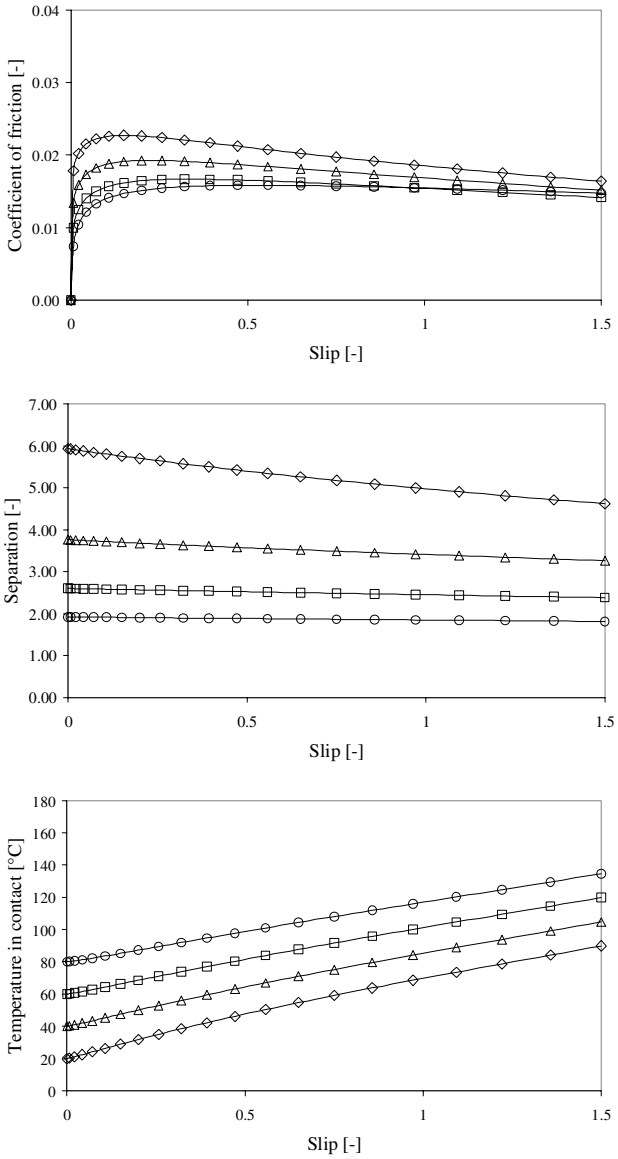

Fig. 3.25 Traction curve, film thickness and lubricant temperature in contact for different lubricant initial temperature ($S_0 = 1$; $F_N = 500$ N): ◊ 20, Δ 40, □ 60 and ○ 80 °C.

The prediction shows the frictional heating influence (negative slope at high slip) at low initial temperatures (high viscosity). This makes sense when the temperature rise due to frictional heating is smaller than the high initial temperature values considered. In this case, the temperature rise is small and therefore the separation doesn't decrease significantly with increasing slip value.

3.2.6 Conclusions

The ML friction model described in section 3.1.4 was extended to include frictional heating and film thickness reduction due to oil inlet temperature increase. The considered frictional heating model is the model of Bos and Moes [49] (Eq. 3.34) and the film thickness correction factor is chosen as given by Pandey [51] (Eq. 3.38). The model was applied to a tribo-system in which several parameters were varied: slip, sum velocity, load, lubricant inlet temperature and viscosity - temperature index. The model gives the possibility to study the combined effects of both frictional heating and the effect on the friction value in EHL considering film thickness reduction due to changes in lubricant inlet temperature. It was found that the frictional heating has an important effect on the friction level when the lubricant inlet temperature is close to ambient temperature. As the inlet temperature increases, the oil viscosity decreases and the main effect is an increase in friction in the ML regime followed by a decreasing friction in EHL. In the same manner, the film thickness is mainly controlled by the oil inlet temperature. As soon as this is significantly high, the correction factor has less influence on the film thickness and therefore on the separation.

3.3 Starved elliptical contact

Apart from the full film lubrication regime based on the fully flooded assumptions which, in fact, occupy most of the EHL research, starvation is a particular situation that was not investigated to the same extent, and almost not at all for the elliptical contacts. For the line contact, recent developments made by Faraon [54] generated a model capable of predicting Stribeck type curves for starved line contacts. The work was based on the findings of Wolveridge et al. [32], which proposed a film thickness reduction factor and the Stribeck curve predictions showed good agreement with the experiments.

3.3.1 The model

The same procedure as suggested by Faraon [54] is also followed here, starting with the work of Chevalier et al. [55], which presented a reduction factor for the film thickness due to starvation depending on the operational conditions M and L (Eq. 3.2 [37]) of point contacts. The reduction factor reads:

$$\Re = \frac{H_c}{H_{cff}} = \frac{r'}{\sqrt[\gamma]{1 + r'^{\gamma}}} \tag{3.42}$$

Where, $r' = H_{oil} / H_{cff}$ is the relative oil film thickness. If the compressibility of the lubricant is considered, r' can be replaced with $r = r' / \rho(P_H)$ when the density is calculated according to Dowson and Higginson [56], reading Eq. 3.43.

$$\rho(p) = \frac{0.59 \cdot 10^9 + 1.34 \cdot p}{0.59 \cdot 10^9 + p} \tag{3.43}$$

In [55] the fit factor γ from Eq. 3.42 was observed to vary between 2 and 5 for the EHL regime. An extensive numerical solution was developed by Damiens et al. [57] to determine how this factor is changing with the operational conditions M and L for elliptical contacts. The results of their calculations (Fig. 3.26) show that the fit parameter varies linear with $\sqrt{M/L}$ following different slopes for different ellipticity ratios, κ.

Based on Fig. 3.26, an empirical function fit for the factor γ is proposed further. Such formula would make the findings on the numerical solution in [57] to be used in engineering calculations and would also make it possible to use in the friction model presented in the previous sections for starved contacts.

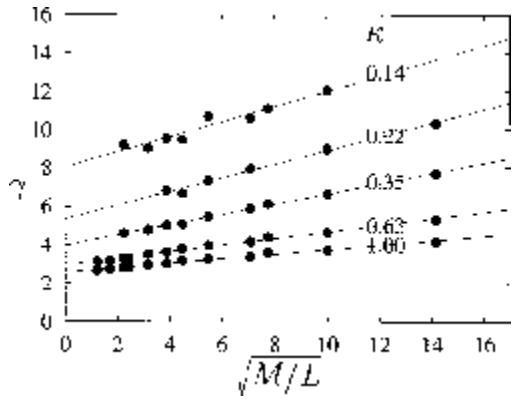

Fig. 3.26 γ as a function of operational conditions for different ellipticity values, κ (r = 1) [57].

Because the γ parameter varies with both ellipticity ratio, κ, and $\sqrt{M/L}$ the empirical relation between them will be done at a first stage by plotting ln(γ) as function of $\ln(\kappa)$ for two values of the $\sqrt{M/L}$, i.e. 1 and 16 (Fig. 3.27 b).

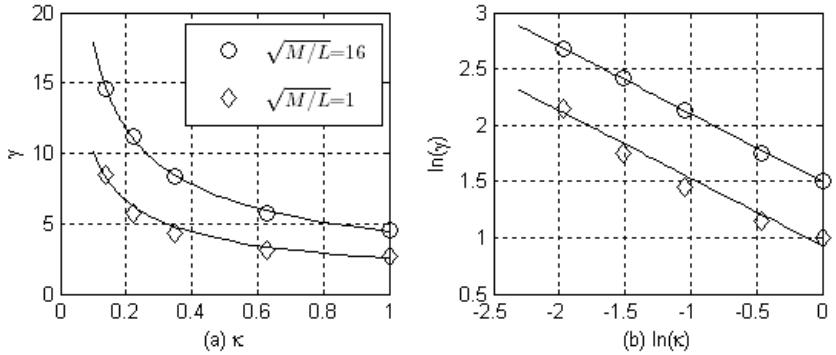

Fig. 3.27 Fit of variation of γ with ellipticity ratio κ for two operational conditions.

In the logarithmic plot, one may see that the two sets of data points lie on straight parallel lines. The points were fitted by using polynomial line fit of order one by the least squares method. The negative slope of both lines was calculated to be approximately −0.6 leading to a first dependency: $\gamma = c \cdot \kappa^{-0.6}$. Further, for c, a linear dependency was found: $c = 2.4 + 0.13 \cdot \sqrt{M/L}$. This results in a general formula for the γ parameter in the reduction film factor, Eq. 3.42:

$$\gamma = \left(2.4 + 0.13 \cdot \sqrt{\frac{M}{L}} \right) \cdot \kappa^{-0.6} \tag{3.44}$$

The film thickness (Eq. 3.19) used in the presented model is to be corrected with the starvation reduction factor (Eq. 3.42) in which γ is given by Eq. 3.44. Because the fit is based on the operational conditions factors M and L, which are also incorporated into the film thickness formula, no extra loop is required in the calculation scheme presented in Appendix D. Results of the starved model are presented in the next section.

3.3.2 Results of the starved model

Considering the same calculation as in the previous sections with the input data given in Table 3.1, the oil inlet thickness was varied such that the fully flooded EHL regime changed to the starved condition. In Fig. 3.28, Stribeck curves are plotted for different oil inlet thickness, which was normalized by dividing it with the standard deviation of the roughness i.e. h_{oil}/σ . When the inlet oil thickness is high enough, the EHL is similar to the fully flooded situation. If the available amount of oil in the inlet zone decreases (starvation), the coefficient of friction in EHL regime increases as the separation remains constant by being constrained due to the quantity of available oil in the inlet zone. Under severe starved conditions, the coefficient of friction can actually stay constant over the entire velocity range. This happens when the thickness of the supplied oil in the inlet zone is lower than the separation, given by the multi-asperity contact model, between the two contacting bodies.

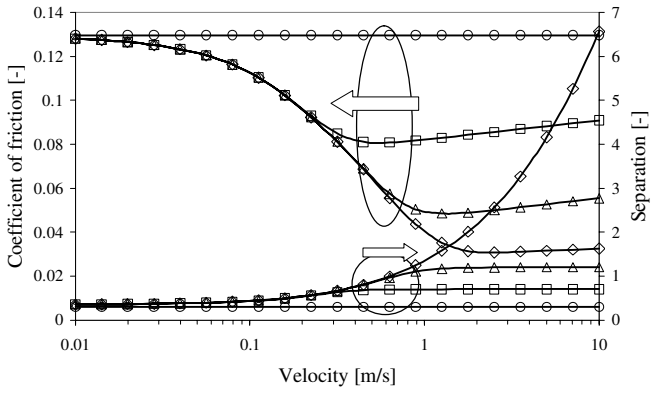

Fig. 3.28 Stribeck curve and dimensionless separation (h_c/σ) for different dimensionless oil inlet thickness, h_{oil}/σ: ◊ ∞, Δ 1.2, □ 0.7 and ○ 0.3.

Since the presented microcontact and friction model may become quite complex, by incorporating both frictional heating and starved conditions, a study of the combined effect of the two effects is proposed further. Choosing one calculation for a starved situation, from the above prediction (Fig. 3.28), for example, when

$h_{oil}/\sigma = 1.2$, the isothermal and thermal cases are plotted in Fig. 3.29. The used inputs are the same as given in Table 3.1 and the thermal related parameters in Table 3.2. For the frictional heating calculations, the heat supply is semi-ellipsoidal, considering maximum temperature rise (see Appendix C).

Following the prediction for the isothermal case (dashed line), clearly the starved EHL regime is observed when the separation remains constrained to the chosen normalized value of $h_{oil}/\sigma = 1.2$. If the change in oil inlet temperature is taken into account (continuous line), the film thickness reduces with the factor C given by Eq. 3.38. Subsequently, the load carried by asperities increases as there is not enough pressure in the film to sustain the same load, leading to an increase of the coefficient of friction. Due to frictional heating, as shown in section 3.2, the coefficient of friction reduces. Near the transition between the ML and EHL regimes a slight decrease in the coefficient of friction is noted. In this case, the effect of film thickness reduction due to starvation is less compared to the decrease in friction due to heating. At high velocities the effect of film thickness reduction is larger than the frictional heating effect.

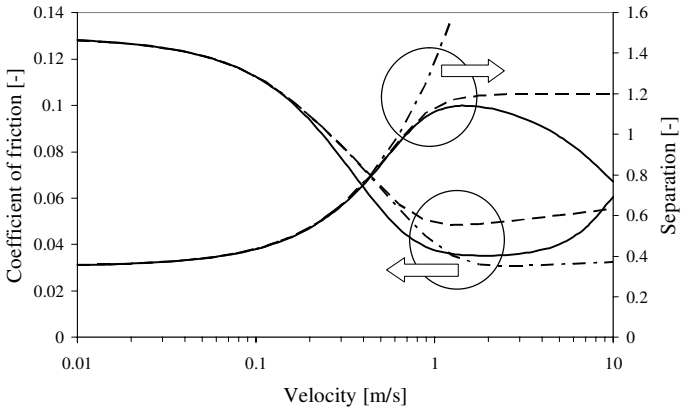

Fig. 3.29 Frictional heating influence on the Stribeck curve and separation (h_c/σ) under starved conditions. Isothermal (dashed line) and thermal, $S_0 = 1.5$ (continuous line); fully flooded isothermal (dash-dot).

Regardless of which effect has more impact on the Stribeck curve, the presented model includes both frictional heating and starvation, any combination of parameters being possible, without altering the calculation scheme presented in Appendix D.

With respect to the traction curve predictions, whereby a sum velocity of 10 m/s (EHL regime) is chosen, results are shown in Fig. 3.30 for the fully flooded and starved situations as well as isothermal and thermal situations.

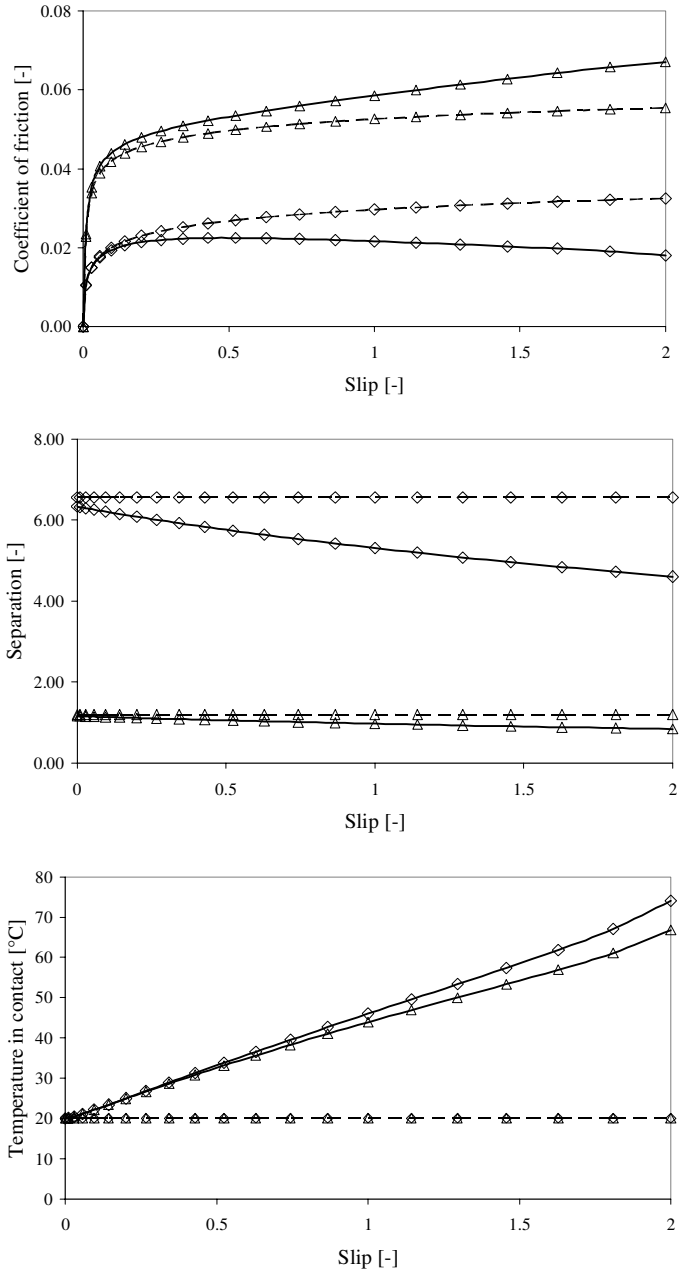

Fig. 3.30 Traction curves, separation (h_c/σ) and contact temperature for the starved model (sum velocity of 10 m/s and parameters as depicted in Table 3.1). Dimensionless oil inlet thickness, h_{oi}/σ, of: ◊ 10 and Δ 1.2 for the isothermal (dashed line) and thermal (continuous line) case.

In the full film regime, the used Eyring model (Eq. 3.23) shows an increasing slope of the traction curve over the entire slip (Eq. 3.21) range. When the frictional heating is taken into account, the coefficient of friction drops with increasing slip (or differential velocity) in most of the situations, showing a negative slope at high slip values, because the external normal load is entirely carried by the lubricant even with incorporating the film thickness reduction (effect discussed in section 3.2.5.2). Studying the frictional heating effects on the traction curve of a starved contact, the effect is opposite to the full film situation. Fig. 3.30 shows that with increasing slip value, the coefficient of friction increases even more. Judging that the film thickness limitation sets the load carried by lubricant to a fixed value, the slightly increasing slope at high slip is due to the nature of the considered shear model in the EHL regime, i.e. Eyring (Eq. 3.23). The effect of frictional heating is that the film thickness reduces to a lower value than the thickness of the available oil in the inlet zone, so the load carried by asperities increases, leading to an increase in the coefficient of friction.

3.3.3 Conclusions

The ML friction model (section 3.1), including frictional heating (section 3.2) and film thickness reduction due to inlet oil temperature increase (section 3.2.3), was extended by including starved conditions. An empirical film thickness correction factor is proposed (Eq. 3.44) based on the numerical model of Damiens et al. [57]. The model was applied to the same tribo-system as in previous sections and the effect of starvation is discussed.

3.4 Rolling with lateral slip

In most common situations, the contacting bodies of an elliptical contact have their radii of curvature, R_{1x}, R_{1y}, R_{2x} and R_{2y}, oriented to the principal axes: x in rolling direction and y in the direction perpendicular to rolling (Fig. 3.31 a). If that is the case, the contact area can be determined according to the Hertz theory summarized in Appendix E and the prediction of the Stribeck and traction curves is made as shown in the previous sections.

When one of the contacting bodies makes an attack angle Φ relative to the rolling direction (Fig. 3.31 b), the contact problem is more complicated (still Hertzian though) in the sense that the contact area will be different than the previous case and will make an angle φ_1 with the rolling direction of the first body (different than Φ). The contact area and its angle to the rolling direction, φ_1, are calculated according to general Hertzian theory as presented in [9].

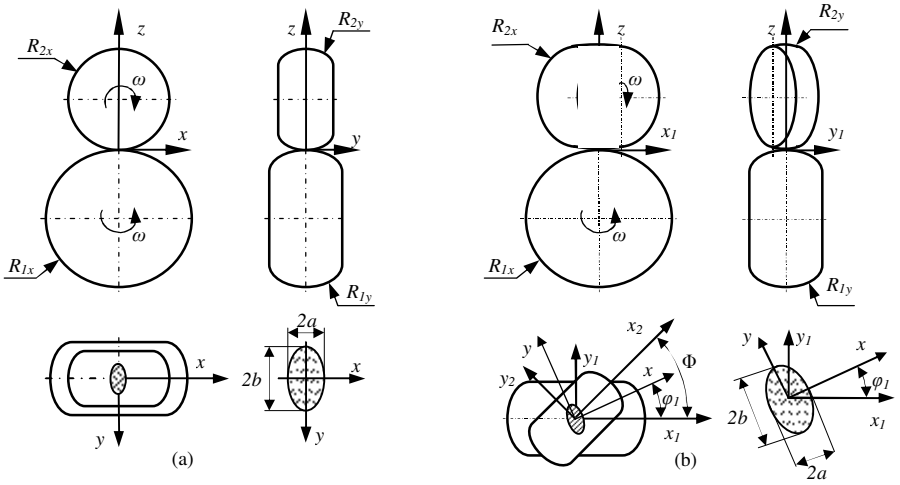

Fig. 3.31 Elliptical contact area when: (a) the contacting bodies have their principal radii of curvature oriented in the x (rolling) and y direction and (b) one of the bodies is inclined with an attack angle Φ relative to the x (rolling) direction.

Next to the contact area, ellipse size and direction, the slip in the contact also has to be recalculated and for the EHL component, the film thickness has to be corrected by considering the lubricant entrance at an arbitrary angle. These two factors will be discussed in the next two paragraphs.

3.4.1 Film thickness in EHL

For the elliptical contact, the film thickness in EHL regime was calculated according to Nijenbanning et al. [42] using Eq. 3.4 and in ML using Eq. 3.19.

Previous work of Chittenden et al. [58] recalculated the film thickness so it would consider the lubricant entrainment along the major axis of the contact ellipse or at some intermediate angle [59].

To start a discussion about how the film thickness is changing with the ellipticity ratio, Chittenden in [58], made this study based on the film thickness proposed by Hamrock and Dowson [60] which reads:

$$H_{\min} = 3.63 \cdot U_{\Sigma}^{\ 0.68} G^{0.49} W^{-0.073} \left[1 - \exp\left(-0.68 \cdot \kappa\right)\right] \tag{3.45}$$

Where, $\kappa = a/b \geq 1$ is the ellipticity ratio of the contact ellipse. Using numerical results, Chittenden et al. [58] fit a new film thickness formula as follows:

$$H_C = \begin{cases} 3.64 \cdot U_{\Sigma}^{\ 0.68} G^{0.49} W^{-0.073} \left[1 - \exp\left(-0.67 \cdot \vartheta^{-2/3}\right)\right] & \text{if} \quad \vartheta \leq 1 \\ 3.00 \cdot U_{\Sigma}^{\ 0.68} G^{0.49} W^{-0.073} \left[1 - \exp\left(-0.96 \cdot \vartheta^{-1}\right)\right] & \text{if} \quad \vartheta > 1 \end{cases} \tag{3.46}$$

Where $\vartheta = R_x / R_y$ is the gap curvature (ellipticity) ratio.

Later studies made by Popovici [61] showed that the formula of Nijenbanning [42] can be used for narrow EHL elliptical contacts. The film thickness derived by Nijenbanning [42] (used in this thesis) together with the Chittenden form ([58] Eq. 3.46) and the numerical predictions of Popovici [61] as a function of ellipticity ratio are shown in Fig. 3.32.

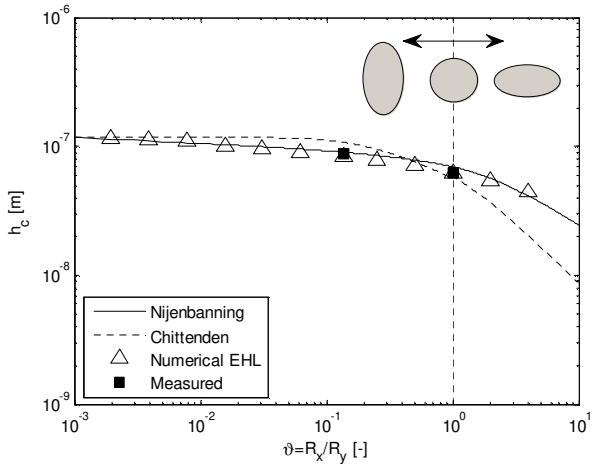

Fig. 3.32 Central film thickness as a function of ellipticity ratio after Nijenbanning [42] (continuous line), Chittenden [58] (dashed line). Both numerical results (Δ) and measured values (■) reproduced from Popovici [61].

Based on the comparison in Fig. 3.32, the film thickness formula of Nijenbanning [42] (Eq. 3.4) showed better accuracy when compared to Chittenden [58] even for narrow EHL elliptical contacts.

The question is: what happens when the oil flow is along some intermediate angle with either of the principal directions of the contact ellipse? An answer was proposed by Chittenden et al. [59] by fitting numerical calculations with:

$$H_C = H_{C0^\circ} \cos^2\theta + H_{C90^\circ} \sin^2\theta \tag{3.47}$$

Where, H_{C0° is the film thickness calculated for the situation when the entrance angle $\theta = 0^\circ$ and H_{C90° is the film thickness for $\theta = 90^\circ$. The angle θ is in fact the angle between the lubricant entrance vector and the minor axis of the contact ellipse [59], Fig. 3.33.

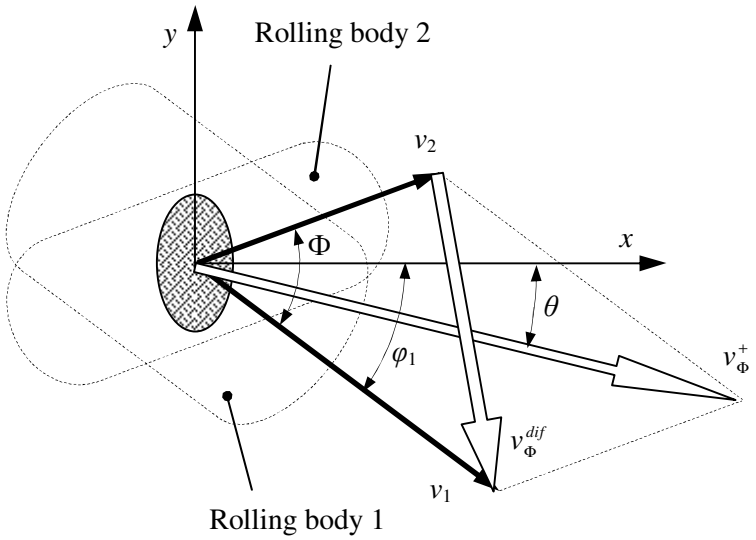

Fig. 3.33 Velocities of two rolling bodies with slip and side slip.

Chittenden et al. [59] calculated the angle θ, by projecting the surface velocity components of the two rolling bodies in the directions of the principal axes of the contact ellipse:

$$\tan\theta = -\frac{v_1 \sin\varphi_1 - v_2 \sin(\Phi - \varphi_1)}{v_1 \cos\varphi_1 + v_2 \cos(\Phi - \varphi_1)} \tag{3.48}$$

Having the angle determined, the film thickness is calculated with Eq. 3.47.

3.4.2 Velocity vectors and slip

When the bodies in contact roll with an arbitrary angle, Φ, the new sum and sliding velocities, v_Φ^{dif} and v_Φ^+, are calculated by using the cosine theorem in Fig. 3.33:

$$\begin{cases} v_\Phi^{dif} = \sqrt{v_1^{\,2} + v_2^{\,2} - 2 \cdot v_1 \cdot v_2 \cdot \cos\Phi} \\ v_\Phi^{+} = \sqrt{v_1^{\,2} + v_2^{\,2} + 2 \cdot v_1 \cdot v_2 \cdot \cos\Phi} \end{cases} \tag{3.49}$$

The slip or slide to roll ratio was previously defined as Eq. 3.21. In this case, it becomes:

$$S_\Phi = \frac{v_\Phi^{dif}}{v_\Phi^{+}} 2 \tag{3.50}$$

For convenience, the slip used as input in the friction model is chosen to be as given by Eq. 3.21, using the scalar values of the surface velocities of the two bodies. So the model will take as input, the slip value, $S = 2v^{dif} / v^+$, scalar sum velocity, v^+, and attack angle, Φ. So from these inputs, using the definition of slip Eq. 3.21, the velocities of the two bodies are calculated:

$$\begin{aligned} v_1 &= \frac{v^+}{4}(2+S) \\ v_2 &= \frac{v^+}{4}(2-S) \end{aligned} \tag{3.51}$$

Substituting v_1 and v_2 from Eq. 3.51, in Eq. 3.48, the angle of lubricant entrance into the contact ellipse is found as:

$$\tan\theta = -\frac{(2+S)\sin\varphi_1 - (2-S)\sin(\Phi-\varphi_1)}{(2+S)\cos\varphi_1 + (2-S)\cos(\Phi-\varphi_1)} \tag{3.52}$$

The same substitution, but in Eq. 3.49, leads to the new sum and sliding velocities:

$$\begin{aligned} v_\Phi^{dif} &= \frac{v^+}{2\sqrt{2}}\sqrt{4+S^2-(4-S^2)\cos\Phi} \\ v_\Phi^{+} &= \frac{v^+}{2\sqrt{2}}\sqrt{4+S^2+(4-S^2)\cos\Phi} \end{aligned} \tag{3.53}$$

And the lateral slip:

$$S_\Phi = 2\sqrt{\frac{4+S^2-(4-S^2)\cos\Phi}{4+S^2+(4-S^2)\cos\Phi}} \tag{3.54}$$

The dimensionless parameter U_Σ in Eq. 3.1, will be therefore corrected with the new sum velocity. So the film thickness, Eq. 3.19, will be calculated according to

the entraining velocity and then corrected by incorporating the entrance angle Eq. 3.52 into Eq. 3.47.

For including the lateral slip into the frictional heating model, the thermal correction factor on the film thickness, Eq. 3.38, has to be modified according to the new form of the lateral slip, Eq. 3.54 and the thermal loading parameter, Eq. 3.40, with the new sum in Eq. 3.53.

With respect to friction, the shear rate in Eq. 3.22 will change to:

$$\dot{\gamma}_{\Phi} = \frac{v_{\Phi}^{dif}}{h_c} \tag{3.55}$$

So the friction force in EHL, Eq. 3.25 will be calculated along the new shear rate vectors by using the definition of $\dot{\gamma}_{\Phi}$ given by Eq. 3.55:

$$F_{f,EHL} = \tau_0 A_H \operatorname{arcsinh}\left[\frac{\eta \cdot v^{+}}{2\sqrt{2}\cdot\tau_0 h_c}\sqrt{4+S^2-\left(4-S^2\right)\cos\Phi}\right] \tag{3.56}$$

The friction force in BL will be calculated by substituting the slip in Eq. 3.29 with the form given by Eq. 3.54:

$$F_{f,BL} = f_C F_C \frac{2}{\pi}\arctan\left[\frac{\pi}{S_{ep}}\sqrt{\frac{4+S^2-\left(4-S^2\right)\cos\Phi}{4+S^2+\left(4-S^2\right)\cos\Phi}}\right] \tag{3.57}$$

Once the friction force is calculated, the two friction force components in the considered directions can be calculated. In the wheel - rail contact situation, the principal directions along the track (X) and perpendicular to the track (Y) are of interest. Assuming the rail is the "Rolling body 1" in Fig. 3.33, the longitudinal and lateral friction forces are:

$$\begin{aligned} F_{fx} &= F_f \frac{\sqrt{2}}{2}\frac{2+S-\left(2-S\right)\cos\Phi}{\sqrt{4+S^2-\left(4-S^2\right)\cos\Phi}} \\ F_{fy} &= F_f \frac{\sqrt{2}}{2}\frac{\left(2-S\right)\sin\Phi}{\sqrt{4+S^2-\left(4-S^2\right)\cos\Phi}} \end{aligned} \tag{3.58}$$

3.4.3 Results of the rolling with lateral slip

Having the above parameters determined (contact area, shear rate and film thickness) for the situation when the attack angle between the two rolling bodies is changed, predictions for the traction curve in BL regime are plotted in Fig. 3.34 and Fig. 3.35. The same inputs are used as given in Table 3.1. The discussions are made based on the coefficient of friction and the dimensionless friction force

components $f_x = F_{fx} / F_N$ and $f_y = F_{fy} / F_N$, i.e. $f = \sqrt{f_x^2 + f_y^2}$.

In Fig. 3.34, the aforementioned parameters are plotted as a function of attack angle by changing the linear (scalar) slip value (Eq. 3.21).

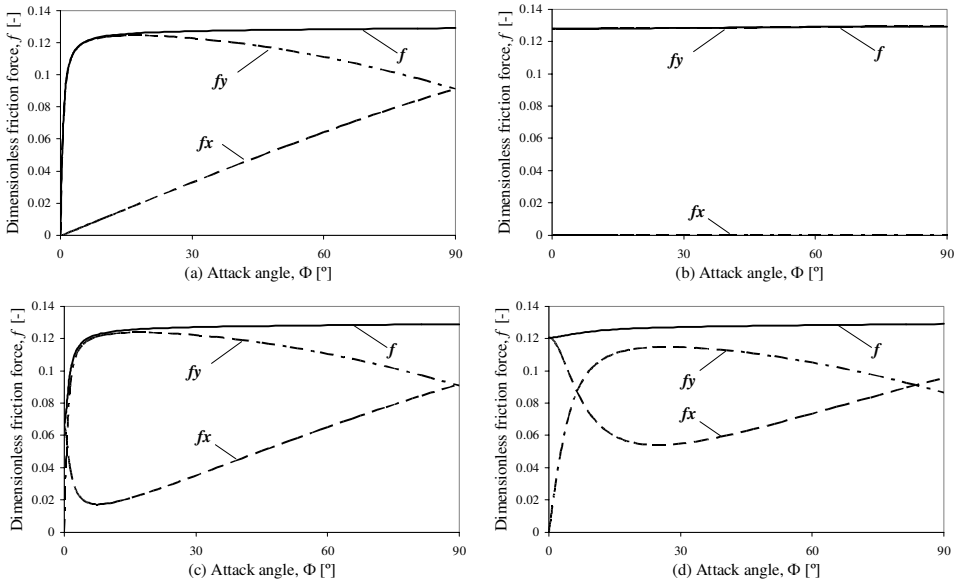

Fig. 3.34 Traction curves in the BL regime (S_{ep} = 0.015 and f_C = 0.13).
Slip of a) 0, b) 2, c) 0.01 and d) 0.1.

Considering the starting situation as pure rolling (Fig. 3.34 a), when the attack angle is increased the resultant coefficient of friction within the contact increases continuously until it reaches the value according to a theoretical attack angle of 90º. The two components vary both according to Eq. 3.58. While the longitudinal, x component increase slowly, the lateral friction force increases almost as much as the resultant one, at least in the first part of the curve. When the attack angle is increased more, the lateral component decreases to the value corresponding to the theoretical angle of 90º. At this point the two friction forces are equal.

Considering the other situation, when the slip defined by Eq. 3.21 is maximum, i.e. $S = 2$ (simple sliding situation, meaning that one of the contacting bodies is not rotating), regardless of the attack angle, the coefficient of friction in x direction has a constant value equal with the resultant one. Of course, the lateral component is zero (Fig. 3.34 b).

Intermediate cases ($0 < S < 2$, Fig. 3.34 c and d) show that the resultant coefficient of friction starts from the value on the traction curve according to the considered

slip, then increases over the entire angle range. The longitudinal component starts from the same value, decreasing with increasing attack angle, as the lateral component increases from zero.

The same three parameters are plotted as a function of slip for different values of the attack angle in Fig. 3.35.

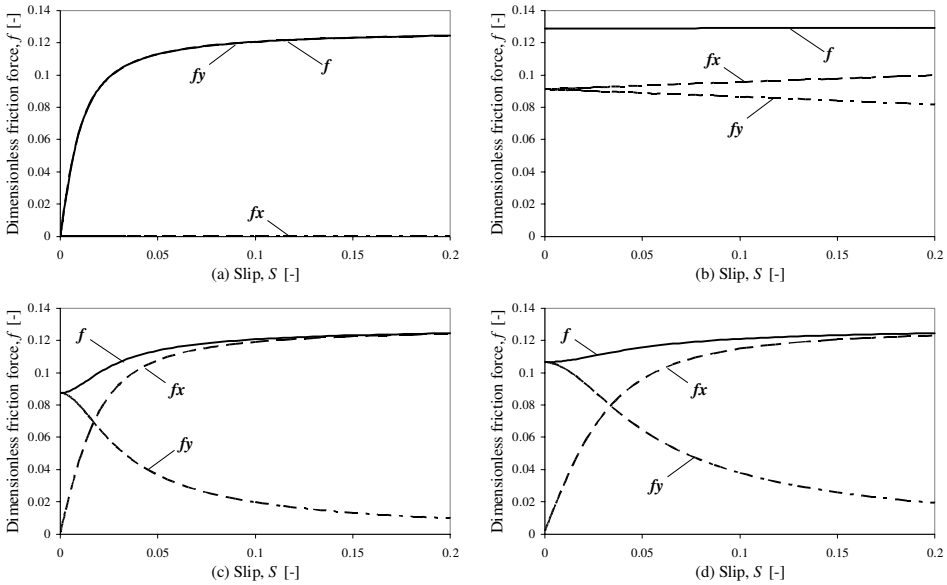

Fig. 3.35 Traction curves in the BL regime (S_{ep} = 0.015 and f_C = 0.13). Attack angle of a) 0º, b) 90º, c) 1º and d) 2º.

Fig. 3.35 (a) represents, in fact, a traction curve since the attack angle is zero (lateral component is zero). On the other extreme, at 90º (Fig. 3.35 b), starting from the same value as the saturation in Fig. 3.34 (a), the longitudinal component increases and the lateral decreases. Eventually the x component will reach the value of the resultant coefficient of friction when the slip will be $S = 2$. For intermediate values of the attack angle (Fig. 3.35 c and d) at zero slip the starting values for all friction components correspond to the values in Fig. 3.34 (a) and for the maximum slip situation, $S = 2$, will correspond to the values in Fig. 3.34 (b). With increasing the slip, the longitudinal, x component will increase and the y component will decrease.

On the other extreme, EHL lubrication regime, the most significant parameter which influences the friction when lateral slip is taken into account, is the film thickness. Of course, the contact area and pressure also changes when the attack angle changes.

The coefficient of friction in EHL regime (Fig. 3.36) shows the same dependency as a function of attack angle, Φ, and slip, S as for the BL results. It is interesting to note that the film thickness decreases with increasing attack angle, Φ.

The decrease is due to a combined effect of frictional heating and a change in ellipticity. When the attack angle is increased, the differential velocity, v_{Φ}^{dif} in Eq. 3.53 and the angular slip, S_{Φ} Eq. 3.54, will also increase, so the thermal correction factor for the film thickness in Eq. 3.38 will decrease.

If the linear (scalar) slip value (Eq. 3.21) is maximal, i.e. $S = 2$, the only parameter which can influence the film thickness is the angle of the lubricant entrance with the principal directions of the contact ellipse. Due to the shape of the contact as presented in Table 3.1, at an angle of attack of 0º, the contact ellipse is wide. So with increasing the attack angle the film thickness decreases. At 90º, the contact ellipse is narrow and the film reduces since more side flow effects take place. This behaviour is in agreement with the findings of Chittenden et al. [59].

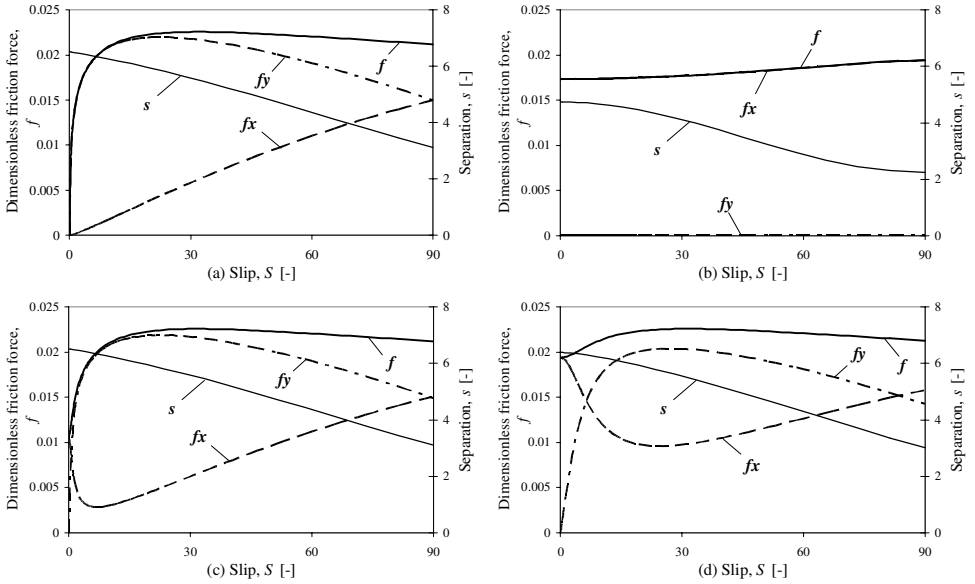

Fig. 3.36 Influence of the attack angle of the coefficient of friction and film thickness (h_c/σ) in EHL regime (thermal, $S_0 = 1$). Slip of a) 0, b) 2, c) 0.01 and d) 0.1.

Plotting traction curves using different attack angle values for the EHL regime, show a similar behaviour as for the BL regime (Fig. 3.37). For a given attack angle, the film thickness does not reduce significantly for the considered scalar slip values, i.e. $S = 0 \div 0.2$. However, the decrease at high slip values is of the same significance as in the case of high attack angles.

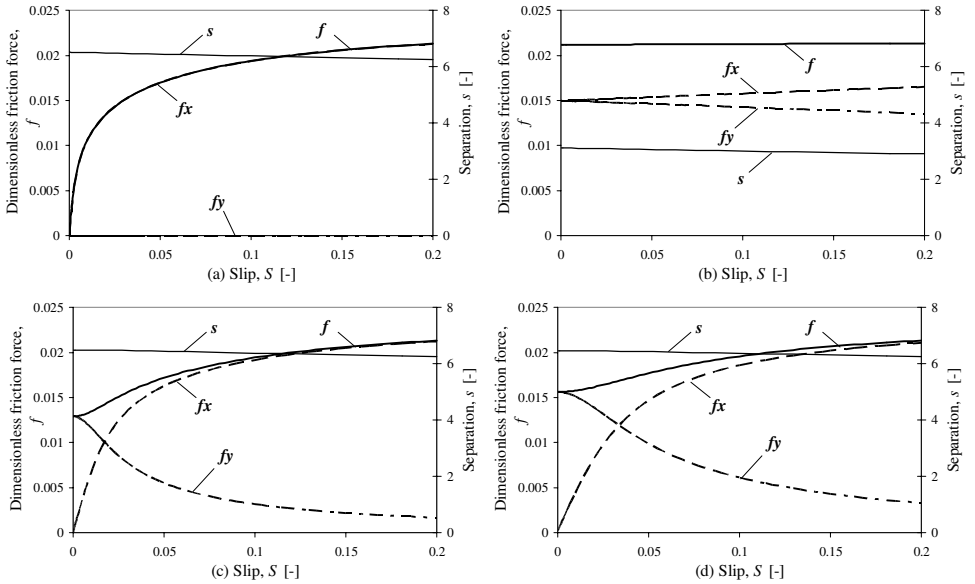

Fig. 3.37 Traction curves and separation (h_c/σ) in the EHL regime (thermal, $S_0 = 1$). Attack angle of a) 0º, b) 90º, c) 1º and d) 2º.

3.4.4 Conclusions

The friction model presented in section 3.1 was updated by introducing the influence of the attack angle. The film thickness formula was corrected according to Chittenden et al. [59]. The shear rate used in the Eyring shear stress model (Eq. 3.23) was also adapted. Finally, the influence of the attack angle was also included into the thermal correction factor for the film thickness, Eq. 3.38. Results considering frictional heating, for the same case as in Table 3.1 supplemented with the attack angle input, were predicted and discussed and it turned out that the attack angle influence on the traction curve has the same trend for the EHL as well for the BL regime.

3.5 Conclusions on the friction model

A deterministic microcontact and friction model is presented by which Stribeck and traction types of curves can be predicted for the elliptical contact situation. Inputs into the model are surface roughness, material properties and functional parameters (normal load, sum velocity, slip and attack angle) together with the rheological properties of the interfacial layer. Frictional heating and starvation effects were also taken into account.

Chapter 4

Model Validation

4.1 Introduction

Theoretical models need to be experimentally validated. Although lubricated concentrated contacts were experimented with very extensively, i.e. [45], [62], [63], this study covers friction measurements over a wide range of velocities. Combined with the surface roughness and lubricant rheological properties, the coefficient of friction for all three (EHL, ML and BL) regimes is measured.

4.2 The setup

The most suitable experimental setup for testing the model is the two disk machine. It represents a robust system, capable of high loads and high velocities. A secondary device is used (pin-on-disk tribometer) for verifying the model at low scale application where the loads are much smaller.

Because the above-mentioned two devices are well known, they will not be described thoroughly. However, some important data about both tribotesters is presented further.

4.2.1 Two disk machine

This apparatus (Fig. 4.1) is fully automatic and capable of measuring the traction curves i.e. friction as a function of slip. The slip is controlled by adjusting the rotational speed of each individual motor but keeping the sum velocity constant.

The main issue encountered during the experiments was the low slip region. A measured traction curve showed that the coefficient of friction reaches its

maximum value when the slip is lower than 5%. To achieve such precision, especially at low velocities, two gearboxes were inserted between the motors and the disks. The gearboxes are in two steps configuration with a constant gear ratio of 27.63. Such a combination allowed the study of friction in the BL regime.

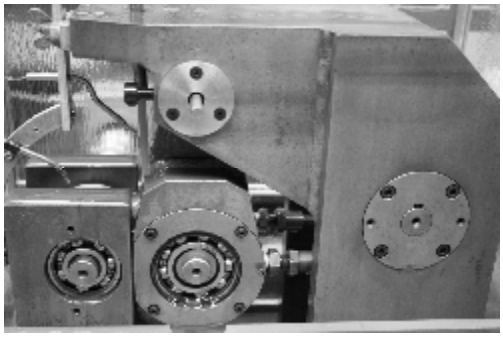

Fig. 4.1 The two disk machine.

Table 4.1 specifies the geometry of the disks as well as the operational parameters of the two disk machine tests.

Table 4.1: Two disk machine setup.

Property	Value	Unit	Description
R_x	19.125×10^{-3}	m	Radius in x (rolling) direction
R_y	50×10^{-3}	m	Radius in y direction
F_N	150, 250, 350	N	Normal load
p_m	0.5, 0.6, 0.67	GPa	Mean contact pressure
v	4, 6, 8	m/s	Sum velocity

4.2.2 Pin-on-disk tribometer

In the pin-on-disk setup, Fig. 4.2, the pin is stationary and the disk turns with variable speed while the normal load is controlled by a dead weight of 10 N.

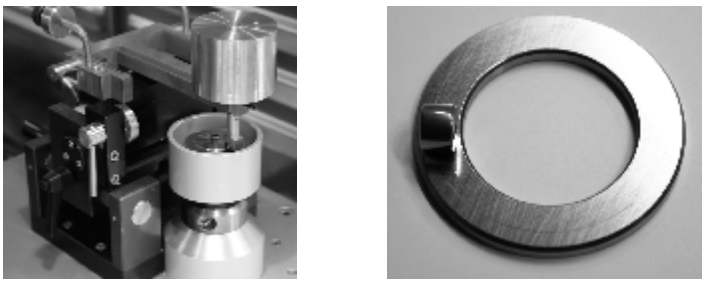

Fig. 4.2 Pin-on-disk tribometer and the studied parts.

The elliptical contact was realized by using an ellipsoid shaped specimen pressed against the rotating disk.

Table 4.2 summarizes the operational conditions and contact geometry of the pin-on-disk setup.

Table 4.2: Pin-on-disk setup.

Property	Value	Unit	Description
R_x	4×10^{-3}	m	Radius in x (sliding) direction
R_y	26.67×10^{-3}	m	Radius in y direction
F_N	10	N	Normal load
p_m	0.455	GPa	Mean contact pressure
v	0.001... 1	m/s	Velocity

4.3 Other inputs

To complete the two considered tribo-systems, the lubricant properties must be specified and the surface topography of the used specimens must be measured and exported in such way it can be used in the model.

4.3.1 Lubricant

The lubricant used is an industrial mineral oil HVI160 which was chosen because it was extensively studied [45] and therefore its rheological properties are well known.

4.3.1.1 Viscosity

Being the most important rheological property of the lubricant, the viscosity and its dependency of pressure and temperature is well known for this predominantly paraffinic oil. The viscosity is considered to vary with pressure and temperature according to Roelands [43] (Eq. 3.3). The parameters related to the viscosity of the lubricant are shown in Table 4.3.

Table 4.3: Lubricant (HVI160) properties [45].

Property	Value	Unit	Description
η_0	0.293	Pa·s	Viscosity at ambient pressure (T_0 = 20 °C)
z	0.63	-	Roelands pressure-viscosity index
S_0	1.24	-	Temperature viscosity index

4.3.1.2 Eyring shear stress

Several traction curves were measured in the EHL regime for different contact pressures and sum velocities. From these curves, the Eyring shear stress was determined.

In order to extract the rheological properties of the tested lubricant, the traction curve is plotted as the shear stress (Eq. 4.1) as a function of the natural logarithm of the shear rate (Eq. 3.22).

$$\tau_H = \frac{F_{f,EHL}}{A} \tag{4.1}$$

$$\dot{\gamma} = \frac{v^{dif}}{h_c} = \frac{S \cdot v^{+}}{2 \cdot h_c} \tag{4.2}$$

The film thickness in the shear rate formula was determined using the Nijenbanning et al. [42] film thickness formula for elliptical contacts.

When the traction curve is plotted as presented in Fig. 4.3, the inclination of the tangent in the inflection point of the curve fitted through the data points reads the value of the Eyring shear stress, (Eq. 4.3) and the intersection between this tangent and the x-axis reads the viscosity at testing conditions, (Eq. 4.4).

$$\frac{d\tau_H}{d[\ln(\dot{\gamma})]} = \tau_0 \tag{4.3}$$

$$\ln(\dot{\gamma}) = \frac{\tau_0}{2 \cdot \eta} \tag{4.4}$$

This procedure applies for EHL contacts where the Eyring model is used (Eq. 3.23). In this present case a fourth order polynom was fitted through the data points. On the right Y axis (Fig. 4.3) the first and second derivative of that polynom were plotted. The second derivative was used to find the inflection point of the curve fit.

Taking into account all conducted measurements and assuming the temperature in the contact is constant for each experiment (the parameter τ_0 and η are obtained from the low slip part of the traction curve), it is observed that the Eyring shear stress was varying with pressure and sum velocity. In the case of viscosity, the influence of velocity was insignificant (within the tested velocity range), so the only parameter to extract was the Roelands pressure-viscosity index, z, which was in agreement with the value given in Table 4.3.

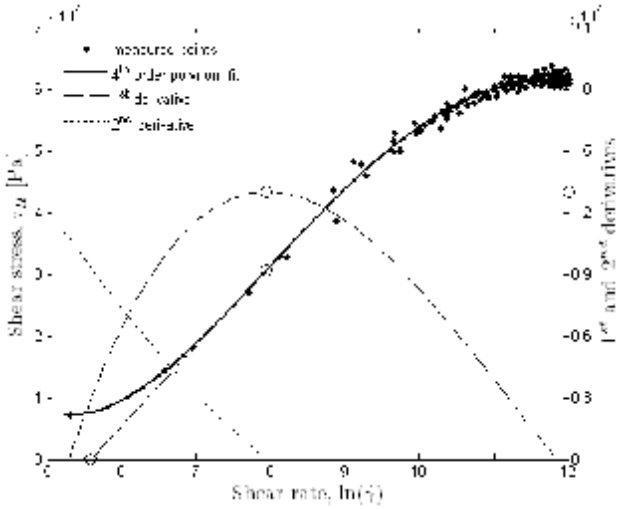

Fig. 4.3 Rheological parameter extraction from the traction curve.

The determined Eyring shear stress varied with the velocity and pressure as shown in Fig. 4.4.

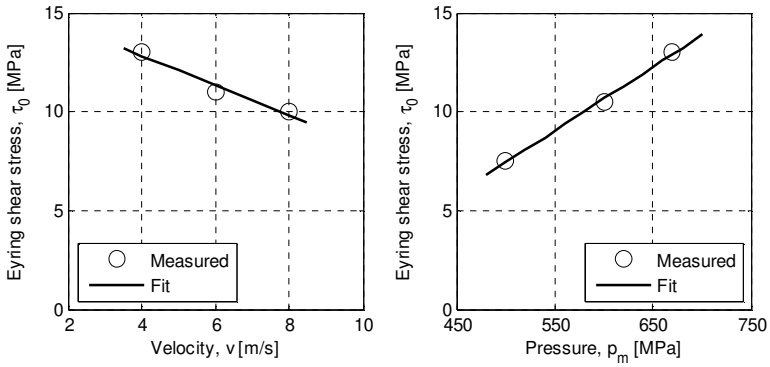

Fig. 4.4 The variation of Eyring shear stress with the sum velocity and mean contact pressure.

Considering the extracted values for the conducted experiments, a function fit is proposed for the Eyring shear stress, Eq. 4.5.

$$\tau_0(p,v)=\tau_0^* + \left(p - p_0^*\right)\cdot tg\left(\alpha_p\right) + \left(v - v_0^*\right)\cdot tg\left(\alpha_v\right) \tag{4.5}$$

Where, τ_0^* is the Eyring shear stress obtained at the reference pressure p_0^* and velocity v_0^*. The $tg(\alpha_p)$ and $tg(\alpha_v)$ are the slopes of the Eyring shear stress as a function of pressure and velocity respectively. The obtained parameters are summarized in Table 4.4.

Table 4.4: Reference and parameters for the variation of the Eyring shear stress with pressure and velocity (HVI160).

Property	Value	Unit	Description
τ_0^*	13	MPa	Reference shear stress
p_0^*	0.67	GPa	Reference pressure
v_0^*	4	m/s	Reference sum velocity
$tg(\alpha_p)$	3.22×10^{-2}	-	Shear stress - pressure slope
$tg(\alpha_v)$	-7.5×10^{5}	-	Shear stress - velocity slope

4.3.2 Surface topography

The roughness of the disks used and ellipsoidal shaped pin were measured after conducting the experiments, using an interferometer. After the surface roughness measurement, the surface is exported in three coordinates, x and y representing the position of a specific point on the surface and z the distance from the mean plane to the real surface.

The summits of the surface are identified and then two radii are determined for each summit. This is done by using the 9-point summits definition [44], i.e. a point is regarded as a summit if the 8 surrounding points are lower.

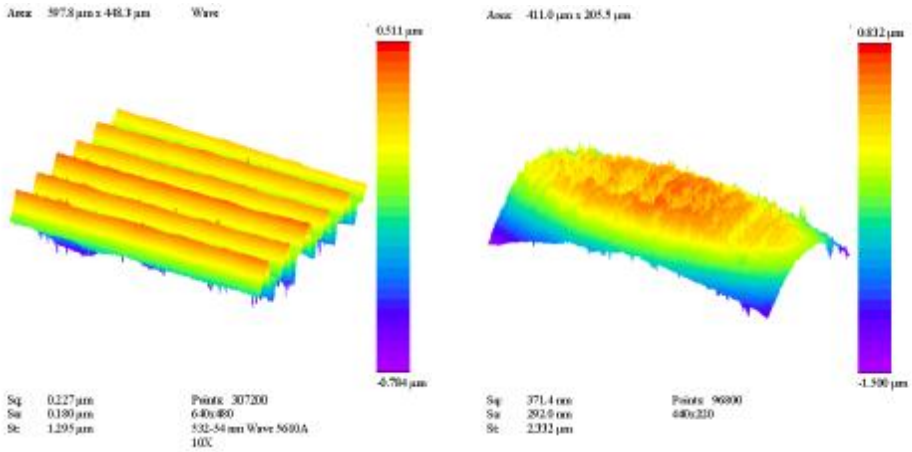

Fig. 4.5 Surface topography of the disks used on the 2 disk machine and ellipsoid shaped pin used on the pin-on-disk tribometer.

Fig. 4.5 depicts the surfaces of the two specimens measured at the end of an experiment. These surfaces were used in the model.

4.4 Measurements

The measurements were divided in three parts. Starting with full film lubrication tests on the two disk machine, traction curves were measured at high sum velocity. After installing the two gearboxes, low sum velocity tests were performed in order to cover the BL regime. And finally, simple sliding tests were performed on the pin-on-disk tribometer.

4.4.1 Full film traction curves

The Eyring shear stress was determined from the full film traction curves plotted as in Fig. 4.3. However, for a good model validation, the variation of the coefficient of friction as a function of slip is also important because it gives information about the thermal region of the traction curve.

When using the frictional heating model of Bos and Moes [49] the present case fits into the situation described by an elliptical contact area and a semi-ellipsoidal heat source.

In Fig. 4.6, three traction curves, measured and calculated, are plotted at different sum velocities and constant contact pressure. It is obvious that if there is an increase in the sliding velocity, therefore the slip value, the frictional heating increases and the coefficient of friction decreases.

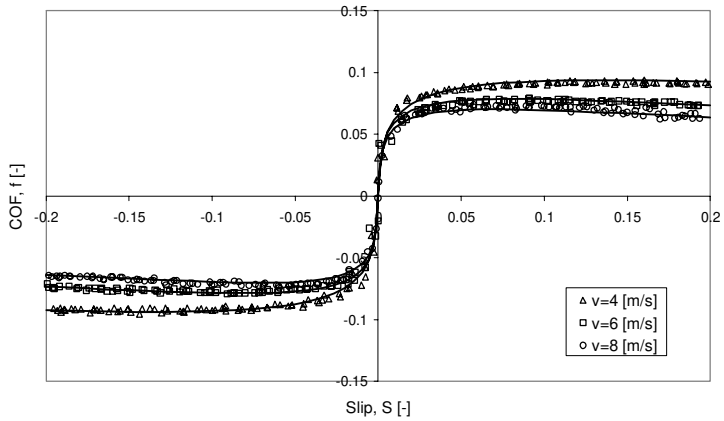

Fig. 4.6 Traction curves at normal load of 350 N (p_m = 671 MPa) for three sum velocities: Δ 4 m/s, □ 6 m/s and ○ 8 m/s. Experimental results and model predictions.

When increasing the normal load, the coefficient of friction in the EHL regime increases (Fig. 4.7). At high slip values, the frictional heat increases, resulting in a slight decrease in friction.

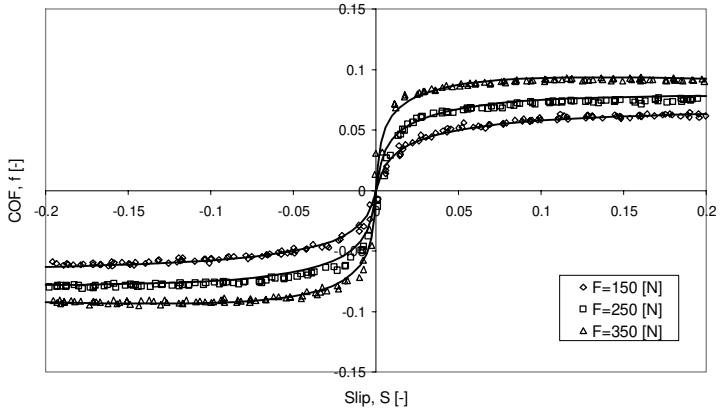

Fig. 4.7 Traction curves at sum velocity of 4 m/s for three normal loads:
◊ 150 N (p_m = 506 MPa), □ 250 N (p_m = 600 MPa) and Δ 350 N (p_m = 671 MPa).
Experimental results and model predictions.

The observed frictional behaviour is in line with those reported in [45], [62] and [63] for lubricated circular and line contact.

Both measured series of curves are well described by the model, good agreement is found in the experiments.

4.4.2 Boundary lubrication traction curves

Three cases experimented with the described setup configuration, see section 4.2.1, at three low sum velocities: 0.036, 0.072 and 0.11 m/s. Assuming the tribo-system with the test conditions given in Table 4.1 and lubricant properties in Table 4.3, the system functioned in the BL regime. The Coulomb coefficient of friction of the boundary layer, for this tribo-system, was found to be f_C = 0.175.

Further, using the ML model (Eq. 3.31) and considering the aforementioned value for f_C, the slip value at the transition from elastic to plastic behaviour of the boundary layer, S_{ep}, was found to vary between 0.0125 and 0.0165. An average value of S_{ep} = 0.014 is taken in further calculations.

The measured values and the model predictions are shown in Fig. 4.8. Model results were found to be in good agreement with the measured values.

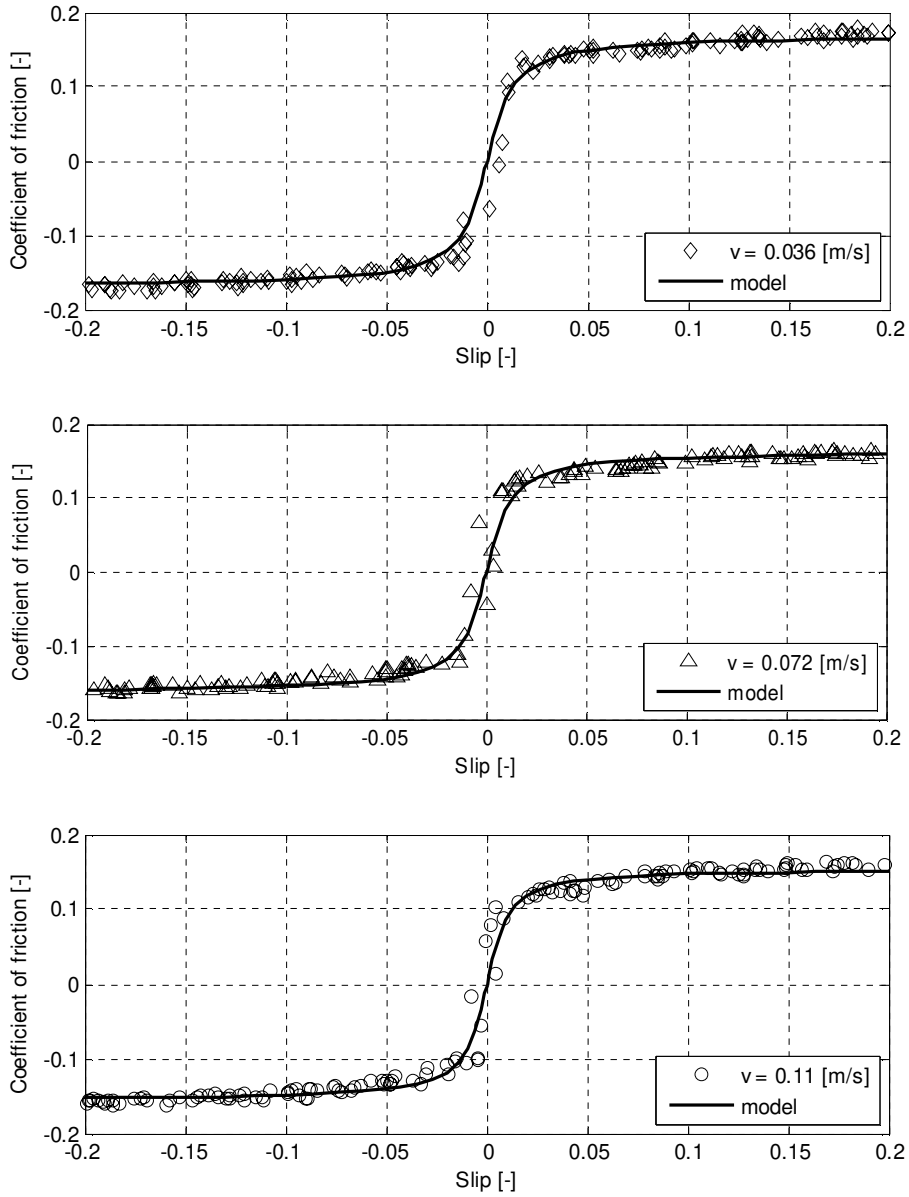

Fig. 4.8 Boundary lubrication traction curves at a normal load of 350 N (p_m = 671 MPa) for three sum velocities: Δ 0.036 m/s, □ 0.072 m/s and ○ 0.11 m/s. Experimental results and model predictions (f_C = 0.175 and S_{ep} = 0.014).

4.4.3 Stribeck curves

In Fig. 4.9, the model prediction, using the values presented in Table 4.2 and Table 4.3, is plotted together with the measured Stribeck curve (pin-on-disk tests).

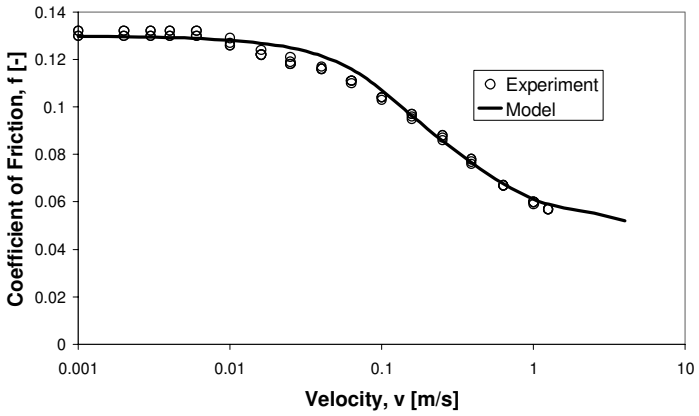

Fig. 4.9 Stribeck curve. Model and experimental results, see Table 4.2 and Table 4.3 for the test conditions and the lubricant properties.

For this tribo-system (ellipsoid shaped pin, disk, HVI160), a Coulomb coefficient of friction of the boundary layer $f_C = 0.13$ (Eq. 3.29) showed good agreement with the measurements. A small difference in the slope of the ML regime is observed. In the experiment, the transition between the BL and ML regime is smoother than predicted by the model.

4.5 Conclusions

This chapter verifies the theoretical friction model for highly loaded lubricated elliptical contacts including frictional heating.

The model predicts the coefficient of friction as a function of several parameters (Eq. 3.31 and 3.21) for mixed lubricated elliptical contacts represented in the so-called Stribeck and traction curves. The formula given by Eq. 3.31 allows the calculation of such curves for the BL and ML regimes by using the fit parameter, S_{ep}.

Experiments were carried out using two different tribometers. The model showed to be in good agreement with the measured friction values.

Chapter 5

Field measurements

5.1 Introduction

In relation to the railroad, there are four questions to which researchers must find solutions to formulate answers:

1. What causes low friction?
2. What is the optimum slip to reach maximum levels of friction?
3. How is the velocity of the train influencing the friction?
4. Where and when is low friction?

From a tribological point of view, a traction curve measurement of the slippery layer on a real track is of utmost importance since it will give an answer to the first questions in terms of rheological properties of that layer. Therefore, the possibility of measuring traction curves, i.e. coefficient of friction as a function of slip, will formulate the main target of the tribometer to be used. The measured traction curve will give insight on the slip value for which the coefficient of friction is maximum and finally, traction and Stribeck curve measurements on a real track will validate the presented microcontact and friction model for the wheel - rail contact.

The need to know the location and the time of low friction (4^{th} question) is presented here as a secondary target, without undermining its importance though. This would have an influence on the driver's behaviour, therefore a direct practical effect on how trains run in service. In fact, the posing of this question represents the need to have a low friction detection system on a train. Having such a detection system would eliminate the situation in which drivers are taking precautions even when the tracks are in good friction condition.This is an aspect that will improve the performance of the train operator by minimizing delays.

This chapter presents the most important already available measuring tools capable of acquiring friction-related data from the rails. Based on this survey, two tribo-testers connected to a train are discussed, i.e. the sliding tester and the tribometer.

5.2 Orientation

In the railroad industry, the friction was investigated in different ways. The approach was to measure the coefficient of friction for different values of slip after applying friction modifiers (ex.: flange lubricants) and also to see how long the effects last, for what distance the lubricant is carried by the wheels, etc.

Of course, the same devices can serve the low friction issue. For a list of possibilities to measure the friction in wheel - rail contacts and also for a practical review concerning the existing level of research in low friction, the reader is referred to [64]. Four of the existing measuring devices are presented below in terms of references, operating principle, advantages, disadvantages and conclusions.

5.2.1 Hand tribometer

This device is a hand-pushed tribometer designed for "Spot Checking Lubrication Effectiveness". The tester (Fig. 5.1) was developed by Salient Systems, Inc. [65] and the concept and some measurements are presented in detail in [66].

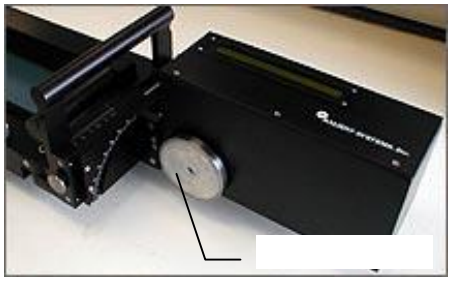

Fig. 5.1 Hand-pushed tribometer [66].

The operating principle of this tribometer is to progressively increase the braking torque of the measuring wheel until slip occurs. The value of the coefficient of friction is then calculated from the peak torque and the onset of slip. In terms of advantages, the hand-pushed tribometer is very light and environmentally friendly, and is easy to transport to the desired location. It is used for investigation purposes by using a reference "by heart" on what slippery means, meaning that it gives information about the friction level in terms of "slippery" or "not slippery".

The main issue of this tribometer is the scale. Usually the measurements taken with

it, in terms of coefficient of friction values, are higher than the real values existing in wheel - rail interface. Between real wheel - rail tribo-system and the set used by this tribometer there is no good relation available, therefore scaling the measurements in order to have the real data is impossible. Also, it doesn't incorporate the slip in the measurement and the velocity range is restricted to walking speed. Therefore, it is concluded that the presented tribometer is not suitable for model validation.

5.2.2 High Speed TriboRailer

The tester named TriboRailer (Fig. 5.2) was developed by Salient Systems, Inc. [65] and the concept and some measurements are presented in detail in [66].

Fig. 5.2 TriboRailer [66].

The operating principle of this tribometer is the same as with the hand-held tribometer, the only difference being that the high speed tribometer saturates the traction curve by inducing lateral slip (2.5%) by steering the measuring wheel.

Noted as a main advantage is that it calculates the coefficient of friction with the recorded values from the load cells (important, because the friction in the ball bearings doesn't influence the measurement). It can acquire data from both rails during one pass at velocities up to 45 km/h (much higher than the previous presented tester) and has automated data collection for coefficient of friction, velocity and location (GPS).

On the other hand, the main major disadvantage is that the simple sliding conditions are not reproduced, but theoretically assumed to be identical with the situation of 2.5% lateral slip. Therefore it is not suitable for traction curve measurements because it cannot give real information about the longitudinal slip value at which the coefficient of friction has its maximum. Due to the fact that traction curve measurements are not possible, no characterization of the interfacial layer is possible.

5.2.3 Surveyor

The tester developed by Portec Rail Inc. [67] was called “Surveyor High Speed Rail Tribometer” and the patented invention is presented in [68]in detail. A quick description of the measurement process will be presented further.

While the entire frame is pushed along the track by a conventional high-railer type vehicle, the measurement wheels roll along the rail. The coefficient of friction is measured on the tread surface of the rail and on the gauge surface by applying a dynamic braking torque with servomotors. When the desired slip is achieved or just before sliding occurs, the coefficient of friction is computed and the brake is released. Then, the cycle is repeated.

Fig. 5.3 Surveyor [68].

As a main advantage, the tribometer can incorporate configurations for measuring both tracks in a single pass, and the spin if required, as well as other measuring devices (weather station, GPS etc.).

The working principle leads again to a discontinuous measurement (one value every two seconds), the value of the coefficient of friction being processed in locations situated roughly between 30 and 80 metres by measuring the braking torque. Here the coefficient of friction is calculated based on the applied braking torque which also takes into account the friction between different parts of the entire assembly.

The construction is complex and very large and it is necessary to use a special vehicle for pushing it along the track. That is why this tribometer is suitable only for service usage, not for research purposes. Also, the measuring principle is not appropriate for achieving the aforementioned targets.

5.2.4 British Rail’s tribometer

The full scale tribometer train [69] was developed by British Rail in 1975. Its working principle is briefly presented below. On a bogie, a brake was mounted, isolated from the rest of the break system, which made independent braking of the axles of the bogie possible. The braking system was not used for torque measurement. During one measurement the braking force is increased linearly until

wheel slide occurs. On that moment the coefficient of friction is calculated measuring the normal and longitudinal load on the axles by a traction rod force for the longitudinal component and a damper force for the normal component. Furthermore, the break is released and the cycle is repeated.

The main advantage is that being a full scale tribometer the train doesn't have to "simulate" the wheel rail contact, but in fact the measuring wheel is a real train wheel. The coefficient of friction is computed with the measured normal and longitudinal forces.

And as the main disadvantage, the coefficient of friction was computed only at the point of wheel sliding.

5.2.5 Conclusions and recommendations

The approach on friction measurement in the railroad industry is briefly presented. After careful consideration of the targeted important aspects, the general conclusion is that none of the existing tribometers is suitable (or available) for the present research. Therefore, a new tribometer to be mounted on a rail vehicle must be designed and built.

5.3 Simple Sliding Sensor (SSS)

Because the wheel - rail environment is very rough, severe shocks are expected from the rail and transmitted through the wheel frame to the assembly body. In order to provide initial insight into the field measurements, a so-called "simple sliding sensor" was designed and built. Solutions for overcoming the high frequency vibrations coming from the rail to the sensors were found and applied to the tribometer design (section 5.4).

5.3.1 Concept

5.3.1.1 Measuring technique

Usually, the normal load and the friction force are measured in the direction they act. But in wheel - rail contacts it is impossible to measure the friction force in its direction. Therefore, preventing the torque generated by the "misalignment" between the friction force and the force transducer plane is also impossible. Such a moment of force is tolerated by a sensor only within specific ranges. Due to the fact that the wheel - rail contact conditions are rather rough and to avoid exceeding these limits, two force transducers are mounted between the two measuring plates.

A scheme is presented in Fig. 5.4.

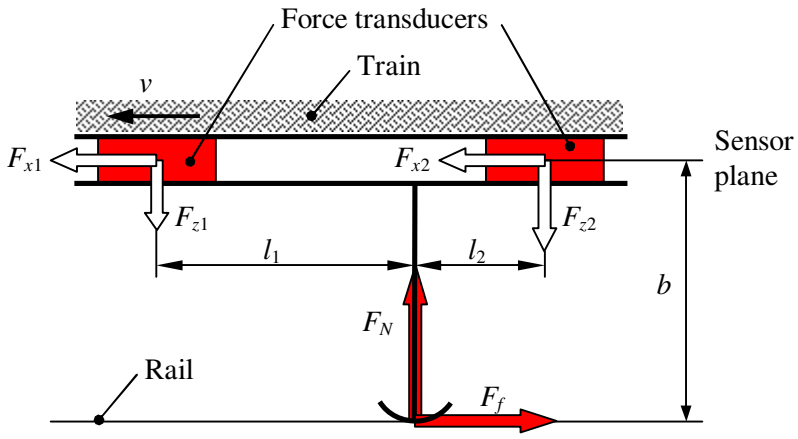

Fig. 5.4 Scheme of the force measurement technique.

The coefficient of friction is calculated from the measured values at the force transducers:

$$\mu = \frac{F_f}{F_N} = \frac{F_{x1} + F_{x2}}{F_{z1} + F_{z2}} \tag{5.1}$$

5.3.1.2 Contact probe

The geometry of the probe is a section of a disk (R_x) with a crowned rim (R_y) and is made of wheel material.

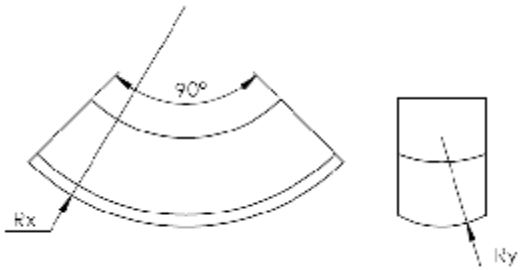

Fig. 5.5 Contact probe geometry.

5.3.1.3 Scheme

Based on the proposed measuring technique, a concept of the simple sliding sensor is designed.

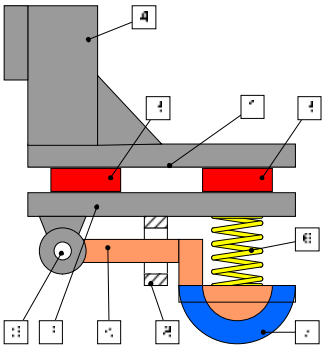

Fig. 5.6 Simple sliding sensor scheme.

In Fig. 5.6, two force transducers (3) able to measure the forces in the principal directions (X, Y, Z) are mounted between two plates (1 and 2). The upper plate (1) is welded to the bogie frame (4) which will be connected to the bogie. The lower plate is connected to the measuring arm (5) through the pivot (9). When the bogie frame is lowered, the spring (6) is loading the measuring arm inducing a contact load between the contact probe (7) and the rail, load measured by the two force transducers (3). Because these two force transducers are able to measure the forces in all principal directions, they also record the friction force.

5.3.1.4 Other requirements

After defining the main functions of the sensor, some other details must be set prior to making a final design. First of all, the movement of the train on the transversal plane to the measurement direction must be compensated. Since the main movement is the one in vertical direction (more than 50 mm), the construction in Fig. 5.6 has to be connected to a frame capable of following the relative irregularities between the train bogie and the top of the measured rail. A second issue is the high frequency vibrations expected from the rail to the two force transducers which are to be overcome by mounting a damping system between the bogie and the frame of the sensor.

5.3.2 Detailed construction

Considering all the above requirements, a final friction sensor was designed (Fig. 5.7). The bogie frame consists of two iron blocks which will be welded to the designated rolling stock.

According to the construction in Fig. 5.7, the normal load in the contact is given by the weight of the assembly from the linear guide to the contact probe. The spring has the role of absorbing vertical oscillations from the rail and therefore making the movement of the measuring unit smoother. If a higher normal load is desired then additional weight units can be mounted and subsequently the spring has to be changed so it can sustain the additional mass. The idea is to keep the swinging arm in balance without having a stiff connection between the measuring probe and the force transducers.

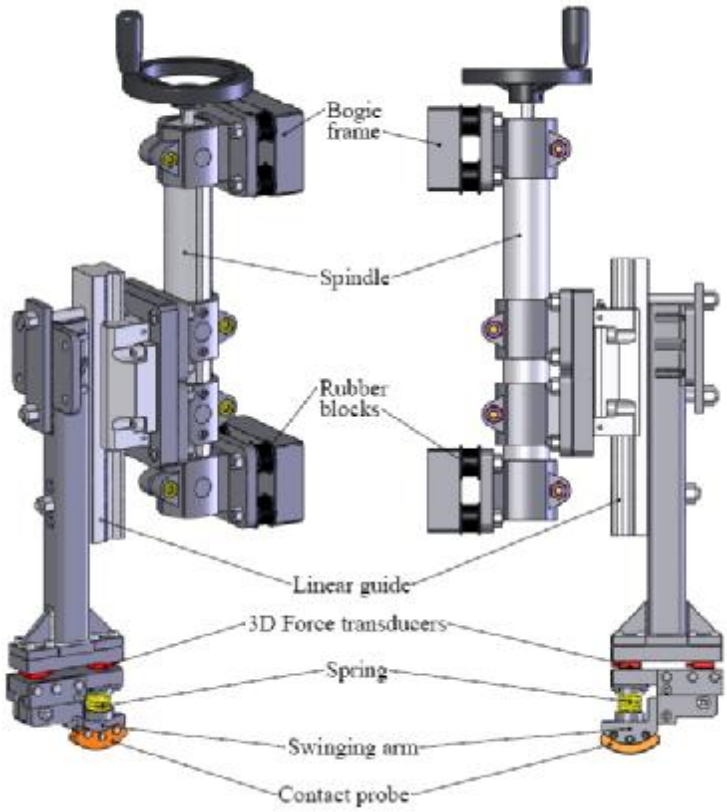

Fig. 5.7 Simple sliding sensor construction.

The constructed assembly was mounted in the front part of a Diesel locomotive (Fig. 5.8) and successfully put to use in the stabling yard of Zutphen, The Netherlands.

Fig. 5.8 Rolling stock and Sensor mounted.

The actual design permits the sensor to be lowered until the contact probe is in contact with the top of the rail by means of a manual spindle (Fig. 5.7). Automation still remains possible by mounting an electrical motor on top of the spindle and a controller. Because the purpose of the presented setup was just proving the detection of slippery tracks, manual control was enough.

A DGPS system (centimetre precision) allowed logging data about train velocity and position. All data from both sliding sensor and DGPS unit was logged in one file by using a Lab View script which also included a Graphical User Interface.

5.3.3 Experiment and results

The designated test track had a length of approximately 500 m. For investigating the changes in the friction level between the measuring probe and the top of the rail, several contaminants were applied on the track. The most representative third body used for contaminating the track was a thin grease called KajoBio [70]. The grease is used in the Dutch railroad for lubricating the contact between the flange of the train wheel and the gauge face of the rail (Fig. 5.9 left). The role of flange lubrication in curves is to lower the friction in the flange contact in order to reduce the squeal noise, track gauging forces and rolling resistance.

Fig. 5.9 Contaminants applied on the track: KajoBio (left) and Sandite (right).

The next applied contaminant over the previous one was the so-called Sandite [4], consisting of a gel containing sand and metal particles (Fig. 5.9 right). This product is also used in the Dutch rail network for improving friction wherever necessary.

The grease was applied over a length of approx. 30 m, then several measurements were performed over the contaminated area. At the first passage, an immediate effect was detected by the sensor and over the contaminated area a significant decrease of the coefficient of friction was recorded from 0.3 to 0.1 (Fig. 5.10 a).

Further, with each passage, the coefficient of friction slowly increased in the contaminated area and decreased in its vicinity because the grease was carried by the wheels of the rolling stock. Afterwards, Sandite was applied to the last 20 m of the previous area and after the first measurement an immediate increase of the coefficient of friction to approx. 0.3 was recorded (Fig. 5.10 b).

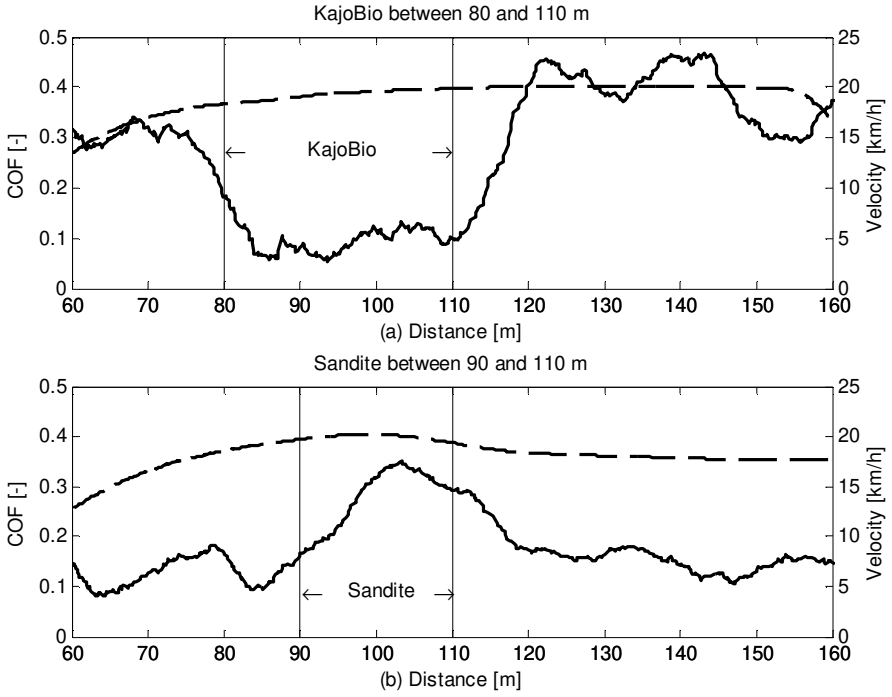

Fig. 5.10 Measurement results with the simple sliding sensor, KajoBio (top) and Sandite (Bottom).

5.3.4 Conclusions

The designed and constructed sensor is capable of detecting changes in friction level and even more, lasting effects of friction modifiers: low friction modifier (KajoBio) and high friction modifier (Sandite). It also detects changes in friction level after a number of passes. The low frequency oscillations of the rolling stock (50 mm and more) are compensated and the high frequency vibrations from the contact probe are damped, which are features leading to a smooth and continuous measurement up to the test velocities of 50 km/h.

5.4 Tribometer

After successfully testing the simple sliding sensor on a stabling yard track, the first step in the field measurements has been made. Knowledge has been gained about regulations and safety when operating within the rail infrastructure.

The next step is to design and use a more complex device capable of measuring traction curves at much higher velocities. The velocity is a very important feature because when carrying out extensive measurements over a rail network the measuring train has to be scheduled in between the normal traffic so a velocity of minimum 80 km/h is necessary. The need to measure traction curves is translated into having a small measuring wheel in contact with the rail whereby rotational speed is controlled by an electrical motor. The wheel - rail contact conditions will be reproduced by keeping the contact pressure the same.

5.4.1 Safety

Since the list is very large, the safety requirements are not all presented, but they all have been carefully considered and solutions for overcoming each one of them have been found.

Adding extra constructions to a rail vehicle of any kind requires special admittance procedures to be carried out. Moreover, since friction measurements imply having a loaded contact probe on the rail during vehicle movement, the process is even more complicated. A few of the major aspects that have to be considered are presented further. The entire construction must not exceed the envelope profile of the track (the area around the track where building is allowed) and the measuring wheel and the arm which will lower it on the rail must be constructed within this envelope profile. Finally, the main and most important safety requirement is as blunt as “no parts must fall off the train”.

5.4.2 Concept

Following the safety requirements the concept in Fig. 5.11 was chosen. The measuring principle is based on using four 3D force transducers sustaining a measuring plate on which all the components of the tribometer will be mounted. In this way, all the torques caused by any misalignment is compensated by each force transducer.

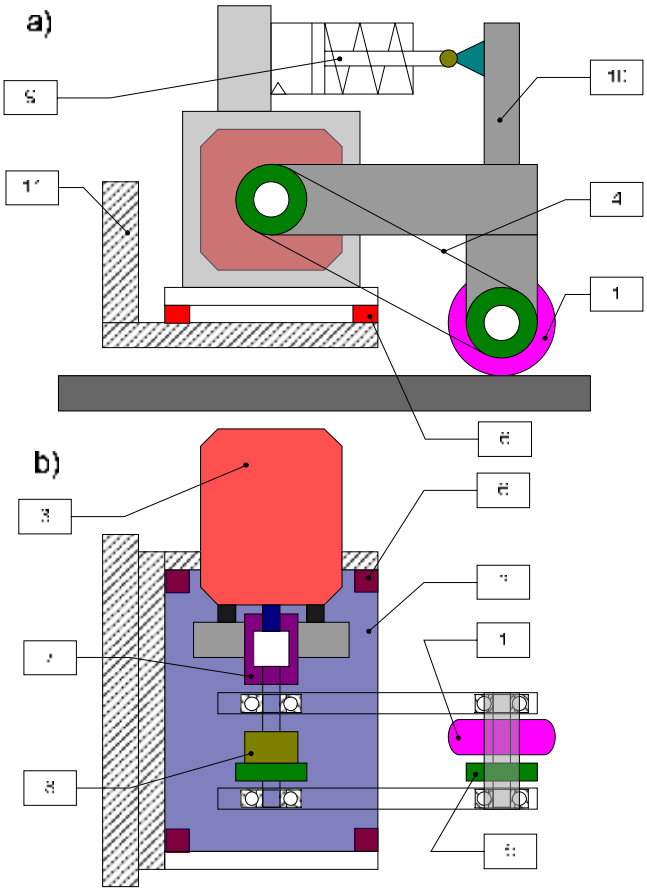

Fig. 5.11 Tribometer concept: a) side view and b) top view.

The measuring wheel (1) is in direct contact with the rail and it is connected to the main plate (2) by means of the wheel frame (10). The measuring wheel (1) and its frame (10) are the only components resting directly on the rail. This construction was chosen because it was the safest. On the main plate (2) are also mounted the motor (3) with its frame. The motor transmits the torque through the ROTEX coupling (7) to the torque limiter (8) and further to the measuring wheel through the chain transmission (4). The torque limiter is able to disconnect the power transmission from the motor to the wheel and vice versa in case of jamming or in case the friction force is exceeding the design limits.

The normal load in the contact is applied from inside the system, by means of an air cylinder (9). An air cylinder was chosen because of its good damping characteristics, taking into account that rough vibrations will be transmitted from the rail to the wheel and wheel frame. The friction between the measuring wheel

and the rail is measured without any interference from the inside components. Of course, there are some connections between the inside system and the outside one, consisting of wires powering the motor or transmitting the signals but these are difficult to avoid. For the presented application, a set of four matched 3D force transducers (6) will be used. Each of the force transducers is able to measure the forces between measuring plate (2) and bogie frame (11) in all three principal directions. Each force transducer has three outputs for the charge amplifier. Summing the signals in the same direction from all four sensors can be done by the use of a "summation" box.

The construction is robust and rigidly connected to the bogie, all the shocks are absorbed by the structural members of the construction and by the force transducers.

5.4.2.1 Measuring wheel geometry

For dimensioning all the components of the tribometer, extensive calculations have been done. Leaving aside the engineering part, the most important calculation from the research point of view is the measuring wheel contact geometry. The two radii of curvature have direct influence on the size of the entire construction when considering the main requirements. For example, keeping the mean contact pressure as in the real wheel - rail contact at a small wheel diameter will allow the mounting of a smaller air cylinder and an electric motor with lower torque and power requirements, therefore with smaller size (see Fig. 5.11). On the other hand, a small wheel diameter will require a higher rotational speed from the motor in order to keep the minimum measurement train velocity of 80 km/h.

Further, a prediction about how different wheel geometry will scale the output of the measurement was made by the usage of the friction model presented in chapter 3. A few simulations were run, by varying the geometry of the measuring wheel and subsequently adjusting the normal load in order to keep the mean contact pressure of 750 MPa. The inputs and calculated required normal load and torque are presented in Table 5.1 and the results in Fig. 5.12.

Table 5.1: Wheel geometry and consequences.

nr. crt.	R_{wx} [mm]	R_{wy} [mm]	F_N [N]	T [Nm] $f = 0.3$	$f = 0.4$	$f = 0.5$
1	475	∞	77500	11044	14725	18406
2	200	300	16500	990	1320	1650
3	200	100	7630	458	610	763
4	50	300	3736	56	75	93
5	50	100	2047	31	41	51
6	50	50	1183	18	24	30

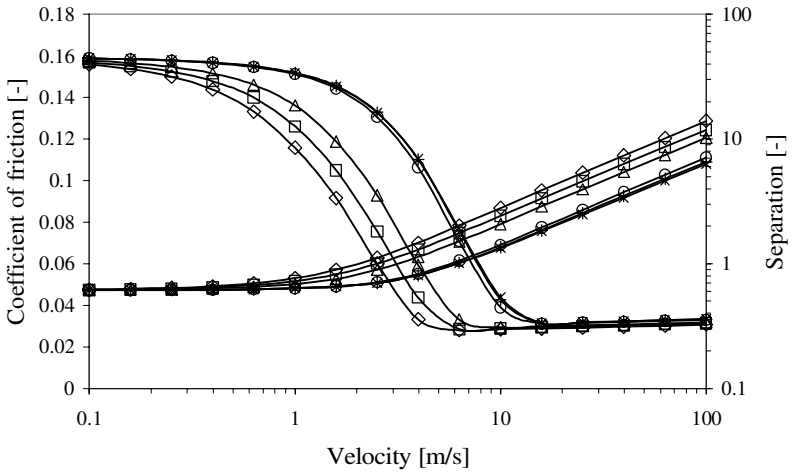

Fig. 5.12 Wheel geometry influence on the predicted Stribeck curve and separation (h_c/σ). $R_x \times R_y$ [mm×mm]: ◊475×INF, □200×300, Δ200×100, ○50×300, +50×100 and ×50×50; see Table 5.1.

The point of this discussion is to determine how much the scale of the tribometer measuring wheel is influencing the measurement, compared to the full scale predictions (curve 1 in Table 5.1 and Fig. 5.12). The second and third curves are closest to the full-scale estimations, but the very high required torque gives no alternative than to move to the next cases. Curves 4, 5 and 6, being very close to each other, will be treated as giving the same result; the factor is determining the required torque and normal load. From this point of view, the last curve, representing the prediction of the Stribeck curve for wheel geometry of 100 mm in diameter and 50 mm radius in the profile, gives the lowest expectations from the motor and the air cylinder.

5.4.3 Detailed construction

In parallel with the friction measurements from the rail tribometer, spectral measurements from the top of the rail were also considered to give potentially valuable correlation with friction. Such correlation would give a major step into slippery track detection by the use of a non-contacting probe. A spectrometer concept was proposed and designed by the Laboratory of Plant Physiology [71] of Wageningen University.

The final product i.e. TriSpec (Tribometer - Spectrometer) was fully engineered by Iris Vision [72], which combined the two concepts into a final design and further manufactured it and developed the software to control the unit when mounted on a special measuring wagon.

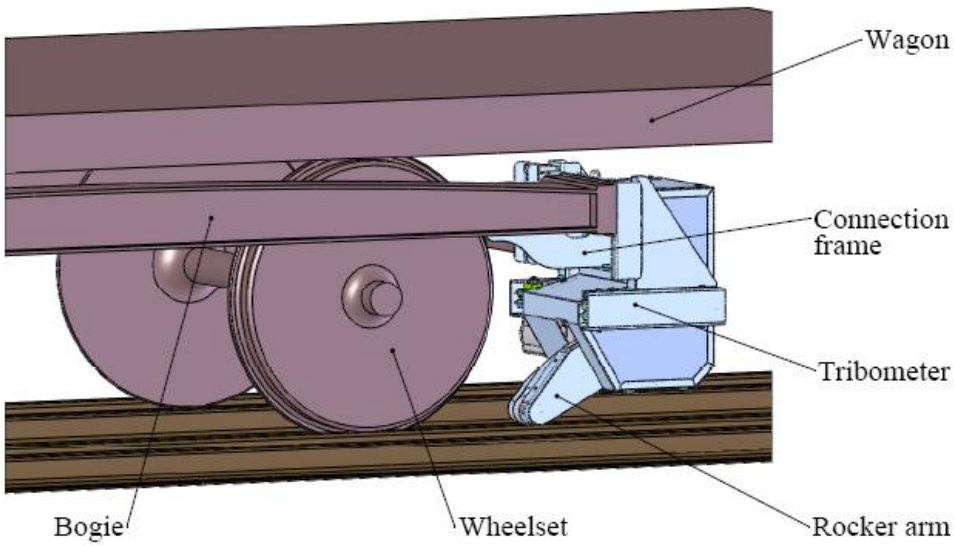

Fig. 5.13 Tribometer mounted on the rail vehicle bogie.

In the design calculations, the following aspects related to safety were considered. The mass resting on the rail has to be as low as possible so eventual shocks from the rail will not generate high inertial forces. The tribometer will be mounted on a bogie by clamping it as close as possible to one of the wheels (Fig. 5.13). In this way the relative movement between the measuring wheel and the rail profile will be minimized.

Going further with the construction of the tribometer (Fig. 5.14), the default position of the measuring wheel will be “UP”, this position is maintained by a retracting spring. For lowering the rocker arm, the air cylinder must first overcome the spring retracting force. A safety pin was used in the joint between the air cylinder and the rocker arm so if some severe shock is encountered by any obstacle from the rail, this will shear and subsequently the rocker arm will be immediately lifted by the retracting spring.

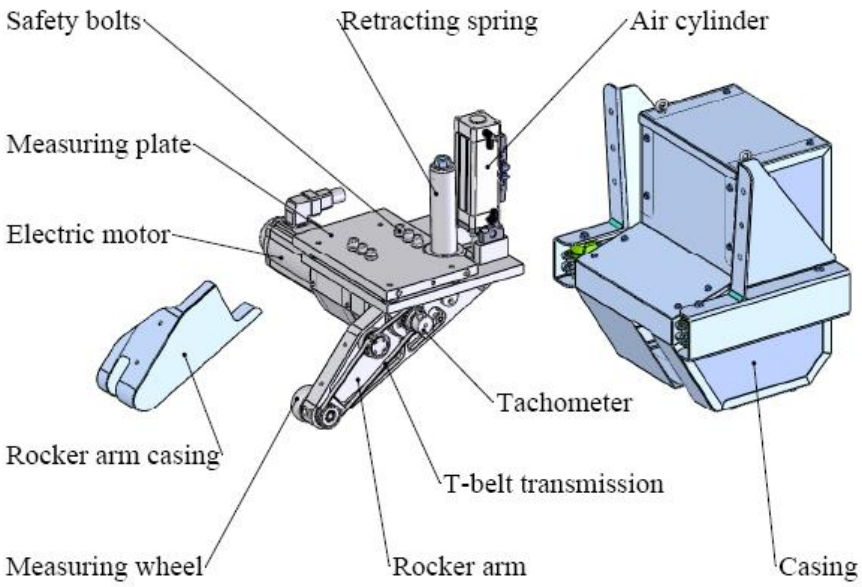

Fig. 5.14 Tribometer construction.

The electric motor will rotate the wheel through a T-belt transmission and the rotational speed of the measuring wheel will be measured by a tachometer. All the components are mounted on the measuring plate (Fig. 5.15).

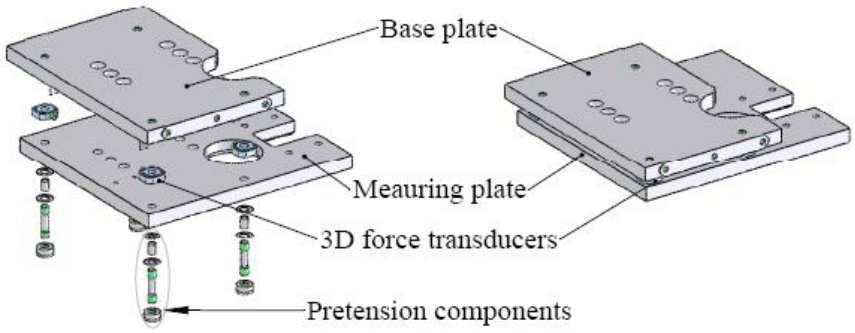

Fig. 5.15 Measuring plate.

Fig. 5.15 shows the configuration of the measuring plate. The base (upper) plate is to be connected to the casing of the tribometer. The casing is connected to the bogie by using four rubber dampers. On the measuring (lower) plate are mounted all the components of the tribometer (electric motor, transmission, tachometer, rocker arm, measuring wheel, air cylinder and retracting spring). The two plates are

connected through pretension components which hold in place the set of four matched 3D force transducers. As an extra precaution, six safety bolts are screwed and tightened into the measuring plate without having direct contact but passing through the upper plate. So, in case the pretension elements are failing, the two plates will still be connected.

The presented construction was mounted on a dedicated measuring vehicle pulled by a locomotive. For security reasons, an extra couch was mounted in between the measuring couch and the locomotive (Fig. 5.16).

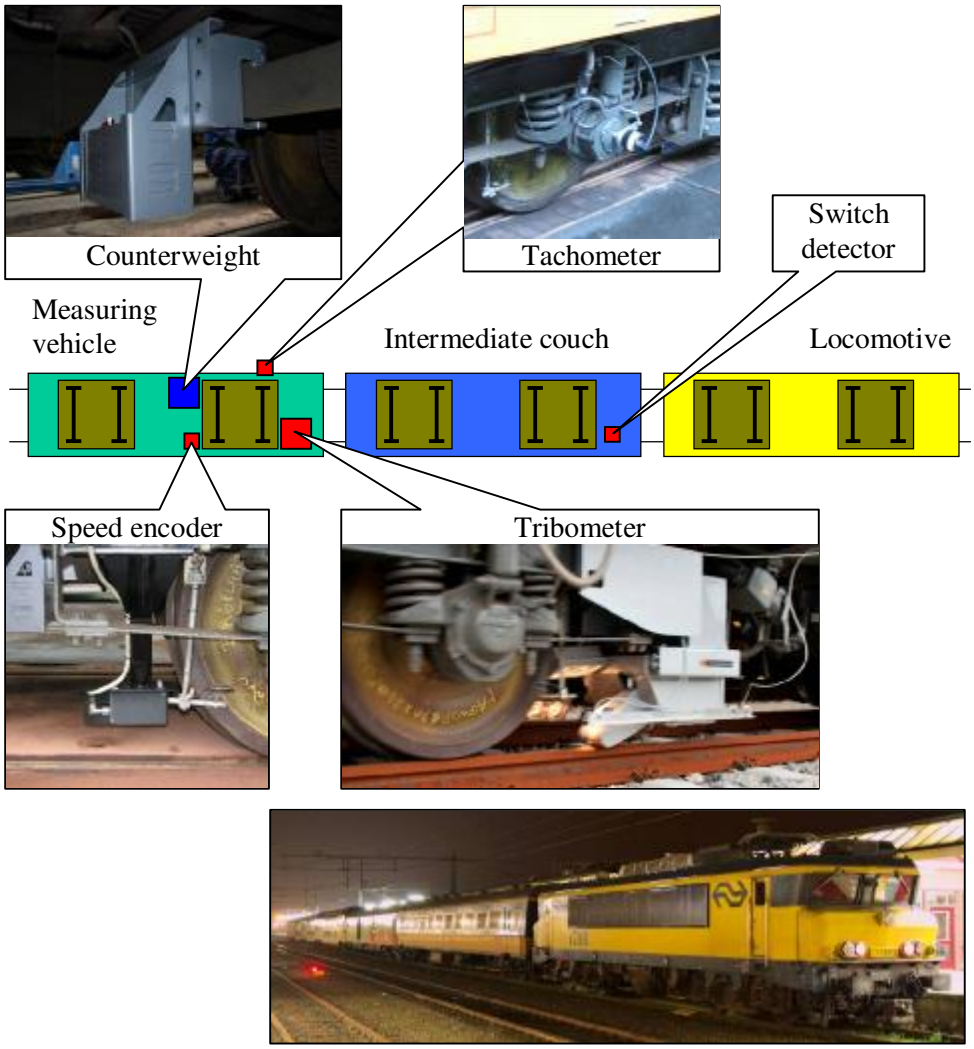

Fig. 5.16 Tribometer on train.

Another important feature is the switch detector. This is, in fact, a proximity sensor which is mounted on the couch ahead of the tribometer pointing at 100 mm inside the track. When a switch is encountered, the sensor triggers and then immediately the rocker arm will be lifted.

5.4.4 Tribometer measurement description

Prior to interpreting the data reading from the TriSpec, the run description has to be detailed. The TriSpec is entirely controlled from a PC terminal (Fig. 5.17) and all its functions necessary to perform a measurement are remote controlled. Safety, being the main constraint on the robustness of the design, also plays an important role in the automation of the measurement, for example, the previously mentioned switch detector (Fig. 5.16).

When the measuring speed is reached, the charge amplifier must be reset and the START button is pressed. The data acquisition starts automatically. The motor will rotate the measuring wheel until its peripheral speed is equal to the speed of the train. At this point, the pure rolling situation should be present. The pneumatic cylinder will lower the rocker arm and press the measuring wheel against the rail with the desired force. At this point, the four-step measuring procedure (Fig. 5.18) starts.

Control terminal

Motor controller

Tribometer controller and data logger

Fig. 5.17 Tribometer control equipment.

Step 1: The motor will increase the speed of the wheel with a difference in velocity between its peripheral velocity and train velocity until the given amplitude, Δv, in km/h is reached within a given time interval, t, in sec.

Step 2: When this amplitude, Δv, is reached the motor decreases the speed of the wheel until the starting value (the one according to pure rolling situation) is reached, within the same time interval, t.

Steps 3 and 4: Next, two sequences are identical to the previous two steps but the motor is braking the measuring wheel within the same amplitude, Δv, over the same time, t, as in the previous two steps.

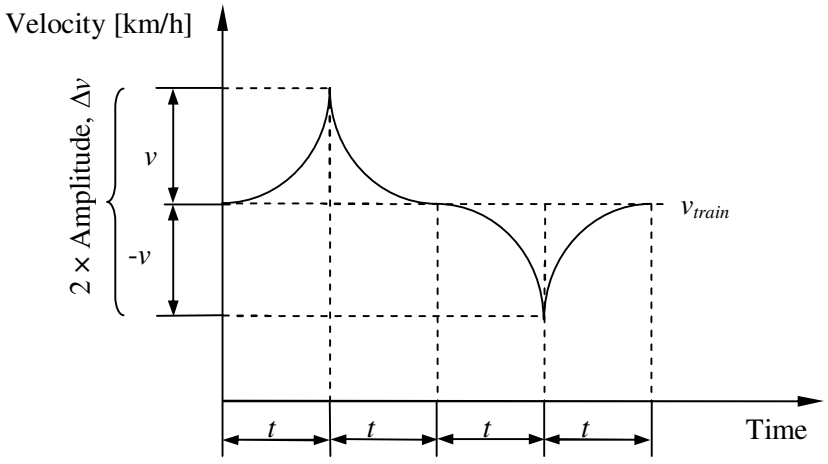

Fig. 5.18 Acceleration and braking scheme, traction curve measurement.

This four-step cycle will continue until the STOP button is pressed. When the STOP button is pressed, first the last cycle will be completed, the pressure to the air cylinder will be cut so the rocker arm will be lifted by the retracting spring. The motor power is also shut down and the data acquisition stops.

For easier post-processing, the measurements had to be performed using a time interval, t, set to a constant value for all measurements. After testing different values, it seemed that a value of 1.5 seconds would be appropriate for any train speed, giving enough time for the wheel to accelerate and brake. Therefore, each cycle ($4 \times t$ for a full traction curve) took 6 seconds to complete.

5.4.4.1 Measurement schedule

The autumn measurement campaign was scheduled over a period of three months in three different locations in the Dutch rail network: Zeeuwselijn (between Roosendaal and Vlissingen), Hoekselijn (between Rotterdam and Hoek van Holland) and Utrecht – Arnhem – Zwolle triangle (Fig. 5.19).

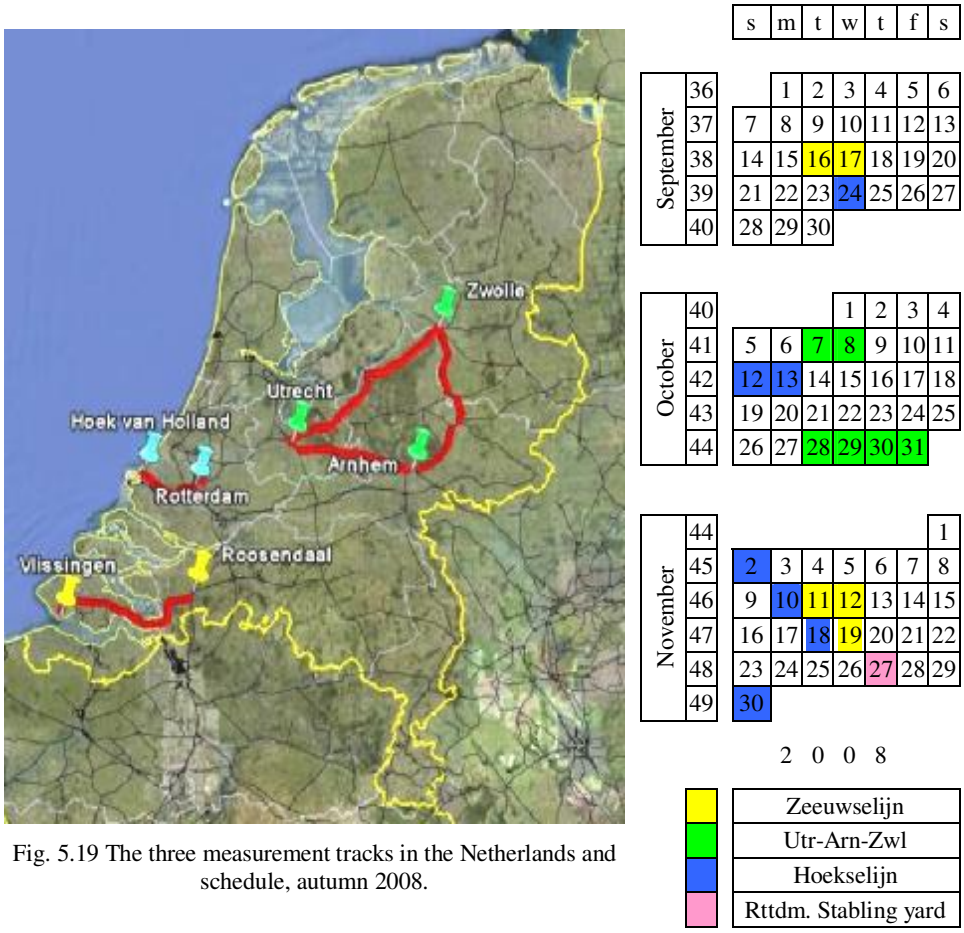

Fig. 5.19 The three measurement tracks in the Netherlands and schedule, autumn 2008.

The Utrecht - Arnhem - Zwolle track was measured once per night, Hoekselijn three to four times per night and Zeeuwselijn two times per night, depending on the track length and available time.

5.4.5 Raw data logging

The TriSpec was designed to perform a complete traction curve up to a maximum slip of 20% at a nominal train velocity of 80 km/h with the possibility to measure braking traction curves at 108 km/h. At such high velocities the data acquisition process is very noisy due to the shocks between the measuring wheel and the top of the rail. The measuring wheel has a diameter of 100 mm, meaning that to achieve pure rolling at a train velocity of 80 km/h its rotational speed had to be approx. 4000 rpm. The maximum traction slip is reached at peripheral velocity of the

measuring wheel of 108 km/h, i.e. approx. 6000 rpm. These specifications are meant to underline the most severe conditions in which the friction measurements were acquired. Some noise in the output data was expected, even with the installed damping system. In the end, the construction of the tribometer was proven to be robust enough and the output signal was optimum.

All TriSpec data was stored directly onto mobile hard drives, by the end of the measuring campaign weighting 700 GB. The content of the AVI and ASCII log files are given in Table 5.2.

Table 5.2: Content of log files.

File	Content
1\000.avi	Video camera, MJPG video stream, 640 × 511
2\000.avi	Visible light spectral camera (VIS), 16 bit AVI files, 476 × 350
3\000.avi	Infra red spectral camera (NIR), 16 bit AVI files, 320 × 256
1.log	UTC timestamp (TS) and frame number (FN) of the video camera
2.log	UTC and FN of the VIS camera
3.log	UTC and FN of the NIR camera
adcs.log	UTC, F_x, F_y and F_z (voltages from the force sensors)
counters.log	UTC, measuring wheel encoder pulses and cor sensor pulses
tacho.log	UTC, train encoder pulses and travelled distance in [m]
wissel.gpslog	UTC, latitude and longitude in RD coordinates. RD = "Rijksdriehoeksmeting" from the Dutch Land Register

5.4.6 Processed outputs

For processing all the data, a Matlab [73] script was written in such way it could automatically search through the log files and extract the measurements so they can be used in a statistical study.

All separate files were opened simultaneously and synchronized using the UTC time stamp of the GPS. Both friction and speed encoder data had to be smoothened. This was done by using the Savitzky - Golay filter [74], which is implemented in Matlab. The GPS latitude and longitude from the Dutch RD coordinate system had to be converted to the World Geodetic System (WGS).

The data post-processing took approximately 200 hours and filtered approximately 800 km of valid measurements.

5.4.6.1 Velocity plot

First outputs (Fig. 5.20) are the velocities involved in calculating the slip: the train velocity from the wheelset encoder (5000 pulses/rot) and the measuring wheel peripheral velocity from its encoder (1024 pulses/rot). As an extra check for the velocity of the train, there is a contactless velocity encoder (1800 pulses/metre).

The measured coefficient of friction is plotted on the right Y axis. On the X axis is the distance calculated from the GPS data, from the starting point of the measurement.

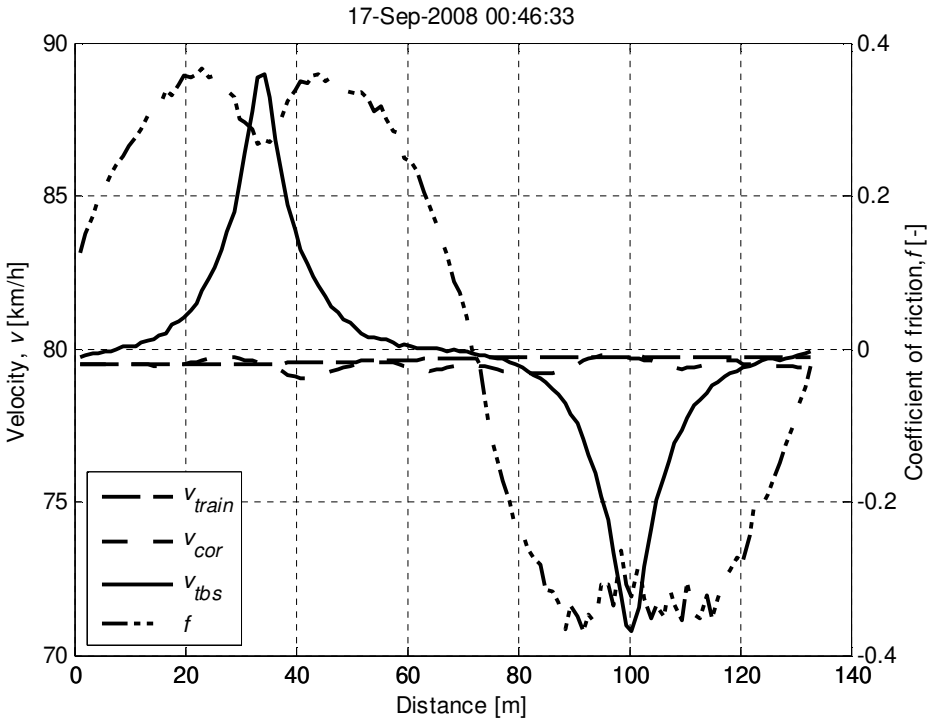

Fig. 5.20 Measured velocities of the train (v_{train} from the tachometer and v_{cor} from the contactless speed encoder, see Fig. 5.13) and measuring wheel, v_{tbs}, (left axis) and coefficient of friction, f, (right axis) during a cycle.

In Fig. 5.20, the train velocity is approximately 80 km/h and the measuring wheel is changing the velocity between 70 and 90 km/h. starting from 80 km/h, increasing the slip from zero up to a positive value (traction) and then decreasing it to a negative slip (braking). As a check, the coefficient of friction is zero when the two velocities are equal.

5.4.6.2 Traction curve

Based on the velocities, the slip is calculated and the traction curve can be plotted (Fig. 5.21). This is the main output of the friction measurement. The traction curve gives an indication if the layer causes low adhesion. The example in Fig. 5.21, however, is a high friction case.

The traction curve is saved as a picture and in its legend some other information is plotted: date and hour at which the measurement started, latitude and longitude at the starting point, distance over which the traction curve was measured in metres, train velocity in km/h at the starting point, start and stop frames into the three video files mentioned in Table 5.2, the value of the coefficient of friction calculated at half of the maximum slip (in this case 6%) on the traction side of the curve and finally, the time in seconds over which the traction curve was measured.

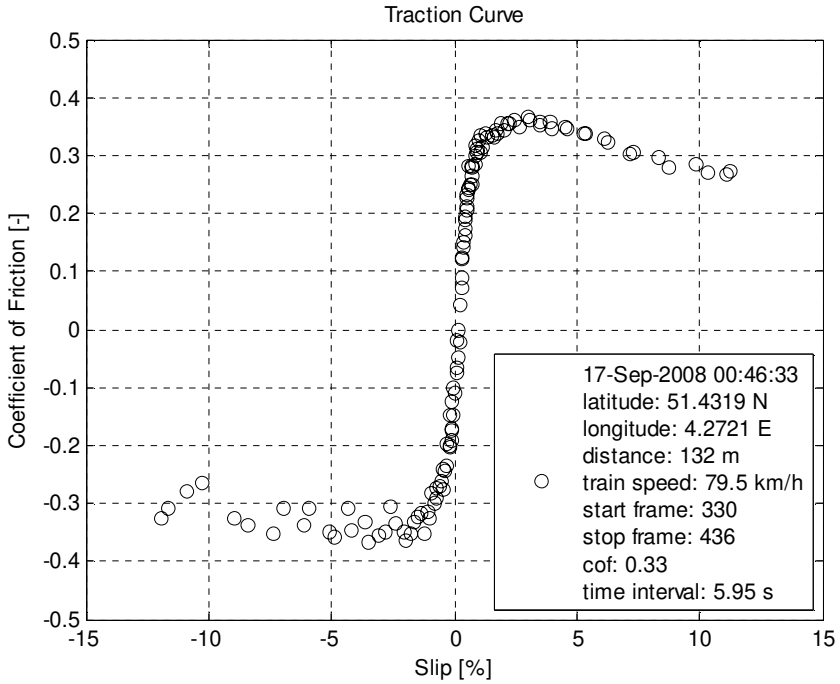

Fig. 5.21 Example of a measured traction curve.

5.4.6.3 Classifier log

Some of the information in Fig. 5.21 is also saved as a tab separated ASCII file which contains the time at which the measurement started, start and stop frames in the video files and the coefficient of friction calculated as previously specified.

5.4.6.4 GPS location

A next output is in fact a file with “kml” extension, an extension which can be opened with the Google Earth software. For example, the traction curve from Fig. 5.21 was measured on Zeeuwselijn, between Roosendaal and Vlissingen (Fig. 5.22).

Fig. 5.22 GPS location of the measured traction curve.

5.4.6.5 Video

The output log file (section 5.4.6.3) contains the start and stop frames in the spectral video files, this information was also used to split the normal video file into chunks according to each traction curve, while the corresponding frame number is also merged into the video. An extracted frame is shown in Fig. 5.23. These videos can be inspected later when the friction data shows abnormal readings.

Fig. 5.23 Frame extracted from the video camera.

5.4.6.6 Traction curve log

It is also important to have the filtered data in a two column matrix saved as a tab ASCII file containing, of course, the Slip and the coefficient of friction. These log files are to be used further for the parametric and statistical study.

5.4.6.7 Conclusions

Because of the huge amount of data (700 GB or 175 DVDs), the manual processing was impossible so a complex code had to be written in Matlab to automate the process. The code needed approximately 200 hours to process all the data. The main result was a number of 8000 sets of outputs as described in section 5.4.6. Out of these, a number of 6172 measurement sets were chosen as valid by visually inspecting each result. If considering that all measurements were performed at 80 km/h and a cycle (Fig. 5.18) took 6 seconds, this means that approximately 800 km of track were measured.

5.4.7 Statistical study

After reading and processing the raw data, a statistical study was made in order to compress the huge amount of information into readable informative plots.

5.4.7.1 First classification

The total 6172 measurements were sorted by using the value of the coefficient of friction recorded at half of the maximum slip on the traction side of the curve. These values were split with a step size of 0.01 into 50 classes and their probability density is shown in Fig. 5.24.

Casting a glance at Fig. 5.24, one may see that approximately 80% of the values are between 0.05 and 0.2. Considering that the measurements were carried out over the entire autumn in three different locations, from a statistical point of view, the range (0.05 - 0.2) indicates the friction level for the Dutch rail network during autumn. Future coefficients of friction considered in calculations should be verified with this range.

Narrowing the classification into three main groups such as low, medium and high coefficient of friction gave more insight into the severity of the problem. The three division classes are shown in Table 5.3.

Table 5.3: Classification of the coefficients of friction (intervals also shown in Fig. 5.24).

Friction	COF	No. of measurements	Percentage
Low	< 0.07	1351	22
Medium	0.07 ... 0.15	2702	44
High	> 0.15	2111	34

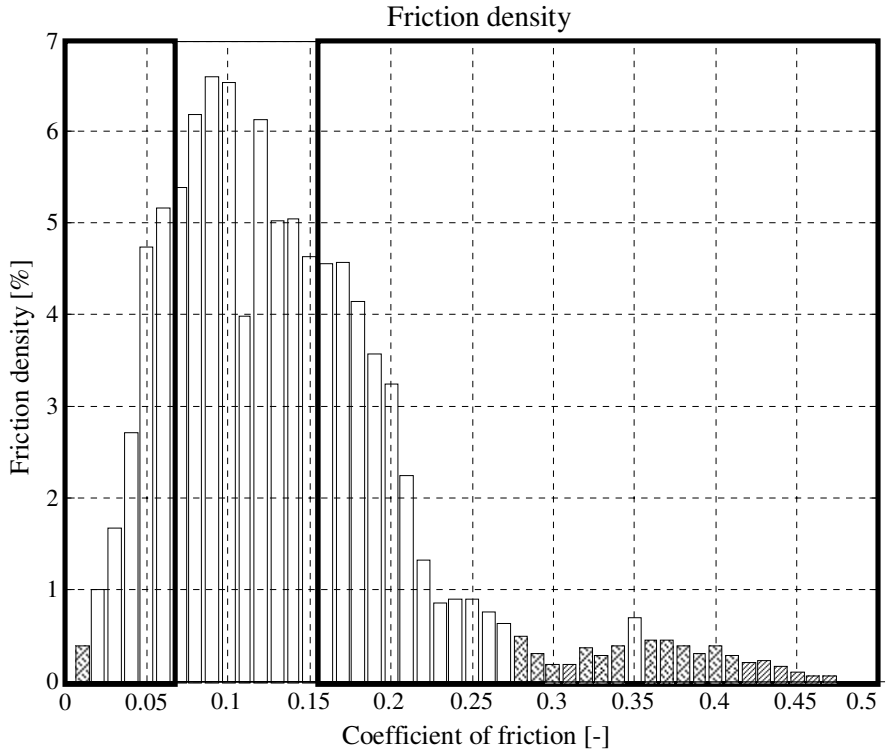

Fig. 5.24 The friction probability density.

The low coefficient of friction value of 0.07 was calculated from a safety point of view, when a train has to brake from 140 km/h until a complete stop within a standardized interval. The high coefficient of friction value is calculated from the requirements of the motor, so the train can reach the maximum velocity with full power of the motor. The coefficient of friction value necessary for accomplishing this is 0.15. The Dutch operator (NSR) uses this last value to make the timetables. The spectra correlation was also made based on the classification given in Table 5.3.

Further, the percentage of each of the three classes is plotted for each measured location in Fig. 5.25, as explained and discussed below. On the X axis is the day when the measurement was taken and on the Y axis is the percentage of the class. The first figure of Fig. 5.25 represents the high friction class (> 0.15) and the last one the low friction class (< 0.07). The first three measuring nights were made in September on Zeeuwselijn and Hoekselijn (Fig. 5.19) and they show no friction problems, almost 100% of the values belong to the high friction class. Following the schedule in Fig. 5.19, the next two measuring nights were on the Utrecht -

Arnhem - Zwolle track. In Fig. 5.25, the first set of high friction values are from the 6th of October, just before midnight. At that time the measured coefficient of friction was higher than 0.15. After midnight, classifying all the measurements, showed a slight decrease on average and further the next night on the same locations, lower coefficient of friction data was recorded. The entire October and November showed a lower friction level than September and most of the values of the coefficient of friction were lower than 0.15.

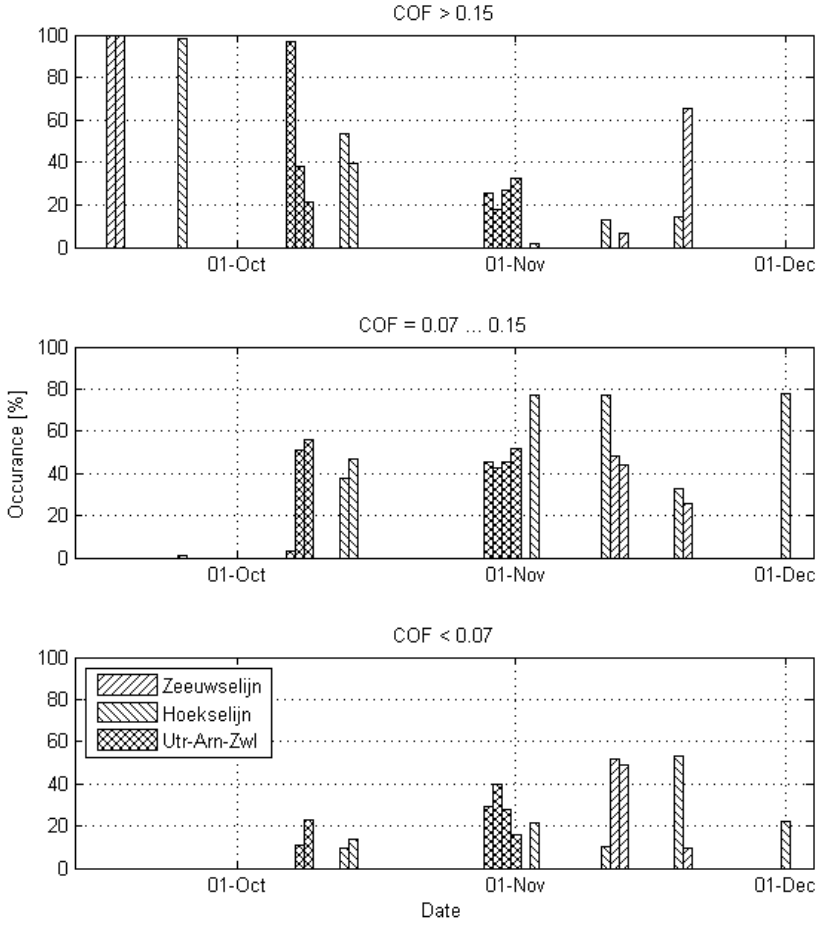

Fig. 5.25 Probability of the three friction classes.

Further correlation with weather data for the measured locations and hours should be done in order to determine if any weather-related factor contributed to the friction level.

5.4.7.2 Parametric interpretation

Besides the first rough classification in low, medium and high adhesion, the measurements provide the traction curve (Fig. 5.21), which gives information about the rheological properties of the interfacial layer, when running over tracks with low friction. The traction curve as presented in Fig. 5.21 has no use in this sense. Therefore a parameterization is done by fitting a logarithm normal function to the data points.

$$f = a^{\#} \cdot \exp\left\{ -\frac{\left[\ln(S) - b^{\#}\right]^2}{c^{\#}} \right\} \tag{5.2}$$

Where, f is the coefficient of friction, S is the slip and $a^{\#}$, $b^{\#}$ and $c^{\#}$ are the fit parameters.

The fit was made by finding the minimum of unconstrained multivariable function using the derivative-free method (the "fminsearch" built in Matlab function). An example of such fit is shown in Fig. 5.26.

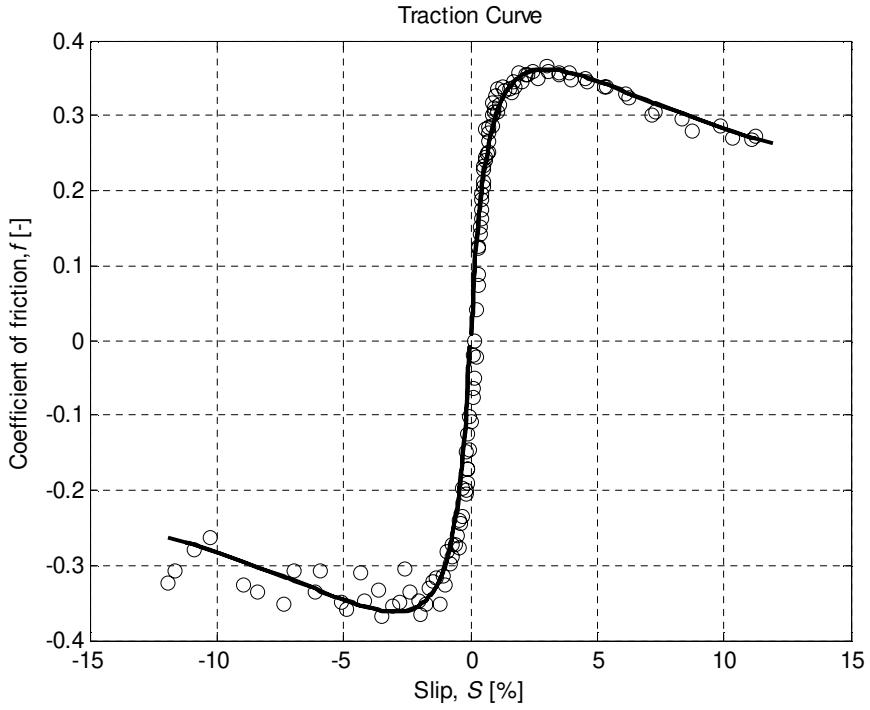

Fig. 5.26 Fit of Eq. 5.2 after the measurement in Fig. 5.21.

The fitting process was again automated by writing a Matlab script. Describing the

traction curves parametrically opened the possibility of plotting several important points for each curve. The key points on a traction curve are shown in Fig. 5.27 and described further.

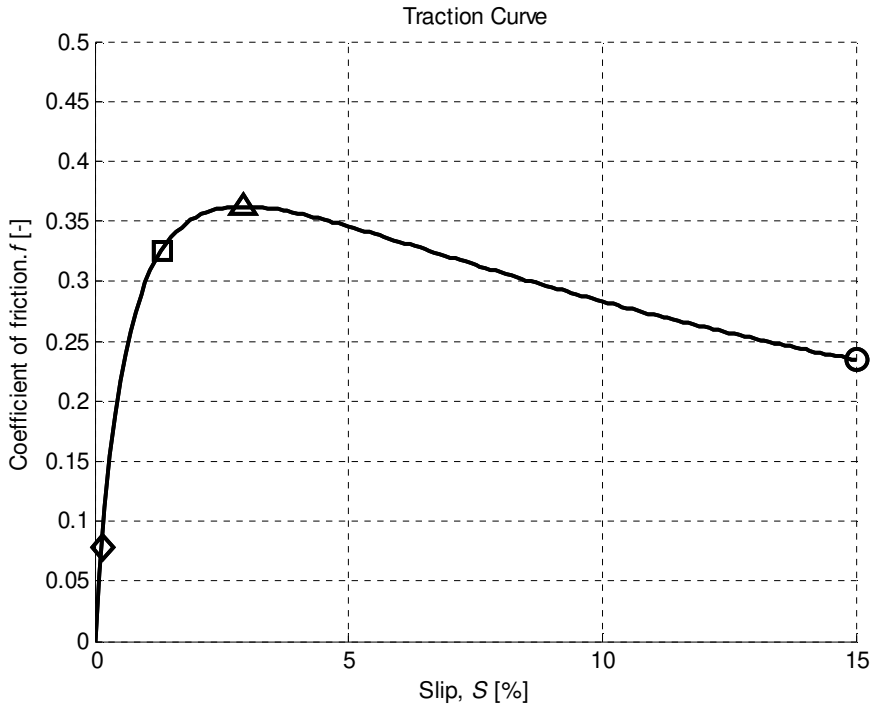

Fig. 5.27 Plot of the fit function and important points: ◊ tangent at the initial slope, Δ maximum coefficient of friction (COF max), □ 0.9×COF max, ○ COF at 15% slip.

Initial slope

First is the tangential point at the initial slope (the first derivative in that point will give the tangent of the slope around zero slip). This value is influenced by the viscosity of the contamination if such contamination exists and the functioning regime can be considered elastohydrodynamic (EHL).

Maximum coefficient of friction

Finally, an answer to the question "at what slip value does the coefficient of friction reach its maximum?". Of equal interest is also the slip value at which the coefficient of friction is slightly lower than the maximum value i.e. $0.9 \times f_{max}$. It can happen that the slip at this value is much smaller than the slip at maximum friction.

Decreasing slope

The temperature effects are visualized onto the traction curve in its last part. If the slope at maximum slip is negative it means the temperature in contact influences the frictional behaviour of the interfacial layer. The check is a decreasing slope at high slip, or not, and is made by comparing the value of the coefficient of friction at maximum slip with the maximum coefficient of friction. Of course, the second derivative gives information about the slope over the entire slip range.

5.4.7.3 Correlation studies

Identifying the classes of all traction curves is done by using a technique presented below. The first classification shown in Table 5.3 remains as the main classifier since it also was used in the correlation studies with the spectra of the surface layer. The next step is, for each of these classes, to identify a distribution of the initial slopes and finally a distribution of the slopes at high slip values.

Because the initial classification was made based on the coefficient of friction measured at half of the maximum slip, the actual maximum on the traction curve can be slightly different, depending on the slopes along the curve.

High friction (first three measuring nights)

Observing that in the first three measuring nights only high friction data was recorded (Fig. 5.25), a subclass is proposed corresponding only to these three nights since the highest friction is expected. Because the same study will be made for the rest of the classes, this one will be explained in greater depth.

Of primary interest is the location of the maximum coefficient of friction on the traction curve. Fig. 5.28 plots significant statistical data concerning the maximum recorded values of the coefficient of friction and the related slip values.

Fig. 5.28 (a) plots the maximum values of the coefficient of friction as a function of slip (Δ symbol in Fig. 5.27). As an observation, if the maximum COF happens at a slip value lower than 15 %, the traction curve presents a decreasing slope on its right-hand side.

The kernel density estimation using automatic bandwidth selection method and the Matlab implementation codes for 1D (kde) and 2D (kde2d) datasets [75] are used for plotting the probability density of both related COFs and slip. In Fig. 5.28 (b) and (d) are plotted the 2D probability densities of both related COFs and slip. The linear probability density using the same method [75] is used for a better identification of the maximum encountered values (Fig. 5.29 a).

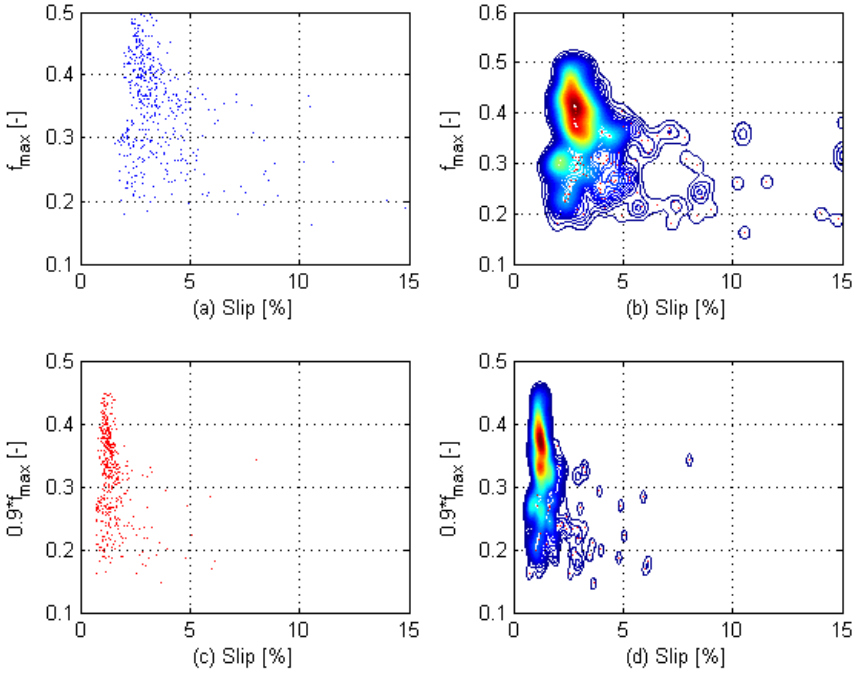

Fig. 5.28 Statistical data for the first subclass of high friction data: (a) maximum COF as a function of slip and (b) 2D probability density of the max COF and slip; (c) and (d) same for 0.9 of the max COF.

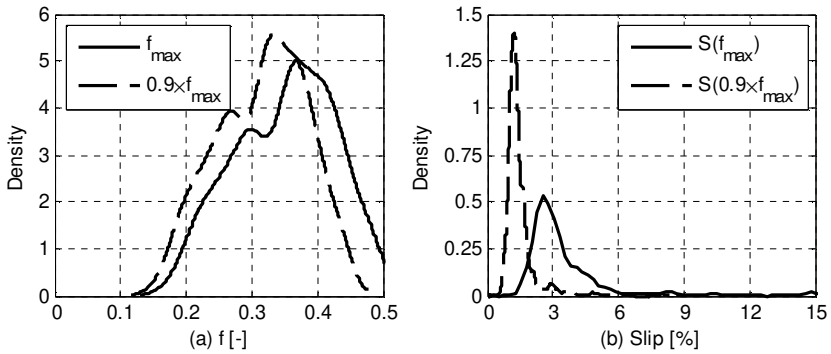

Fig. 5.29 Probability density of maximum COF (continuous line) and 0.9×maximum COF (dashed line) against related slip.

If the probability density of the coefficient of friction is plotted for slip values between 0 and 15% (f_{max} is the continuous line and $0.9 \times f_{max}$ is the dashed line), Fig. 5.29 is obtained. One can observe that most of the maximum COF values happen at

a slip value lower than approximately 6%. Even more, for a parametric study, the 2.75% value will be noted as the mean optimum slip value for reaching the absolute maximum value of COF. But what exactly does the maximum value of the COF mean? The answer is found in the plot of the probability density of the maximum COF (Fig. 5.29 (a), continuous line). The max COF values within the high friction class lie between 0.15 and 0.5 with the highest probability at 0.37 and a secondary peak at 0.3. Note that both peaks of the maximum COF happen at the same peak of slip value.

Trying to restrain the slip interval for the maximum COF, the same plots as presented above are made for the slightly smaller value of the maximum COF i.e. $0.9 \times f_{max}$. Fig. 5.28 shows that for slightly lower values of the maximum COF with a peak at approximately 0.33 and secondary peak at 0.26 (Fig. 5.29 a), the related slip decreases significantly and further almost 100% of the values are lower than 3% slip with a peak at 1.2 % (Fig. 5.29 b). In this case, the correlation between the 2D (Fig. 5.28) and the linear (Fig. 5.29) probability estimation is valid since there are two groups of data clearly separated.

It can be concluded that for the high friction class, the optimum slip would be 1.2% for reaching a coefficient of friction of 0.33. Note that any slip exceeding this optimum will not result in a friction level lower than 0.15, which is the value on which the timetable is made and that the braking distance is guaranteed at the same slip values.

Of equal interest are the slopes around zero slip value. A trial for correlating the initial slopes with the 0.9 of the maximum COF[1] is made below (Fig. 5.30).

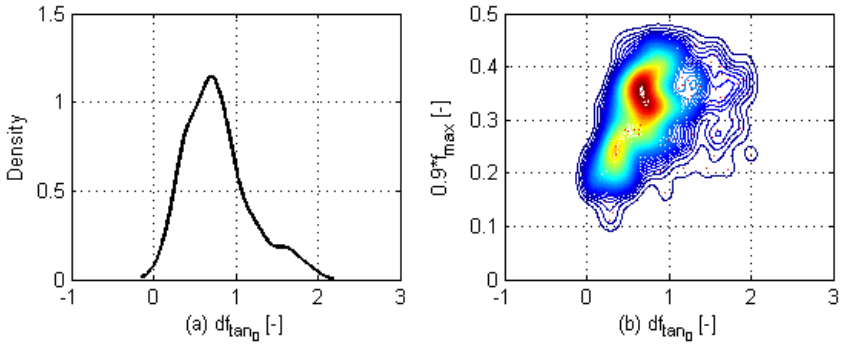

Fig. 5.30 Slopes at rolling: (a) probability density of all slope values and (b) correlation between $0.9 \times f_{max}$ and slope.

[1] Since it was shown before that the COF equal with $0.9 \times f_{max}$ is more significant when correlated with the according slip value, this quantity will be used for this correlation.

Plotting the probability density for the slopes around zero slip, (Fig. 5.30 a), shows that the initial slope varies from approximately 0.3 to 1.7, with a peak for the slope at 0.7. However, since a correlation with the maximum slip is of interest, the 2D density estimation between the two is also shown (Fig. 5.30 b). It is shown here that indeed the registered peak of 0.7 corresponds to the COF value of 0.33. A smaller secondary summit is recorded for a slope of 0.3 corresponding to a COF of 0.26. Two classes are identified up to this point by correlating the initial slopes (0.7 and 0.3) with the two maximum values of the COF (0.33 and 0.26) at the same slip (1.2%).

Continuing the study on the last part of the traction curve, of high interest are the values of the COF at high slip values i.e. 15% and the slope at that point. If assuming that the maximum COF has one peak in the probability density function (0.37 in Fig. 5.29 a) then higher slope values will automatically correspond to lower COF values. This will be explained further. Fig. 5.31 plots the probability densities of the coefficient of friction at a slip of 15%, $f_{15\%}$ (a) and related slope (b). As can be seen, most of the slopes have negative values and two peaks are noted at -0.0065 and -0.008. For the COF at 15% slip, the probability density plot doesn't say much with respect to correlated data, it only shows a concentration of values around 0.25.

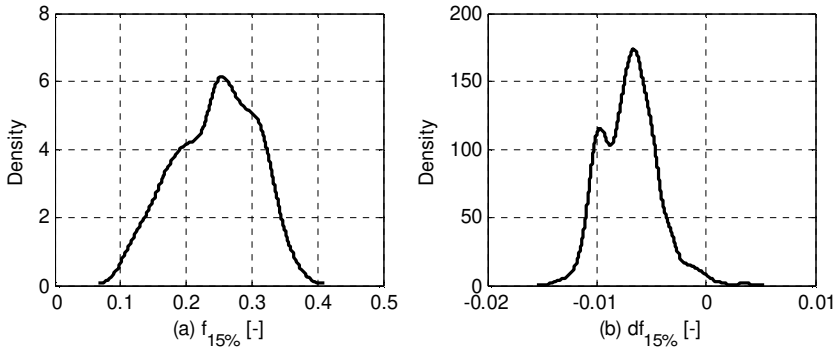

Fig. 5.31 Probability density of the coefficient of friction (a) and related slope (b) at a slip of 15%.

For a good correlation, the 2D density estimation functions are plotted between the values of COF at 15% slip against the related slopes (Fig. 5.32 a) and the same against the maximum COF values (Fig. 5.32 b). Fig. 5.32 b shows two summits at the same maximum COF values in the first part of the classification i.e. 0.37 and 0.3 with the corresponding values of the COF at 15% slip of 0.25 and 0.17. Even more, these last values are at the same coordinates of the summits in Fig. 5.32 a, where the slopes are -0.008 and -0.0065 accordingly.

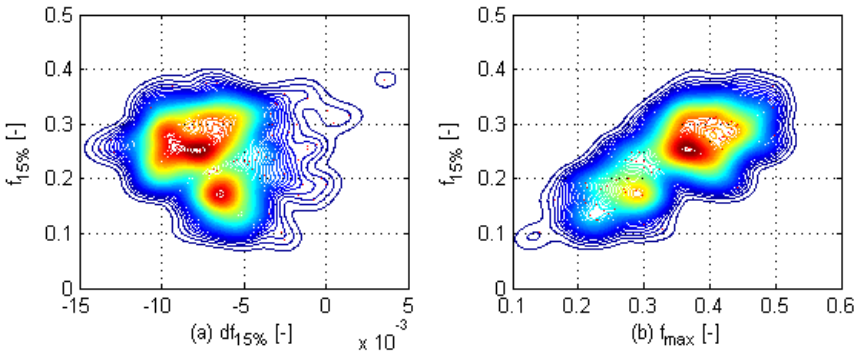

Fig. 5.32 2D probability density of (a) the COF and related slope at a slip of 15% and (b) COF at 15% slip and maximum COF.

The parameters of the two identified traction curves (called “High 1” and “High 2”) which occur the most in the first three measuring nights are plotted in Fig. 5.33 summarized in Table 5.4 (section 5.4.7.4).

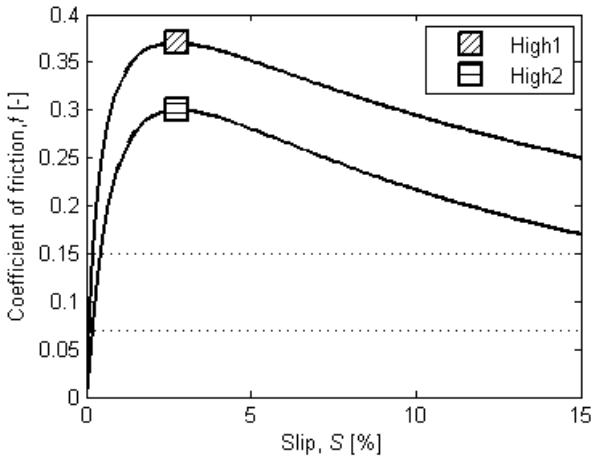

Fig. 5.33 Representative traction curves measured on the tracks in the Netherlands on the first three measuring days of autumn 2008 (see Fig. 5.19 and Fig. 5.25).

The same kind of discussion as described above applies to the rest of the traction curves by keeping the classes as mentioned in Table 5.3, i.e. medium friction (Fig. 5.39 to Fig. 5.43) and low friction (Fig. 5.44 to Fig. 5.48). The details are not given further except for the same plots concerning the statistical data. As a remark, the correlations for these cases showed one point summit concentrations in the 2D plots so one traction curve for each case was identified. A summary of the results is given in Table 5.4.

High friction (rest of the nights)

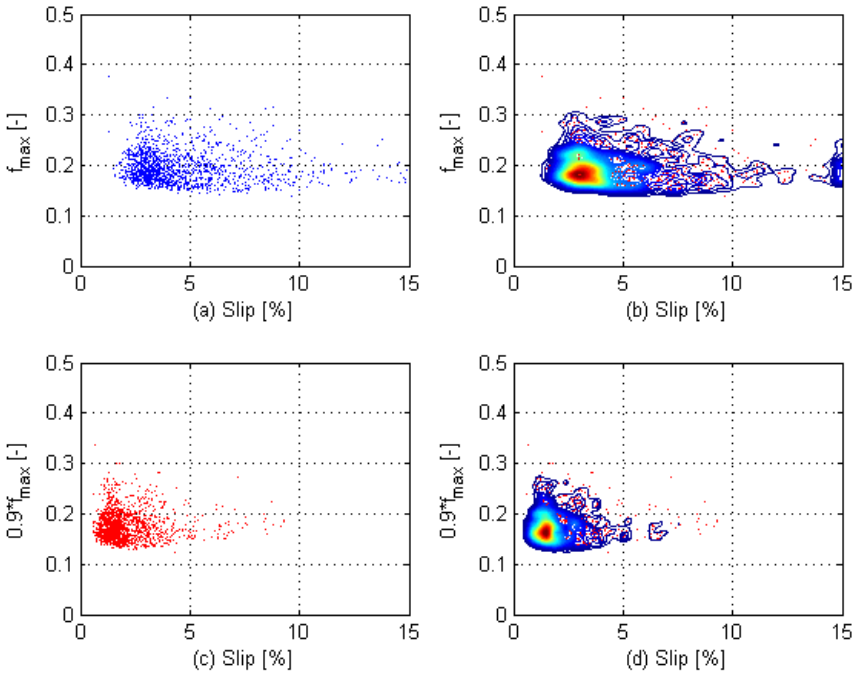

Fig. 5.34 Statistical data for the second subclass of high friction data:
(a) maximum COF as a function of slip and (b) 2D probability density of the max COF and slip;
(c) and (d) same for 0.9 of the max COF.

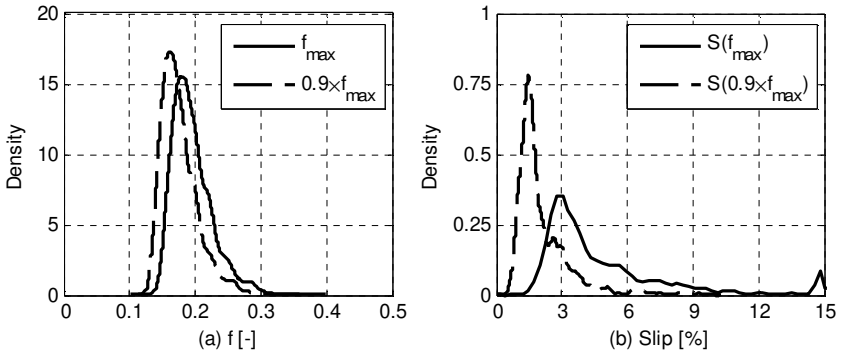

Fig. 5.35 Probability density of maximum COF (continuous line) and
0.9×maximum COF (dashed line) against related slip.

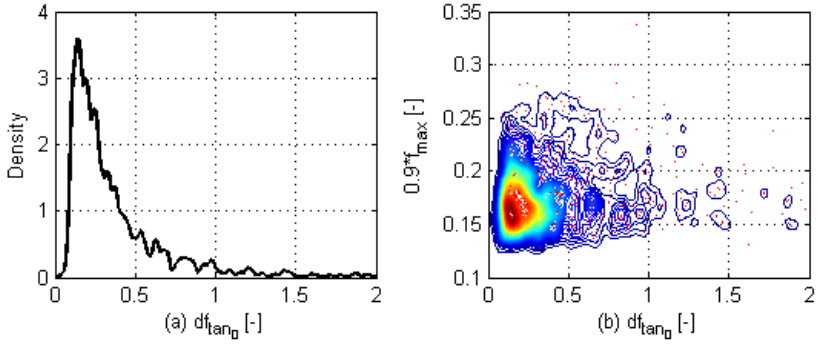

Fig. 5.36 Slopes at rolling: (a) probability density of all slope values and (b) correlation between $0.9 \times f_{max}$ and slope.

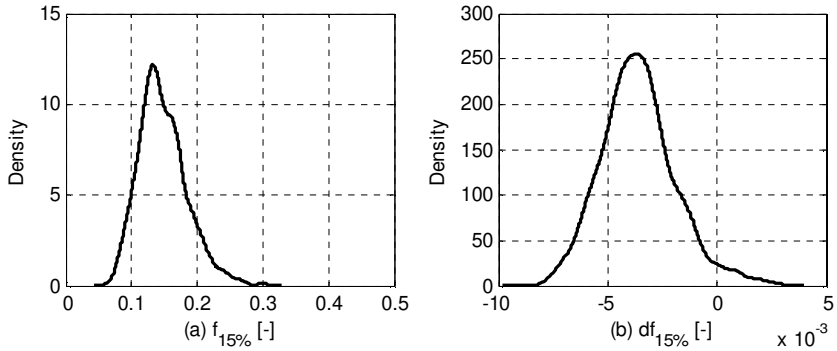

Fig. 5.37 Probability density of the coefficient of friction and related slope at a slip of 15%.

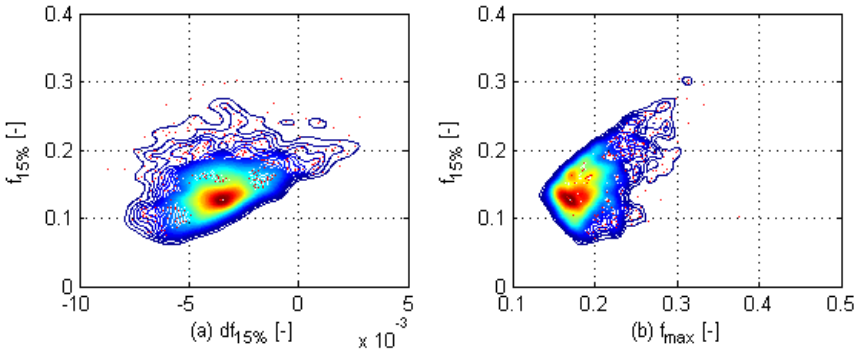

Fig. 5.38 2D probability density of (a) the COF and related slope at a slip of 15% and (b) COF at 15% slip and maximum COF.

Medium friction

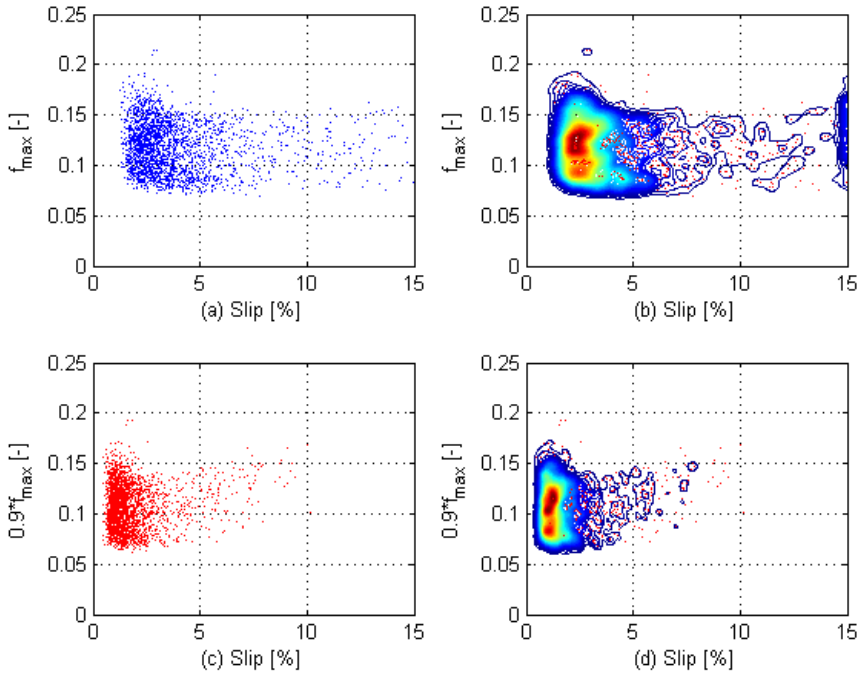

Fig. 5.39 Statistical data for the medium friction data: (a) maximum COF as a function of slip and (b) 2D probability density of the max COF and slip; (c) and (d) same for 0.9 of the max COF.

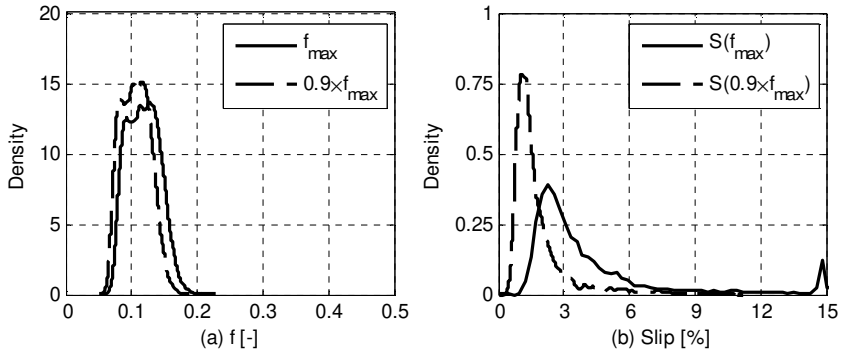

Fig. 5.40 Probability density of maximum COF (continuous line) and 0.9×maximum COF (dashed line) against related slip.

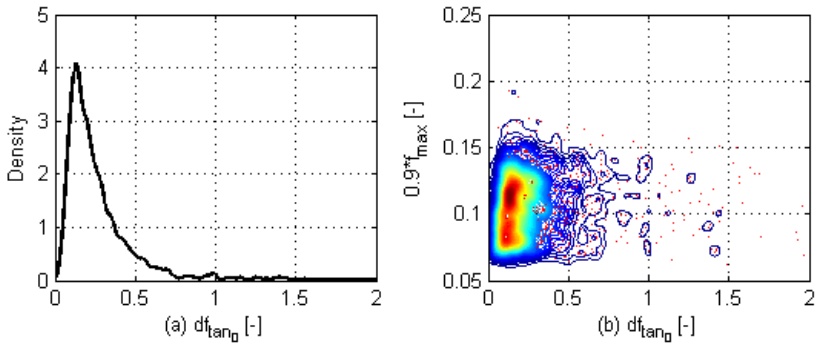

Fig. 5.41 Slopes at rolling: (a) probability density of all slope values and (b) correlation between $0.9 \times f_{max}$ and slope.

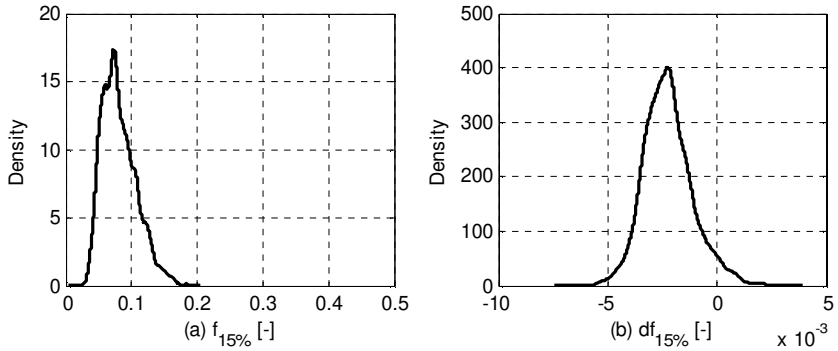

Fig. 5.42 Probability density of the coefficient of friction and related slope at a slip of 15%.

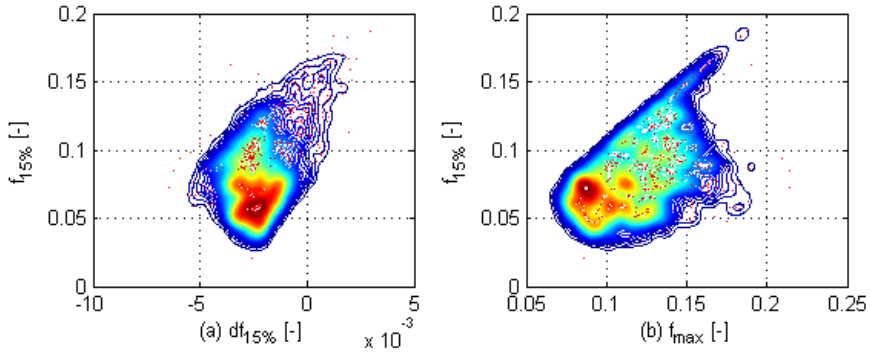

Fig. 5.43 2D probability density of (a) the COF and related slope at a slip of 15% and (b) COF at 15% slip and maximum COF.

Low friction

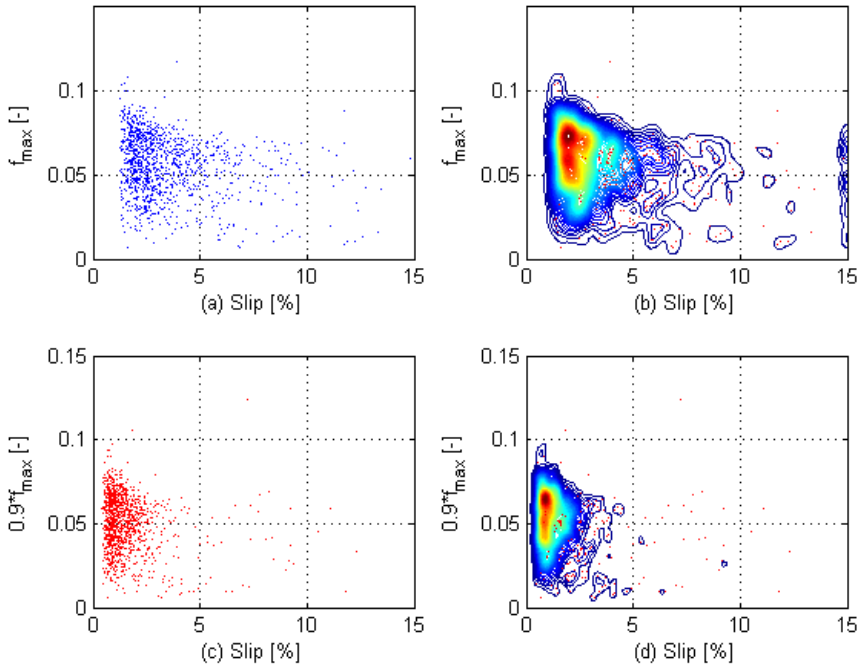

Fig. 5.44 Statistical data for the low friction data: (a) maximum COF as a function of slip and (b) 2D probability density of the max COF and slip; (c) and (d) same for 0.9 of the max COF.

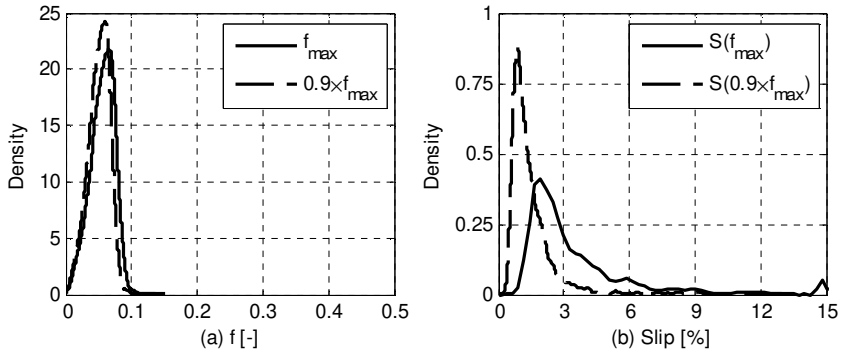

Fig. 5.45 Probability density of maximum COF (continuous line) and 0.9×maximum COF (dashed line) against related slip.

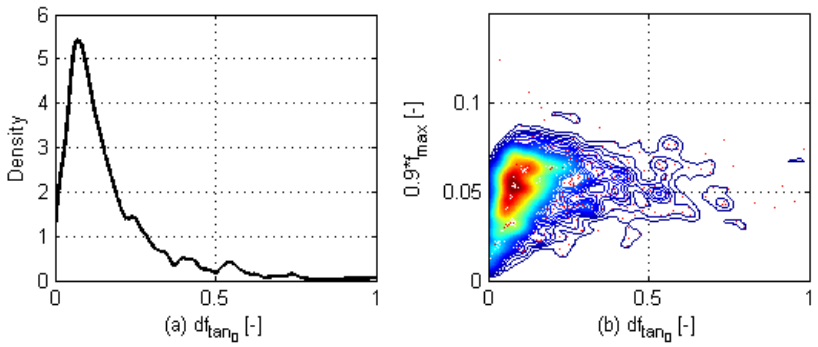

Fig. 5.46 Slopes at rolling: (a) probability density of all slope values and (b) correlation between $0.9 \times f_{max}$ and slope.

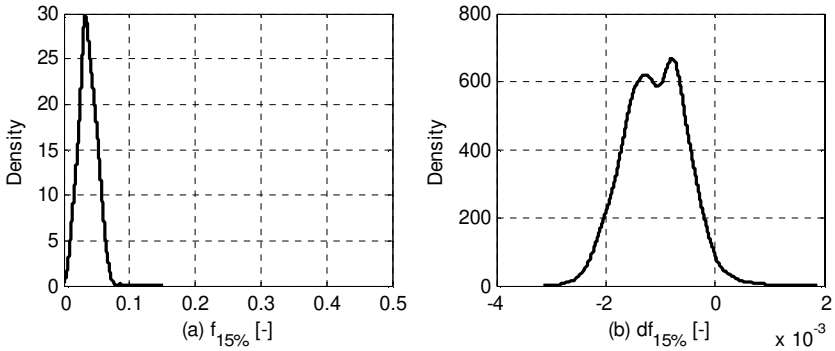

Fig. 5.47 Probability density of the coefficient of friction and related slope at a slip of 15%.

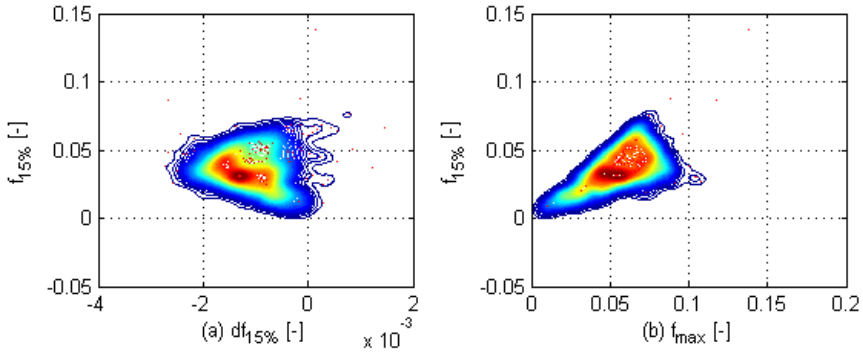

Fig. 5.48 2D probability density of (a) the COF and related slope at a slip of 15% and (b) COF at 15% slip and maximum COF.

5.4.7.4 Identified traction curves

The parameters extracted from the statistical plots presented in the previous section are shown in Table 5.4.

Table 5.4: Identified classes of traction curves.

Parameter	High 1	High 2	High 3	Medium	Low
Slope at zero slip	0.70	0.30	0.15	0.13	0.07
Maximum COF	0.37±0.053	0.30±0.038	0.18±0.031	0.11±0.024	0.065±0.018
Slip at Maximum COF	2.75	2.75	3.00	2.30	2.00
0.9 * Maximum COF	0.33±0.048	0.26±0.034	0.16±0.028	0.10±0.022	0.06±0.016
Slip at 0.9 * Maximum COF	1.20	1.20	1.50	1.10	0.90
COF at 15%	0.25±0.043	0.17±0.031	0.13±0.037	0.07±0.026	0.033±0.014
Slope at 15%	-0.008	-0.0065	-0.0036	-0.0023	-0.0013

These five traction curves are the most representative for the measuring nights. Their fit parameters in Eq. 5.2 are given in Table 5.5 and according shape in Fig. 5.49.

Table 5.5: Fit parameters for the identified classes of traction curves (Eq. 5.2).

Fit parameter	High 1	High 2	High 3	Medium	Low
$a^{\#} = f_{max}$	0.37	0.30	0.18	0.11	0.065
$b^{\#}$	0.98	1.03	1.28	1.05	0.83
$c^{\#}$	7.58	4.98	6.19	5.94	5.16

Rheological parameters can also be extracted from the traction curve corresponding to the low friction case assuming the lubrication regime is solid state behaviour EHD. Since the maximum coefficient of friction is 0.065 such assumption is realistic. The procedure is shown in Chapter 4, section 4.3.1. Rheological parameters are to be used for the prediction of the Stribeck curve as presented in Chapter 3, when a train is running on such interfacial layer.

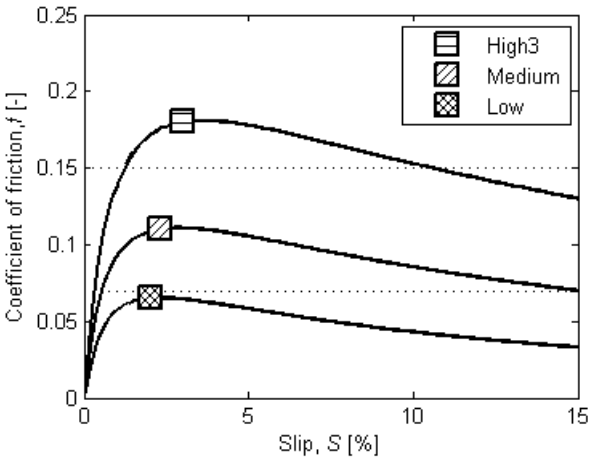

Fig. 5.49 The three representative traction curves measured on tracks in the Netherlands. October and November 2008.

5.4.8 Conclusions and recommendations

The measuring campaign lasted for the entire autumn of 2008 and was carried out during the nights on three different tracks within the Dutch rail network. 80% of the measured coefficient of friction lay within the interval of 0.05 - 0.2. Therefore, future coefficients of friction considered in calculations should be verified with this range. Only 34% of the values are higher than 0.15 (the value after which the NS timetable is scheduled).

Five traction curves which are most representative were identified by the use of a statistical approach and their complete description is detailed in section 5.4.7.4.

As an important finding we note that the slip where the maximum COF is reached in all classes is lower than 3%. Actual slip for the WSP system is 15%.

Chapter 6

Model application to wheel - rail contact

The developed friction model for lubricated elliptical contacts, described in Chapter 3, was validated in the laboratory, Chapter 4, and applied to the wheel - rail contact situation, Chapter 5. This chapter stands for applying the model for extracting rheological parameters of the interfacial layer from the traction curves measured with the train tribometer.

6.1 Model validation using the Tribometer

For establishing a connection between the friction model presented in Chapter 3 and the tribometer described in section 5.4, a set of tests under controlled conditions were conducted on the stabling yard of Rotterdam.

The idea was to manually contaminate a large part of the track with a lubricant of known rheological properties and then perform measurements on it.

6.1.1 The contamination

The chosen contaminant is the same biodegradable grease used for the measurements with the device presented in section 5.3. The grease is called KajoBio [70] and in the Dutch railroad is applied in curves for wheel flange - rail lubrication.

The rheological properties of the grease were extracted from two disk machine tests, performed with cylindrical disks. The entire procedure, similar with the parameter estimation presented in section 4.3.1, is described in detail in [76].

In particular the Eyring shear stress parameter was found to vary with the contact pressure and sum velocity (Fig. 6.1).

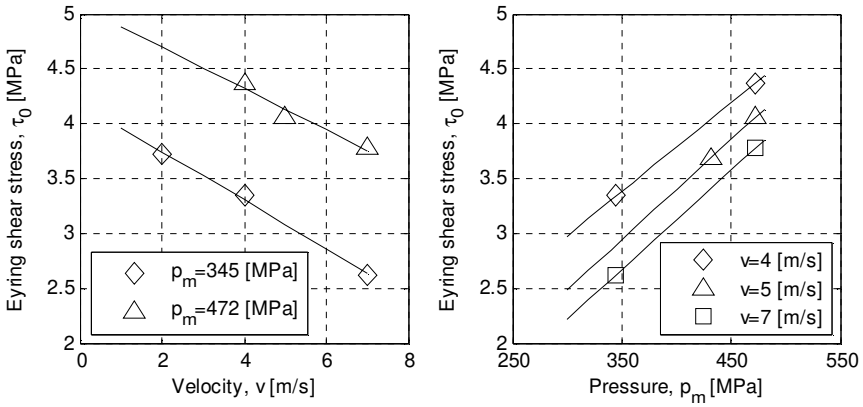

Fig. 6.1 Eyring shear stress values for the KajoBio extracted from the two disk machine tests for different contact pressures and sum velocities.

The extracted values were fit with Eq. 4.5 and the results are also plotted in Fig. 6.1. The fit parameters together with the other rheological properties to be used as input in the model are summarized in Table 6.1.

Table 6.1: Grease (KajoBio) properties [76].

Property	Value	Unit	Description
η_0	0.255	Pa·s	Viscosity at ambient pressure (T_0 = 20 °C)
z	0.4	-	Roelands pressure-viscosity index
S_0	-	-	Temperature viscosity index
α	11.3	GPa^{-1}	Barrus pressure - viscosity coefficient
τ_0^*	1	MPa	Reference shear stress
p_0^*	0.1	GPa	Reference pressure
v_0^*	≈ 0	m/s	Reference sum velocity
$tg(\alpha_p)$	8.8×10^{-3}	-	Shear stress - pressure slope
$tg(\alpha_v)$	-2.05×10^{5}	-	Shear stress - velocity slope

6.1.2 The measurements

The rolling stock on which the tribometer was mounted (Fig. 5.16) was described in detail in section 5.4.3 and its measurement description in section 5.4.4. The track has a length of 500 m and the maximum allowed velocity on it is 30 km/h. The grease was manually applied by "painting" the rail over a distance of 100 m. The model inputs regarding the measuring wheel operational conditions are: $R_{wx} = R_{wy} = 50$ mm at a normal load $F_N = 1.2$ kN.

Several passes were made over the contaminated area and a few of the measured traction curves together with the model predictions are shown in Fig. 6.2. The tests were repeated three times, i.e. three runs over the same contamination, after which KajoBio is applied again on the track.

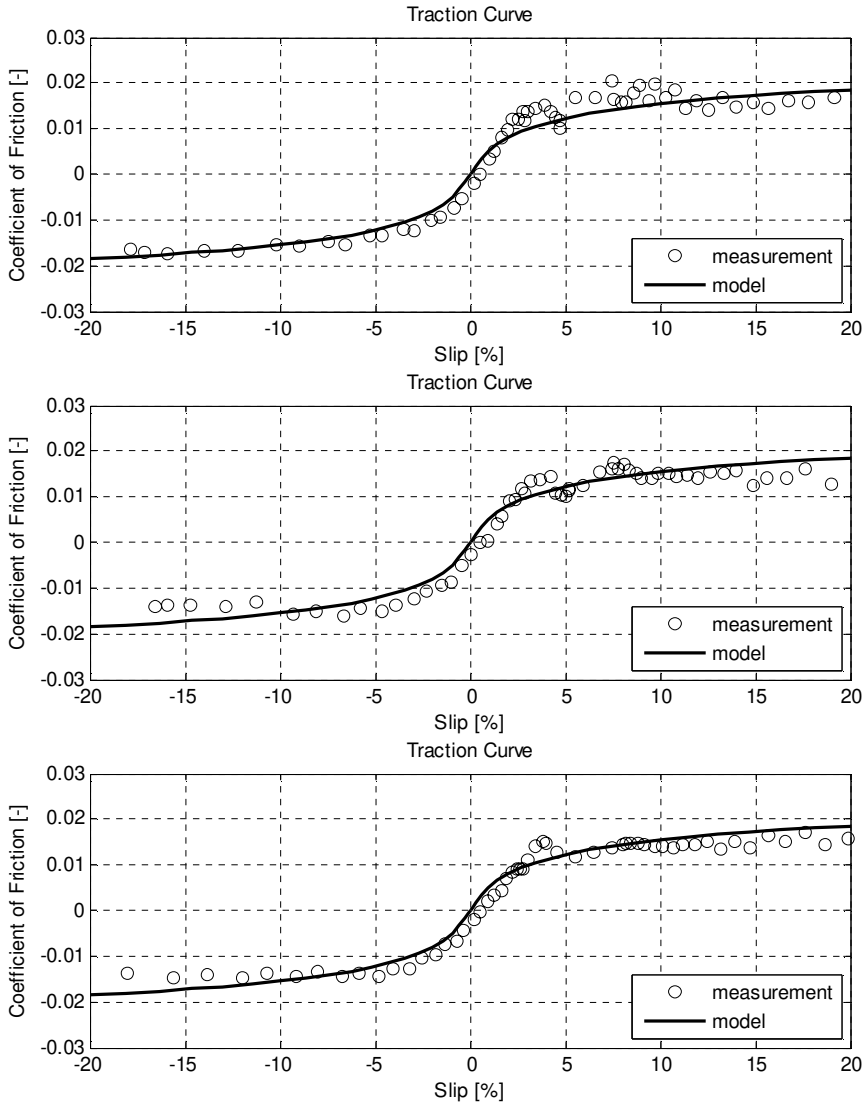

Fig. 6.2 Model predictions and tribometer measurements when running over a track contaminated with KajoBio. Traction curves are measured over a distance of 49 m in 6 s, train velocity 8.2 m/s, outside temperature 7 ºC.

6.1.3 Summary

The on-track friction experiment proposed and conducted, had the goal to prove that the measured values are in agreement with the microcontact and friction model predictions described in Chapter 3. For that purpose, measurements were performed with a known grease used by the Dutch network infrastructure manager, ProRail, for wheel flange - rail lubrication in curves. Two disk machine experiments were conducted with the KajoBio grease in order to extract its rheological properties [76]. These properties were used in the friction model and the predicted results were found to be in good agreement with the measured values.

6.2 Prediction of friction measurements with the train tribometer

Once the tribometer measurements show reliable results in comparison with the predictions of the model, the traction curves measured in section 5.4 will be used to identify the rheological properties of the interfacial layer. As stated before (section 5.4.6.7), the number of the traction curves measured in the autumn campaign of 2008 on the Dutch rail network, was very large, i.e. approx 6000. Therefore, only a few characteristic curves are chosen for the rheological description (Fig. 6.3).

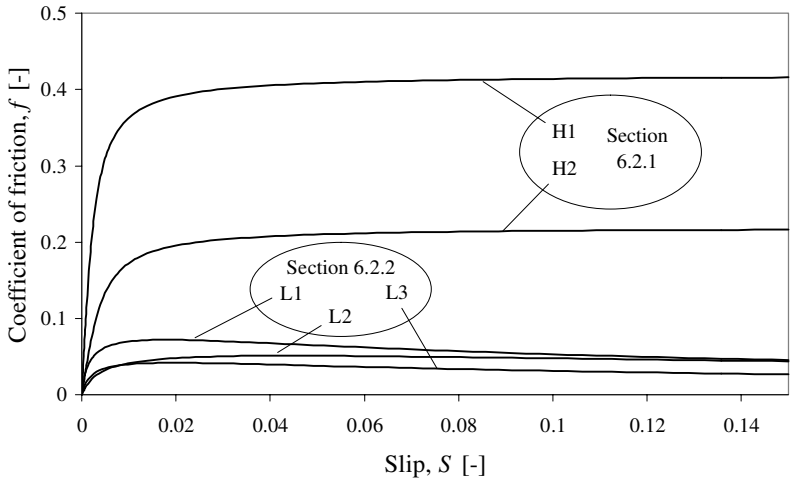

Fig. 6.3 Friction measurements from low to high (F_N = 1200 N, v_{train} = 22 m/s).

Fig. 6.3 plots five arbitrarily measured traction curves in the form given by Eq. 5.2. These traction curves will be the case study for the next two subsections.

6.2.1 High friction (BL)

Fig. 6.4 plots the two examples of measured traction curves at high friction (Fig. 6.3), both presenting an asymptotic behaviour as described by Eq. 3.29.

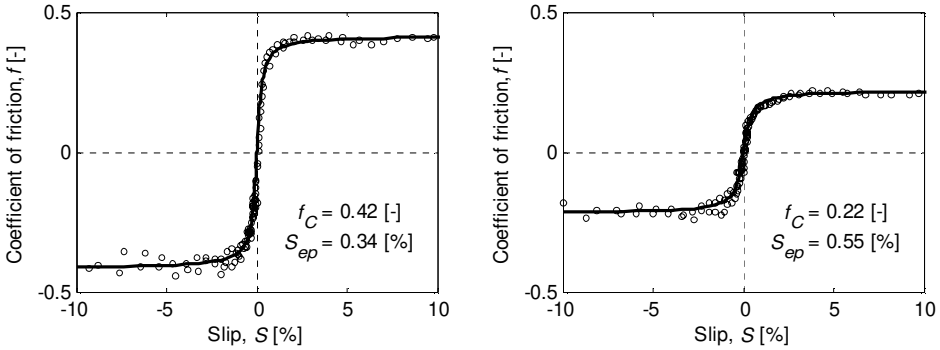

Fig. 6.4 High friction traction curves: (o) model and (-) measurements (F_N = 1200 N, v_{train} = 22 m/s).

Since the coefficient of friction reaches rather high values, i.e. 0.2 to 0.4, the lubrication regime for the considered traction curves in Fig. 6.4 is BL. The two measurements were performed on different days and were chosen to show that the coefficient of friction in BL regime, f_C, as well as the slip at the transition from elastic to plastic behaviour of the boundary layer, S_{ep}, may vary slightly from measurement to measurement due to different layers (friction level varies). The identified parameters are given in Table 6.2.

Table 6.2: Identified parameters on the high friction traction curves.

Parameter	Unit	H1	H2
f_C	[-]	0.42	0.22
S_{ep}	[%]	0.34	0.55

The name “H1” and “H2” refer to the traction curves in Fig. 6.4 (left) and (right) respectively.

6.2.2 Low friction (EHL)

The same discussion is proposed for the low friction data. The first parameter to be extracted is the Eyring shear stress and the apparent viscosity (Fig. 6.5).

One of the three traction curves with low friction of which the logarithm normal fit function, Eq. 5.2, is applied (shown in Fig. 6.3) is used as an example for obtaining the Eyring shear stress. The function fit and measured data points are plotted in Fig. 6.5 (left). As described in section 4.3.1.2, if the function fit is plotted as the

shear stress, τ_H (Eq. 4.1), function of the natural logarithm of the shear rate, $\ln(\dot{\gamma})$ (Eq. 4.2), the inclination of the tangent in the inflection point of the curve, is a direct reading of the Eyring shear stress (Eq. 4.3), the maximum of the first derivative. The intersection between this tangent and the $\ln(\dot{\gamma})$ axis will determine the apparent viscosity in the contact (Eq. 4.4). For the example shown in Fig. 6.5 the determined Eyring shear stress is 15.7 MPa and the apparent viscosity is 1×10^6 Pas.

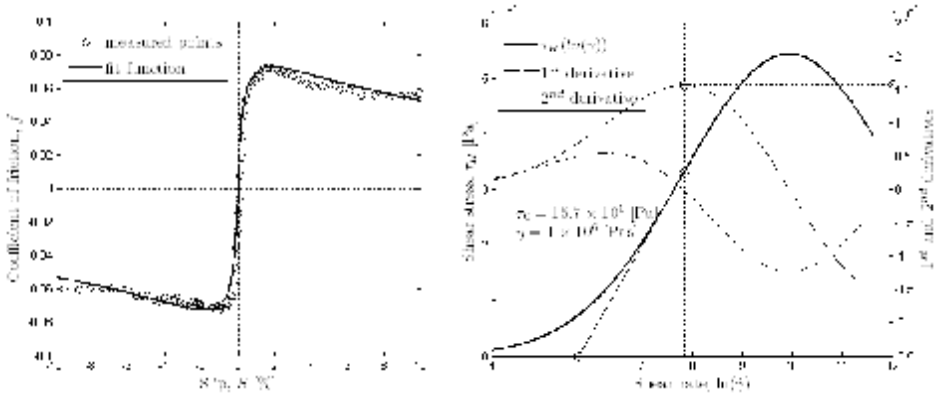

Fig. 6.5 Eyring shear stress and viscosity determined from the traction curve, F_N = 1200 N, v_{train} = 22 m/s.

The rheological parameters extracted for the low friction examples, referred as "L1", "L2" and "L3", in Fig. 6.3 are summarized in Table 6.3 and the comparison between the model results and the measurements are plotted in Fig. 6.6. The traction curves were measured at different tracks, i.e. different layers, and as a result the values for the parameters differ (F_N and v_{train} are equal).

Table 6.3: Rheological parameters of the low friction traction curves.

Parameter	Unit	L1	L2	L3
τ_0	[MPa]	15.7	12.0	10.0
η_0	[Pas]	0.6	0.4	0.55
z	[-]	0.470	0.455	0.440
S_0	[-]	1.5	1	2.5

The examples show good agreement between the measurements and the model predictions (Fig. 6.6).

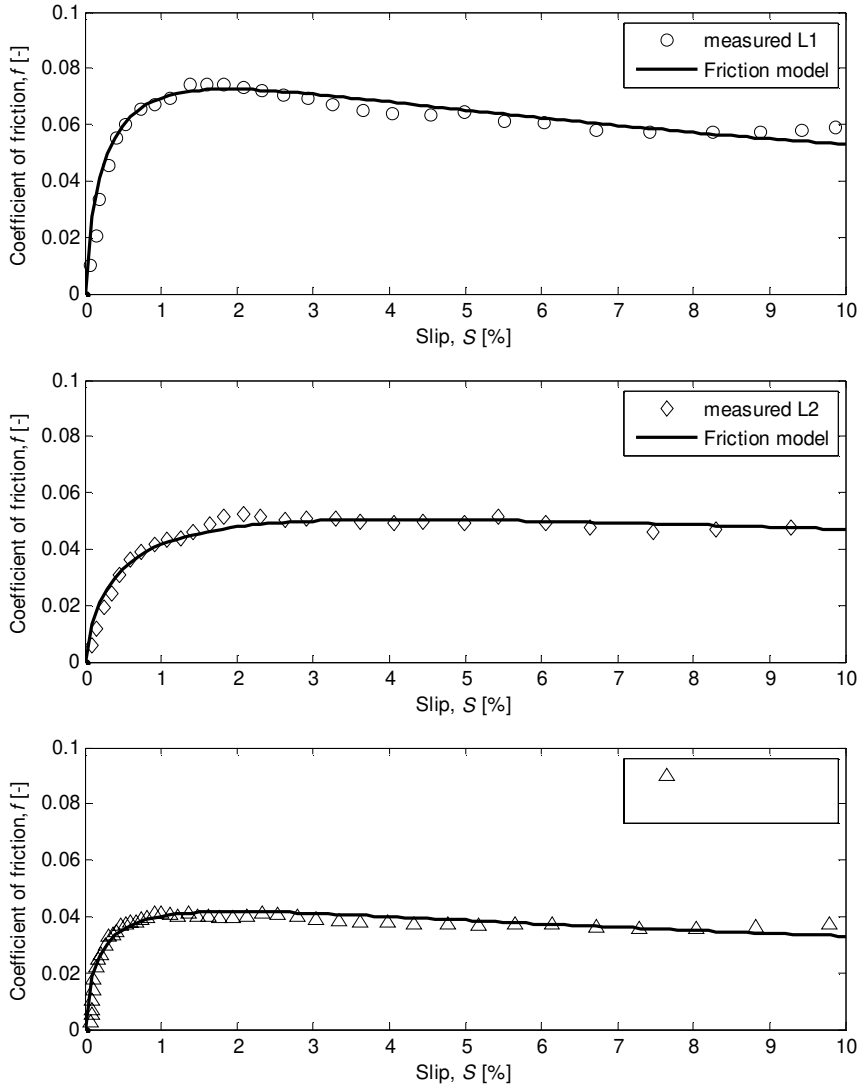

Fig. 6.6 Low friction traction curves, model and measurements: ○ "L1", ◊ "L2" and Δ "L3" (F_N = 1200 N, v_{train} = 22 m/s).

6.2.3 Not-Eyring measured traction curves

During the rheological study of the measured traction curves, it was observed that some of the curves could not be fitted with the Eyring based friction model, Eq. 3.23 and for the friction, Eq. 3.25, in particular for low slip values. Two examples are given in Fig. 6.7.

The first curve referred as “Ref” is, in fact, the traction curve with the lowest coefficient of friction in Fig. 5.49. The curve referred to as “Ex” is arbitrarily chosen, which clearly show a difference between the measured friction and friction model at low slip values. For these two examples, the rheological properties are extracted as described in the previous section and are given in Table 6.4. When the model predictions are plotted together with the measurements (Fig. 6.7), a significant difference is observed on the first part of the curve. Such behaviour is due to viscoelastic behaviour of the interfacial layer [9, 77].

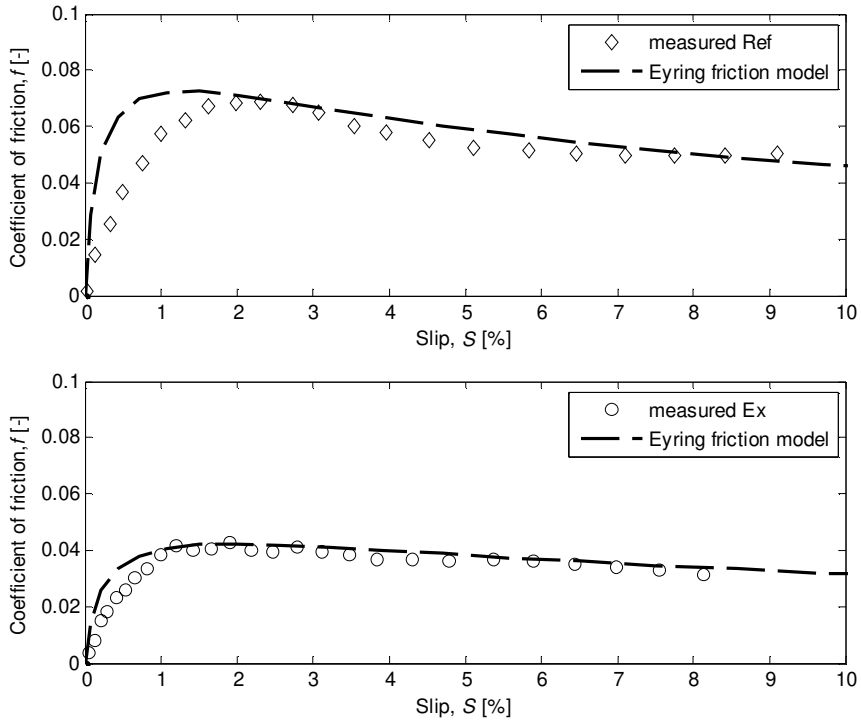

Fig. 6.7 Measurements showing different than Eyring shear behaviour.

Table 6.4: Rheological parameters of the layer showing different than Eyring behaviour.

Parameter	Unit	Ref	Ex
τ_0	[MPa]	18.5	10.0
η_0	[Pas]	0.6	0.55
z	[-]	0.465	0.440
S_0	[-]	2.0	2.5

Therefore, to be able to accurately describe the shear behaviour of the interfacial

layer as measured between wheel and rail, viscoelasticity must be implemented in the friction model. So, the next subsections deal with the viscoelasticity modelling of the interfacial layer.

6.2.3.1 Modelling the viscoelastic behaviour of the interfacial layer

The presented model will be used for the prediction of the coefficient of friction within the wheel - rail contact when the train will run over slippery tracks. In the previous sections the shear behaviour of the interfacial layer was governed by the Eyring model (Eq. 3.23) whereas the coefficient of friction in the BL regime was of Coulomb type. In this section, the model will be extended to include viscoelastic behaviour of both interfacial and boundary layer.

For an easier discussion and comparison between the described models, there are a few dimensionless numbers to be set:

$$\bar{\tau} = \frac{\tau}{\tau_i} \tag{6.1}$$

$$\xi = \frac{\eta\dot{\gamma}}{\tau_i} \tag{6.2}$$

Where the index i can be $i \equiv 0$ for Eyring based models or $i \equiv L$ for the limiting shear stress based models [78,79,80]. The $\dot{\gamma}$ parameter is the shear rate (Eq. 3.22).

The available shear models

The general model for describing the shearing of lubricants in EHL contacts is:

$$\xi = f(\bar{\tau}) \tag{6.3}$$

Where $f(\bar{\tau})$ represents the existing shear models:

Elastic - fully plastic:
$$f(\bar{\tau}) = \begin{cases} \bar{\tau} & \text{for} \quad \bar{\tau} < 1 \\ 1 & \text{for} \quad \bar{\tau} \geq 1 \end{cases} \tag{6.4}$$

Eyring:
$$f(\bar{\tau}) = \sinh(\bar{\tau}) \tag{6.5}$$

Bair & Winer [78]:
$$f(\bar{\tau}) = -\ln(1-\bar{\tau}) \tag{6.6}$$

Gecim & Winer [79]:
$$f(\bar{\tau}) = \operatorname{atanh}(\bar{\tau}) \tag{6.7}$$

Elsharkawy & Hamrock [80]:
$$f(\bar{\tau}) = \bar{\tau}\left(1-\bar{\tau}^n\right)^{-1/n} \tag{6.8}$$

The above-mentioned shear models are shown in Fig. 6.8.

For describing viscoelastic behaviour of the boundary layer, the general shear model in Eq. 6.3 will be extended to a Maxwell based model.

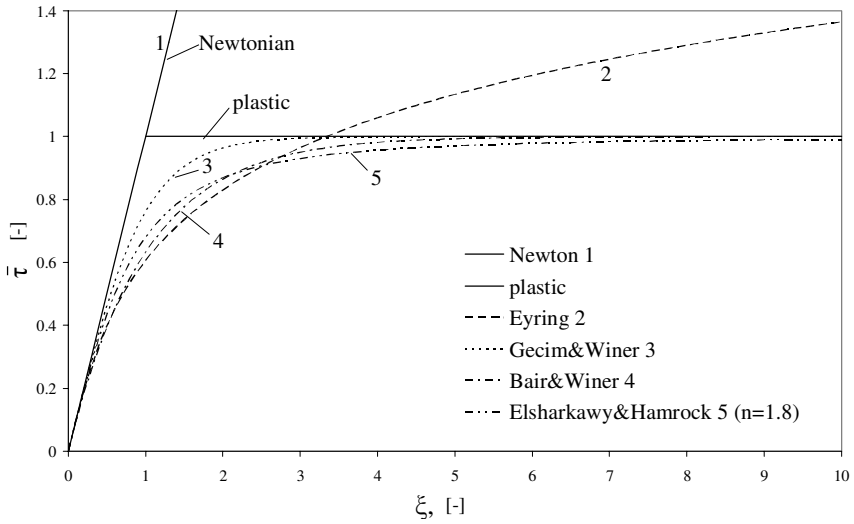

Fig. 6.8 Shear models.

The viscoelastic Maxwell model

A Maxwell based model is represented by an elastic spring with a shear modulus, *G'*, and a viscous damper with a viscosity, η, governed by one of the laws presented in Eq. 6.4 - 6.8. A schematic representation of a Maxwell based model is shown in Fig. 6.9.

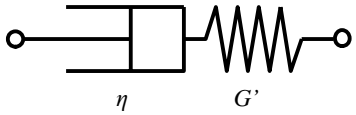

Fig. 6.9 Maxwell model.

The governing equation for such a model, keeping the form of the general model in Eq. 6.3, is given by:

$$\xi = \frac{\eta}{G'}\frac{d\bar{\tau}}{dt} + f(\bar{\tau}) \tag{6.9}$$

Where, $f(\bar{\tau})$ has one of the shear model forms (Eq. 6.4 - 6.8).

Eq. 6.9 is an ordinary differential equation of the first order, with the shear stress dependent of time, which will be solved numerically. The boundary condition is given by the value of the shear stress at initial time (at the boundary of the contacting area), which is zero: $\bar{\tau} = 0$ when $t = 0$.

Considering now a sliding elliptical contact in the presence of an interfacial layer which follows the above-presented behaviour and assuming for it a steady flow in the contact interface, this reads:

$$\frac{d}{dt} = U \cdot \frac{d}{ds} \tag{6.10}$$

Where $U = v^+/2$ is the mean rolling velocity.

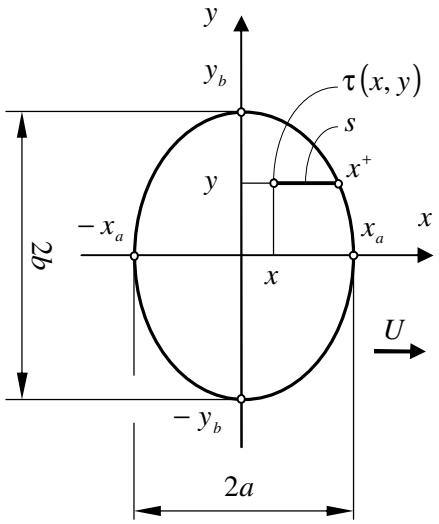

Fig. 6.10 Contact ellipse and shear stress calculation.

Further, assuming that the contacting bodies roll in the x direction of the contact ellipse, from Fig. 6.10, we can write:

$$s = x^+ - x \tag{6.11}$$

Where,

$$x^+ = a \cdot \sqrt{1 - \frac{y^2}{b^2}} \tag{6.12}$$

This means that for a given value of $y \in [-b, b]$, the corresponding positive value of x on the ellipse is in fact x^+ given by Eq. 6.12. So, according to Eq. 6.10 and the above, the time variable in Eq. 6.9 can be changed as follows:

$$\xi = D\frac{d\bar{\tau}}{dX} + f(\bar{\tau}) \tag{6.13}$$

The boundary condition changes to: $\bar{\tau} = 0$ when $X = X^+$. D is called Deborah

number and is given by:

$$D = \frac{\eta \cdot U}{a \cdot G'} = \frac{\eta \cdot v^{+}}{2 \cdot a \cdot G'} \tag{6.14}$$

X, Y are the dimensionless axes of the contact ellipse and X^{+} is the maximum value which X can have for a given value of Y:

$$X = \frac{x}{a}; \quad Y = \frac{y}{b} \quad \text{and} \quad X^{+} = \sqrt{1 - Y^{2}} = \frac{x^{+}}{a} \tag{6.15}$$

The final form of a Maxwell based model written in the form ready for numerical computation, by separating the two dependent variables (X and $\bar{\tau}$) is given by:

$$\frac{dX}{D} = \frac{d\bar{\tau}}{\xi - f(\bar{\tau})} \tag{6.16}$$

In order to calculate the friction force given by this type of interfacial layer, first the shear stress, τ, must be derived from the above-presented model.

Results of the Maxwell based shear models

Eq. 6.16 is a first order differential equation and its solution is derived by integrating it numerically. The numerical solver is described in Appendix G. However, the first two presented shear models, given by Eq. 6.4 and Eq. 6.5 can be solved analytically and the procedure is detailed in Appendix H.

The results of the presented Maxwell based models (Eq. 6.13) are shown in Fig. 6.11. It can be seen that with increasing the value of the Deborah number, D (Eq. 6.14), the shear stress shifts to the right when plotted against the dimensionless number, ξ (Eq. 6.2). In fact, when $D << 1$, the interfacial layer has a viscous behaviour and when $D \geq 1$, elastic behaviour starts to have effect.

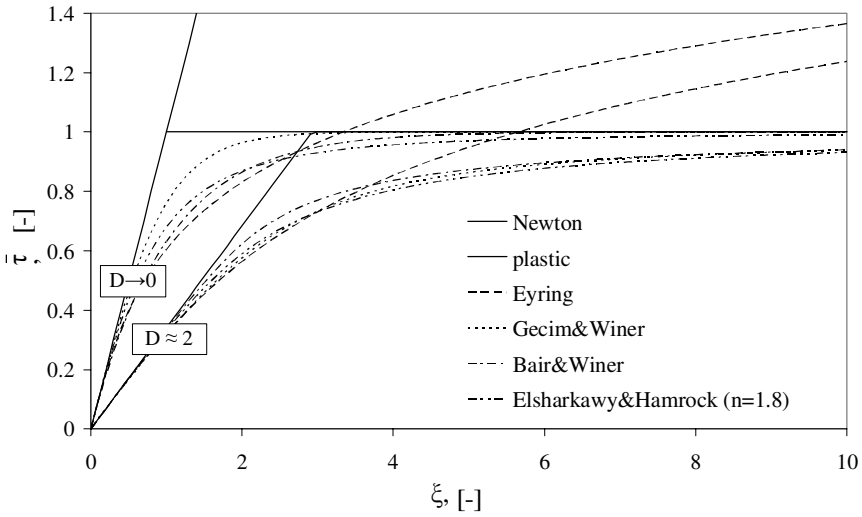

Fig. 6.11 Maxwell based shear models.

Friction force, generated by shearing a viscoelastic layer

After calculating the shear stress evolution over the contact area, the next step is to calculate the friction force by integrating the shear stress over the elliptical domain. The general mathematical formulation in the dimensionless form is:

$$\overline{F}_f = \frac{F_f}{\tau_i \cdot \pi \cdot a \cdot b} = \frac{1}{\pi} \iint_{\overline{A}} \overline{\tau}(X,Y) \cdot d\overline{A} = \frac{2}{\pi} \int_0^1 \int_{-X^+}^{X^+} \overline{\tau}(X,Y) \cdot dX \cdot dY \qquad (6.17)$$

$$\overline{A} = \left\{ X^2 + Y^2 \le 1; \quad Y \in [0,1]; \quad X \in \left[-X^+, X^+ \right] \right\} \qquad (6.18)$$

where, $\overline{A}$ is the dimensionless half elliptical domain. The index i can be either $i \equiv 0$ for the Eyring or $i \equiv L$ for the limiting shear stress models. X^+ is given by Eq 6.15.

For the Maxwell – Newton model, an analytical solution was given by Johnson and Roberts [77]. Their solution and an empirical approximation of the numerical results are given in Appendix I.

6.2.3.2 Experimental validation of the viscoelastic model

The shear modulus of the interfacial layer (viscoelastic) was determined by using the method described in [81] (Appendix J). For both cases presented in Fig. 6.7 and Table 6.4 (“Ref” and “Ex”), the shear modulus, *G’*, was found to be 45 MPa. The results of the friction model incorporating viscoelastic behaviour and using Eyring shear behaviour (Eq. 6.5) are plotted together with the measured points in Fig.

6.12.

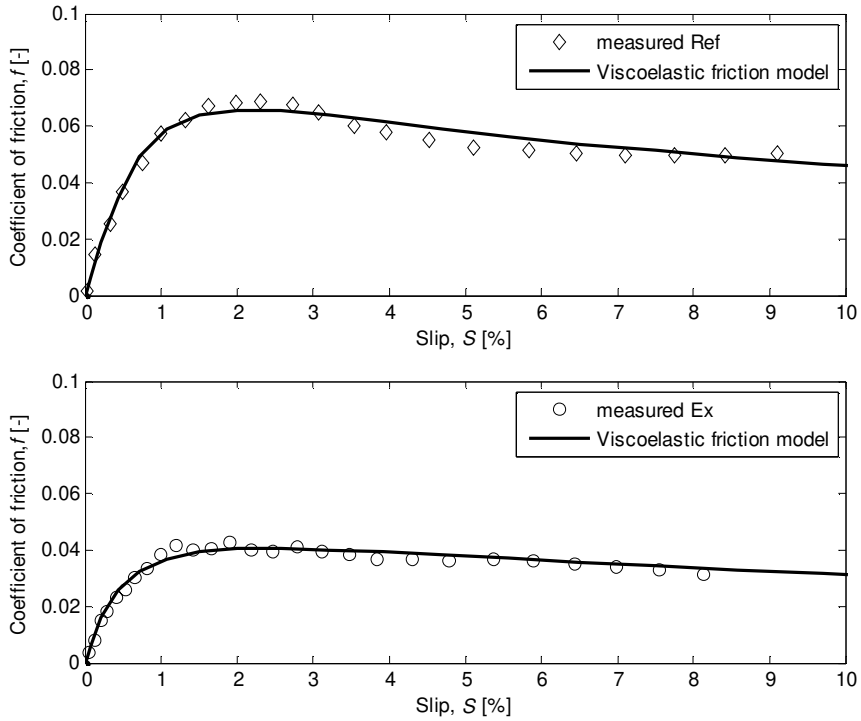

Fig. 6.12 Viscoelastic model and measurement results (G' = 45 MPa): ◊ "Ref" and ○ "Ex".

Good agreement is found between the new friction model (viscoelasticity included) and measured traction curves.

6.2.3.3 Friction in the BL regime

In order to apply the viscoelastic behaviour to the BL regime, some assumptions have to be adopted:

- The friction in the BL regime is given by shearing the boundary layer between the contacting asperities.
- The shear behaviour of the boundary layer is viscoelastic (Maxwell type).
- In boundary lubricated contacts, the slip is the same for all asperity microcontacts.

The friction force generated in a pair of asperities in contact, F_{f_i}, can be calculated along the $\dot{\gamma}$ vectors, by integrating the shear stress (given by the model according to the assumed behaviour of the interfacial layer), over the contact area, A_i

(according to Eq. 6.17), where $i \in 1...N$ (N being the number of pairs of asperities in contact). The friction force in the BL regime is given by the sum of the contributions of all the contacting asperities:

$$F_{f,BL} = \sum_{i=1}^{N} F_{f_i} \tag{6.19}$$

In this way, the Maxwell type model, (Eq. 6.9), adapted to the existing rheological models (Eq. 6.4 through 6.8) can be used for the prediction of the coefficient of friction in the BL regime.

6.2.4 Conclusions

The measured high friction traction curves are well described by the friction force for rolling/sliding contacts in the BL regime (Eq. 3.29). The Coulomb coefficient of friction, f_C, and the slip at the transition from elastic to plastic behaviour of the boundary layer, S_{ep}, are easily identified.

The measured low friction traction curves are in agreement with the shear model of Eyring (Eq. 3.23) resulting in the friction force for the EHL regime given by Eq. 3.25. The extraction of the rheological parameters is more difficult and in most of the situations, the interfacial layer causing low friction has viscoelastic behaviour. Methods for extracting the rheological parameters are presented and some examples are discussed.

Part of the measured traction curves show a non-viscous type of behaviour for the interfacial layer, so they could not be described by the Eyring model. For this purpose, the present friction model was extended to include also viscoelastic behaviour of both interfacial and boundary layer. New predictions show good correlation with the measured traction curves, for the low friction cases (assumed to act in the EHL regime). For validation, frictional heating, was taken into account.

It was also shown that the Maxwell type model, (Eq. 6.9), adapted to the existing rheological models (Eq. 6.4 through 6.8) can be used for the prediction of the coefficient of friction in the BL regime by assuming that the friction in the BL regime is generated by shearing the boundary layer. The friction force generated in a pair of asperities is calculated by integrating the shear stress over the microcontact area (Eq. 6.17) and the total friction force in the contact is found by summing the contribution of all the contacting asperities (Eq. 6.19).

Chapter 7

Conclusions and recommendations

This chapter closes the research concerning friction in the wheel - rail contact, in particular the slippery track issue. Conclusions are drawn here as well as proposed future work regarding the mentioned topic.

7.1 Conclusions

Based on a study of the literature and contact calculations made, it was concluded that the wheel - rail contact can be regarded as an elliptical contact problem. For an accurate prediction of the friction levels in the presence of an interfacial layer of non-Newtonian behaviour, a new Mixed Lubrication friction model for the elliptical contact situation was developed.

7.1.1 Friction model

A good agreement was found between the presented elliptical model and the proposed equivalent line contact. Different parameters were varied in order to study their influence on the Stribeck curve and separation. The variations noticed were similar to the existing friction model for line contacts, i.e. Gelinck [34] and Faraon [38]. The most significant influences in the Stribeck curve are in the ML regime which shifts to the left (the coefficient of friction decreases) with increasing viscosity of the lubricant and with decreasing of surface roughness. The Stribeck curve hardly shifts by changing the load. Not less important are the changes in the EHL regime where friction increases with increasing both normal load and

viscosity of the lubricant. Of course, the roughness in EHL regime has no influence on the friction level.

Further, the ML friction model was extended to include frictional heating and film thickness reduction due to oil inlet temperature increase and starvation. The considered frictional heating model is the model of Bos and Moes [49] (Eq. 3.34) and the film thickness correction factor chosen is as given by Pandey [51] (Eq. 3.38). The model was applied to a tribo-system in which several parameters were varied: slip, sum velocity, load, lubricant inlet temperature and viscosity - temperature index. The friction model gives the possibility to study the effect of frictional heating and/or film thickness reduction due to changes in a lubricant's inlet temperature. It was found that the frictional heating has an important effect on the friction level. As the inlet temperature increases, the oil viscosity decreases and the main effect is an increase in friction in the ML regime followed by a decreasing friction in EHL.

To include also starvation effects in the model, a film thickness correction factor is proposed (Eq. 3.44) based on the numerical results of Damiens et al. [57]. The friction model includes both frictional heating and starvation, any combination of parameters being possible.

Finally, the influence of the attack angle was introduced in the model to study its influence on the film thickness, slip and ultimately the coefficient of friction.

7.1.2 Experiments

To validate the model for the general elliptical contact situation in the presence of a lubricant, experiments were carried out in the laboratory using two different tribometers, i.e. a two disk machine and a pin-on-disk device. The model showed to be in good agreement with the measured friction values.

For a wheel - rail contact validation of the model, experiments had to be carried out in the field. For this purpose, the approach on friction measurement in railroad industry was studied and after careful consideration, the general conclusion is that none of the existing tribometers was suitable (or available) for the present research. Therefore, two train borne tribometers, referred as "Sliding Sensor" and "TriSpec", were developed and used.

The first sensor proved to be capable of detecting changes in friction level and even more, lasting effects of friction modifiers: low friction modifier (KajoBio) and high friction modifier (Sandite). It also detects changes in friction level after a number of passes. The low frequency oscillations of the rolling stock are compensated and the high frequency vibrations from the contact probe are damped, features leading to a smooth and continuous measurement up to the test velocities of 50 km/h.

A second tribometer, i.e. “TriSpec”, was developed for measuring traction curves between a measuring wheel and the top (head) of the rail. The device was mounted on a special measuring vehicle and measurements were conducted on the Dutch rail network over the entire autumn of 2008. The collected data was huge (700 GB or 175 DVDs) so the manual processing was impossible. Therefore, a code had to be written in Matlab to automate the process. The code needed approximately 200 hours to process all the data. The main result was a number of 8000 sets of outputs as described in section 5.4.6. Out of these, a number of 6172 measurement sets were chosen as valid by visually inspecting each result. If considering that all measurements were performed at 80 km/h and a cycle (Fig. 5.18) took 6 seconds, it means that approximately 800 km of track was measured.

The measurements were carried out at night-time on three different tracks within the Dutch rail network. 80% of the measured coefficient of friction lay within the interval of 0.05 - 0.2. Therefore, future coefficients of friction considered in calculations should be verified within this range. Only 34 % of the values are higher than 0.15 (the value after which the NS timetable is scheduled).

Five traction curves which are most representative were identified (Fig. 7.1) by the use of a statistical approach and their complete description is detailed in section 5.4.7.4. As an important finding it is noted that the slip where the maximum COF is reached in all classes is lower than 3%. The actual slip for the WSP (brake) system is 15%.

One particular experiment was conducted with the goal to prove that the measured values are in agreement with the friction model predictions described in Chapter 3. For that purpose, measurements were performed over a known grease used by ProRail for flange lubrication in curves. Two disk machine experiments were conducted with the same grease in order to extract its rheological properties [76]. These properties were later used in the friction model and the results were found to be in good agreement with the measured values.

The measured high friction traction curves are well described by the friction force for rolling/sliding contacts in the BL regime (Eq. 3.29). The Coulomb coefficient of friction, f_C, and the slip at the transition from elastic to plastic behaviour of the boundary layer, S_{ep}, are easily identified.

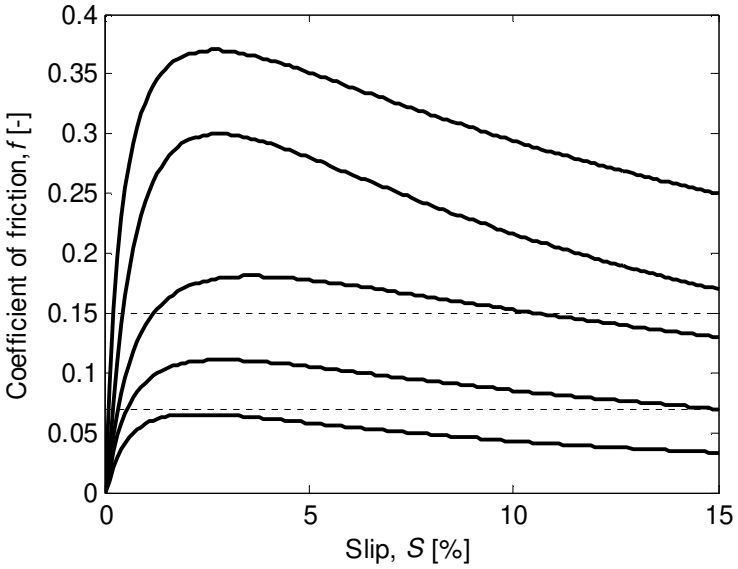

Fig. 7.1 Representative traction curves measured on tracks in the Netherlands (autumn 2008).

The measured low friction traction curves are in agreement with the shear model of Eyring (Eq. 3.23) resulting in the friction force for the EHL regime given by Eq. 3.25. The extraction of the rheological parameters is more difficult and in most of the situations, the interfacial layer causing low friction has viscoelastic behaviour. Methods for extracting the rheological parameters are presented and some examples are discussed.

Part of the measured traction curves showed a non-viscous type of behaviour for the interfacial layer, so they could not be described by the Eyring shear behaviour. For this purpose, the present friction model was extended to include also viscoelastic behaviour of interfacial/boundary layer. Predictions with the model showed good correlation with the measured traction curves, for the low friction cases (assumed to act in the EHL regime). For validation, frictional heating was taken into account.

It was also shown that the Maxwell type model, (Eq. 6.9), adapted to the existing rheological models (Eq. 6.4 through 6.8) can be used for the prediction of the coefficient of friction in the BL regime by assuming that the friction within a pair of contacting asperities is generated by shearing the boundary layer.

7.2 Discussions

This section will discuss the applicability of the developed viscoelastic model (section 6.2.3.1) to the BL regime as well as the environmental temperature influence on friction.

7.2.1 Viscoelastic model applied to the BL regime

The friction force generated in a pair of asperities in contact depends on thickness and elasticity of the boundary layer. In this subsection, the influence of these factors is studied on the Stribeck and traction curves. The general elliptical contact used in previous calculations with the inputs given in Table 3.1, is also used here. The boundary layer is assumed to shear according to the Eyring - Maxwell model and for isolating the influences of different parameters only the BL regime is considered, the shear model in EHL regime is Eyring (Eq. 3.23, without viscoelasticity). The properties of the boundary layer are given in Table 7.1.

Table 7.1: Properties of the boundary layer.

Property	Value	Unit	Description
τ_{0C}	9×10^{7}	Pa	Shear stress of the boundary layer
G_C'	1×10^{7}	Pa	Shear modulus of the boundary layer
h_C	5×10^{-8}	m	Thickness of the boundary layer

7.2.1.1 Boundary layer viscosity and thickness

In the microcontacts, the pressure may increase until 2 GPa, therefore the viscosity according to Roelands [43] and/or Barus [82] is not suitable for the present situation. Yasutomi et al. [83] proposed a model which can describe more accurately the viscosity pressure dependency. However, because the Yasutomi model has a discontinuity in the viscosity - pressure dependency and a large number of fitting parameters, it is not used here. Viscosity according to Roelands [43] will be used but limited to the value of 1×10^{6} Pas.

The thickness of the boundary layer is difficult to estimate. In the next calculations, this parameter is varied between two limits and its influence on the friction is discussed. However, as a trial, the film thickness formula for EHL contacts proposed by Nijenbanning [42] is also used here together with another approach for calculating the film thickness in micro-EHL contacts as proposed by Sloetjes [84].

7.2.1.2 Influence of the boundary layer thickness

In Fig. 7.2, several Stribeck curves are plotted, varying the thickness of the boundary layer in order to study its influence. It can be noticed that by increasing

the boundary layer thickness, the coefficient of friction in the BL regime decreases. Also, when the thicknesses according to Nijenbanning [42] and Sloetjes [84] are plotted, the Stribeck curves in these cases record an increased friction value with increasing velocity in the BL regime, while the ML regime does not change/shift in lateral direction. This effect is due to the variation of the boundary layer thickness for different pairs of contacting asperities.

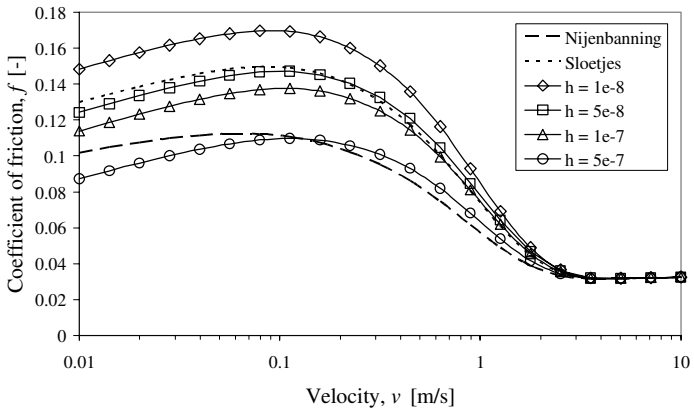

Fig. 7.2 Stribeck curve for non linear viscoelastic behaviour of the boundary layer (G_C' = 1×10^7 Pa), influence of the boundary layer thickness, h_C (m).

Another effect is the increase of the coefficient of friction in the BL regime, with increasing velocity. The increase in the coefficient of friction ends when the ML regime is reached and the number of contacting asperities starts to decrease.

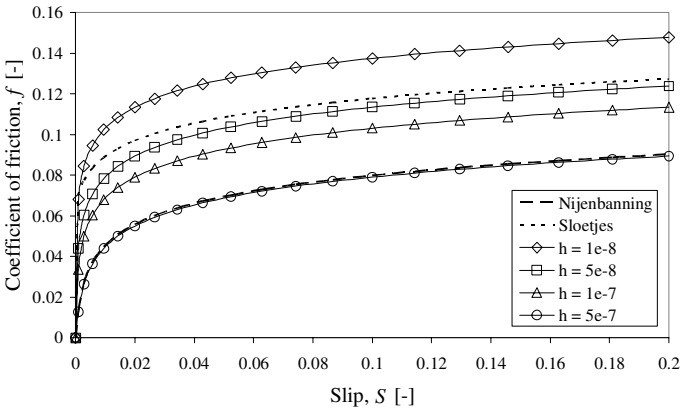

Fig. 7.3 Traction curve for non linear viscoelastic behaviour of the, boundary layer (G_C' = 1×10^7 Pa), influence of the boundary layer thickness, h_C (m).

The influence of the boundary layer thickness on the traction curve (Fig. 7.3) is obvious, with increasing the boundary layer thickness, the coefficient of friction decreases.

7.2.1.3 Influence of the shear modulus

In Fig. 7.4, several Stribeck curves are plotted, for different values of the shear modulus of the boundary layer.

Before starting to analyze the effect of the shear modulus, Eq. 6.13 shows that if the Deborah number (Eq. 6.14) decreases to zero, the viscoelastic behaviour is diminishing. So the boundary layer predominant behaviour will be a viscous one, given by the model described in Eq. 6.3. A predominant viscoelastic effect leads, in fact, to a decrease in the coefficient of friction which is visualized in Fig. 6.11. So, studying the effect of the Deborah number and in particular its dependency of the shear modulus, it is observed that with increasing the shear modulus, the viscous behaviour is less predominant and the coefficient of friction increases. This effect is shown in Fig. 7.4.

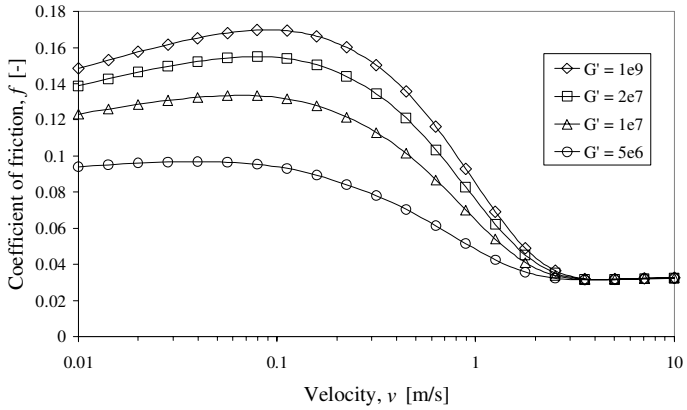

Fig. 7.4 Stribeck curve for non linear viscoelastic behaviour of the boundary layer ($h_C = 5\times10^{-8}$ m), influence of shear modulus of the boundary layer, G_C' (Pa).

The shear modulus influence on the traction curve is twofold (Fig. 7.5). Decreasing the shear modulus, first, it shifts the traction curve to the right by decreasing the slope of the curve near the pure rolling point (zero slip) and secondly, it lowers the value of the coefficient of friction at high slip values, according to the value found for the Stribeck curve for the simple sliding situation, at 200% slip. Since the slope of the curve around pure rolling point is very sensitive to different values of the shear modulus, its influence on the high slip region is clearly visible in the Stribeck curve (Fig. 7.4).

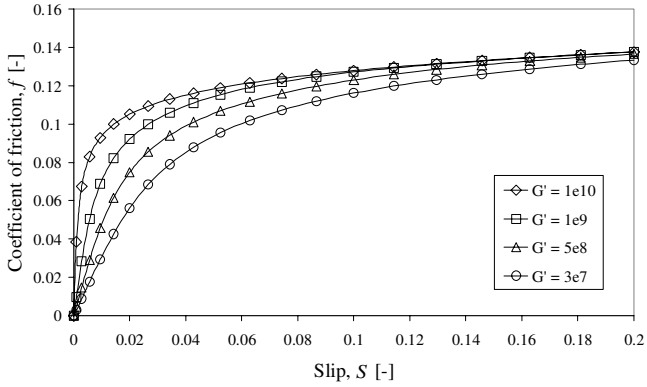

Fig. 7.5 Traction curve for non linear viscoelastic behaviour of the boundary layer ($h_C = 5\times10^{-8}$ m), influence of the shear modulus of the boundary layer, G_C' (Pa).

7.2.2 Temperature

Having the parameters of the most representative traction curve for the low friction situation (Table 6.4) and considering its viscoelastic behaviour (shear modulus, G' = 45 MPa), the effect of ambient temperature is studied in Fig. 7.6.

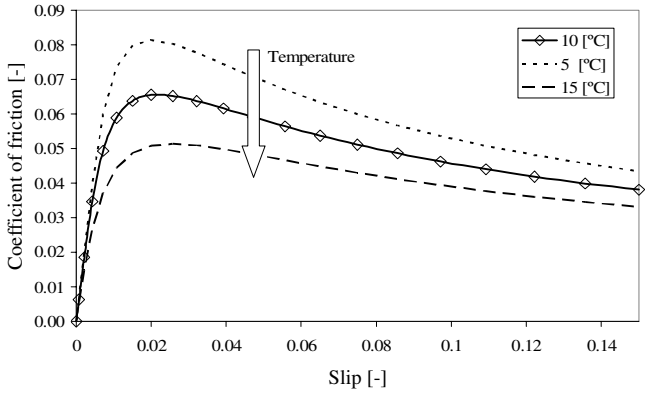

Fig. 7.6 Effect of temperature on the traction curve
(F_N = 1200 [N], v = 22 [m/s], S_0 = 1 [-], G' = 45 [MPa]).

Assuming the train is running at 22 m/s (approx. 80 km/h) over the layer causing low friction at 10 ºC, the diamond indicated line in Fig. 7.6 is obtained. If the ambient temperature would be only 5 degrees lower, the coefficient of friction would increase with approx. 25 %. If the train would pass over the same layer when the temperature outside is say 15 ºC, the friction level will drop by 21 %. In both cases, the coefficient of friction value is compared with the one at 10 ºC.

As shown, the temperature has an influence on the viscoelastic behaviour of the interfacial layer. With increases in temperature, the friction level decreases for this type of material behaviour, as discussed by Briscoe and Tabor [85]. By combining the viscoelastic behaviour of the layer and the frictional heating model of Bos and Moes [49] the friction model would be complete, covering all three lubrication regimes. This is why further research in this matter is recommended.

From the predictions using the determined rheological parameters, it was shown that the ambient temperature has a major impact on the friction level. It is more likely to encounter slippery tracks when the ambient temperature is higher. A 15 ºC autumn day would result in lower friction value compared to a 5 ºC one.

7.3 Recommendations

Based on the presented research on the low friction problem in wheel - rail contacts, a few recommendations will be given in the next subsections.

7.3.1 Theoretical

As summarized in the first two chapters, the friction between wheel and rail depends on a large number of parameters such as: train velocity, slip and attack angle between wheel and rail, contamination properties, surface roughness, wheel and rail profiles, material properties and external load. The developed microcontact and friction model applicable to the wheel - rail contact situation is highly complex and takes most of these parameters into account. Most of the situations caused by the relative position between the wheelset and the track (Fig. 2.3) are covered by approximating the non-Hertzian contact area with an equivalent elliptical contact area. There is still one situation which can influence significantly the behaviour of a train when running on slippery tracks and that one is a high lateral shift of the wheelset causing the wheel flange to have contact with the gauge side of the rail. This takes place in curves and can also happen on a straight track due to the hunting (zig-zag) movement of the train. A flange contact makes a significant angle with the horizontal plane so the spin component becomes predominant. This movement, i.e. spin, should be included in the model as it can give significant information when the train runs in curves. One may start working on the topic starting from the work of Johnson and Roberts [77].

As the friction model also includes frictional heating for the EHL component (section 3.2), the same should be conducted for the BL regime. Since the boundary layer is modelled as a viscoelastic material, the friction in the microcontacts is calculated by using one of the Maxwell shear models available. The same model of

Bos and Moes [49] for calculating the flash temperature in the macrocontact can be used also for the microcontacts when the asperities are approximated by ellipsoids.

7.3.2 Practical

From a practical point of view, there are a few quick gains and recommendations for both the Dutch operator (NSR) and the network manager (ProRail).

7.3.2.1 Braking and traction

A quick gain is based on the traction measurement performed in the rail network. From Fig. 7.1, one may see that the maximum coefficient of friction is reached at a slip value less than 5% and not at 15%, the value of which the WSP, i.e. wheel slide protection, system is working. An adjustment for that system to operate at say 5% slip would improve the braking efficiency by 30 - 40 % (Fig. 7.7).

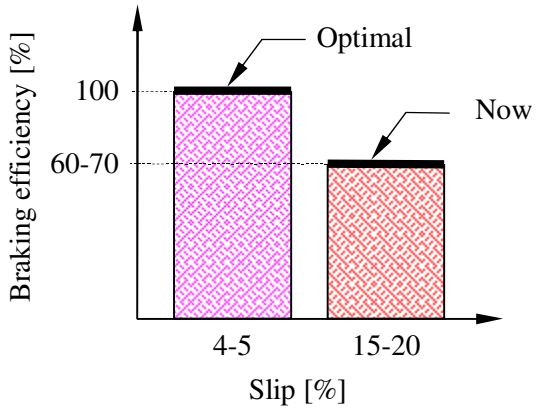

Fig. 7.7 Braking efficiency improvement.

7.3.2.2 Low friction detection

Based on the tribotester measurements, with the general results given Fig. 7.1, a low friction detection system is proposed. Since the friction level of the wheel - rail contact differs significantly at low slip values, say 1%, low friction detection is rather easy. For such purpose, a schematic representation of low friction detection as in Fig. 7.8 is proposed to be mounted on a non-driven bogie.

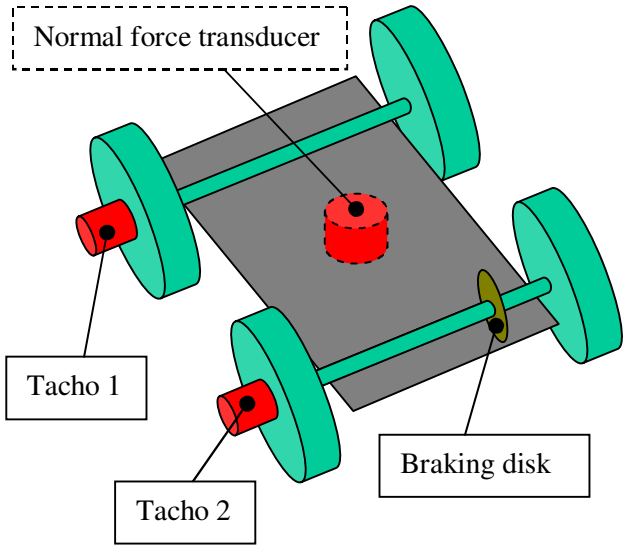

Fig. 7.8 Low friction detector on a non-driven bogie.

If, on two wheelsets, the rotational speed can be measured within acceptable limits, the 1 % slip value can be accurately detected. Choosing a non-driven bogie on any service rolling stock and mounting a force-controlled brake on one of the wheelsets, accurate low friction detection is realized. The first wheelset would record with "Tacho 1" the velocity of the train and the second wheelset, with "Tacho 2" would record its rotational speed while braking. Measurement of the braking force can be done by any available means, i.e. air pressure within the braking system, force transducer in the braking pad components chain, etc.

As a possible scenario, trains equipped with such devices would slightly brake only on the braking wheelset for a short period of time, at 1 or 2% slip, without affecting the velocity and dynamics of the train. An indicator could be positioned within the cockpit of the driver to give him or her a signal, wherever the track is, on whether it is slippery or not. Possibilities that can be taken further from this point are many: in the case of a known condition of the track, the driver can take appropriate action, so he/she will brake accordingly to the friction level of the track and he/she might also signal to the following trains what the real condition of the track is.

So, with only three relatively simple to mount measurement devices, on a non-driven bogie of any rolling stock, a low friction detection system can be easily built on each train.

7.3.2.3 Layer removal

Concerning the layer removal problem, research that focused on the frictional heating in the BL regime should be conducted further. Usually, rolling/sliding contacts should function in a safe regime (surfaces protected by a surface layer) from a wear point of view, i.e. when plotting the normal load as a function of sliding velocity the operational conditions should lie beneath the transition line (Fig. 7.9), 'safe to unprotected' (no surface layer present) sliding contact.

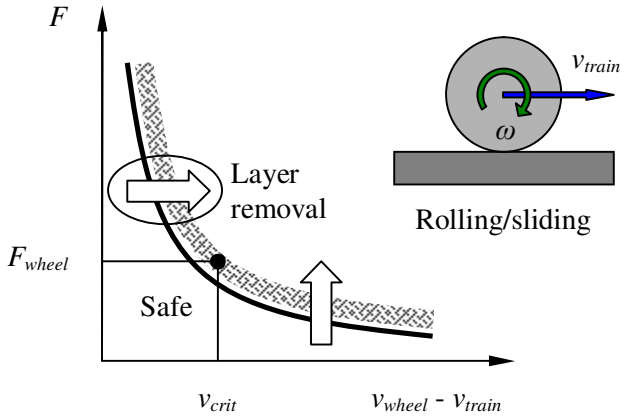

Fig. 7.9 Scheme of layer removal.

In relation to the low friction problem, this protective layer is not desirable. Changing the contact to an unsafe regime can be realized by either increasing the normal load or increasing the sliding velocity. Since the axle load on a train cannot be changed, the available method is to increase the slip value (sliding velocity) between wheel and rail. Once such critical sliding velocity of the unwanted contamination layer is determined, this layer can be thermally removed. To determine the operational conditions, i.e. load velocity combination, more field measurements should be conducted with the developed tribometer. The experiments should exclusively be oriented on high slip traction curves at low train velocity.

7.3.2.4 Correlation: low friction – Meteo data

It was shown that the environmental temperature has a significant influence on the friction between wheel and rail (section 7.2.2). More precisely, on "warm" autumn days, it is more likely that slippery tracks will be found than on "cold days". Therefore, investigations into correlating the local temperature data with slippery tracks should be done. It should be easy to implement such a prediction model since access to meteorological information is rather easy.

Appendixes

Appendix A – Separation

The adopted method to be used in this thesis for calculating the separation (input for the microcontact model) is based on material volume conservation (Eq. 3.14). However, at very high loads and/or when the microcontact is considered to be elasto-plastic by using for instance the model of Zhao [39], the film thickness can become negative, which is not realistic. In the present work, which includes elastic deformation of asperities, the separation didn't record negative values to any of the reference loads used. Anyway, for having continuation with the mentioned model of Faraon [38] and avoiding particularly situation when the separation may become negative, the truncation model of Johnson et al. [40] was implemented into the model by simply adjusting the deterministic formulation given by Eq. 3.14 with Eq. A.1:

$$h_c = \frac{1}{n}\sum_{j=1}^{n}\left\langle h_s - z_j \right\rangle \tag{A.1}$$

where $\langle\ \rangle$ are the so called "Macauley brackets" in which the negative values are neglected (formulation also used in [40]). Predictions of the model when using both methods of calculation the separation are depicted in Fig. A.

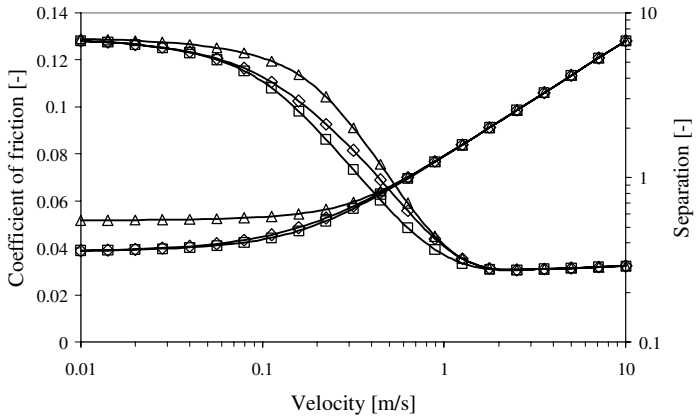

Fig. A Stribeck curves using different methods for calculating the separation (inputs given in Table 3.1): ◊ volume conservation (Eq. 3.14), Δ truncation method (Eq. A.1) and □ truncation method considering elastoplastic deformations.

As an effect when using the truncation method of Johnson, the ML regime becomes steeper which is not in agreement with experiments [38]. On the other hand, if plasticity of the asperities is included the ML becomes less steep.

Appendix B – Solution scheme for the ML friction model

Solving the ML friction model means in fact, determining the load carried by the asperities. This is done by following the solution scheme in Fig. B.

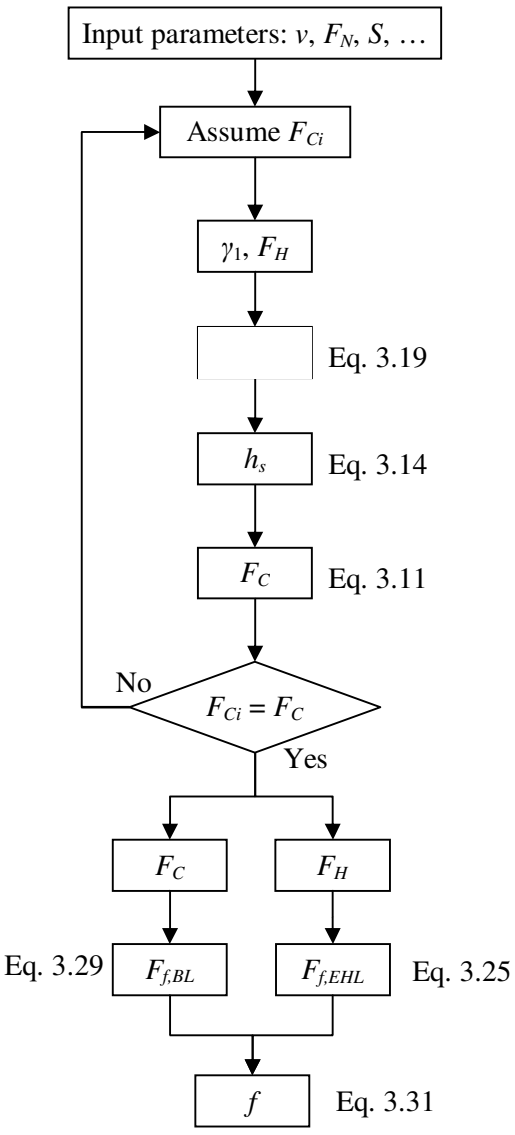

Fig. B Solution scheme for the calculation of the friction coefficient in ML regime.

Appendix C – Bos and Moes model [49]

The dimensionless flash temperature factor/number according to the model of Bos and Moes [49] reads:

$$\theta_i = \left\{ \left(\theta_s \cdot \mathbf{S}(\phi)\right)^s + \left(\frac{\theta_h}{\sqrt{2 \cdot \phi \cdot |Pe_i|}} \right)^s \right\}^{\frac{1}{s}} \tag{C.1}$$

Where, $s = 0.5 \cdot \exp(1-\phi) - 2.5$ and $\phi = b/a$ is the aspect ratio of the contact ellipse, as defined in [49].

$$\theta_h = \frac{\theta_r \cdot (1+p_e)^2 + \theta_c \cdot (1-p_e)^2}{2 \cdot (1+p_e^{\,2})} \tag{C.2}$$

is the flash temperature solution for high Peclet numbers. In Eq. C.2, $p_e = Pe_2/Pe_1$ is the Peclet number ratio where $Pe_i = (a \cdot v_i)/(2 \cdot k_i)$ and $k_i = K_i/(\rho_i \cdot c_i)$ is the diffusivity, ρ_i the density and c_i the specific heat at constant pressure of body *i*, *i* = 1,2, surface 1 and 2 respectively.

Further, the shape factor in Eq. A1 is given by:

$$\mathbf{S}(\phi) = \frac{2 \cdot \sqrt{\phi}}{1+\phi} \cdot \frac{2}{\pi} \cdot \mathbf{K}\left(\frac{|1-\phi|}{1+\phi} \right) \tag{C.3}$$

With **K** the elliptical integral of the second kind:

$$\mathbf{K}(m) = \int_0^{\frac{\pi}{2}} \frac{d\varphi}{\sqrt{1 - m^2 \cdot \sin^2(\varphi)}} \tag{C.4}$$

Or the numerical approximation according to [86]:

$$\mathbf{K}(m) = \frac{\pi}{2} \cdot (1-m) \cdot \left[1 + \frac{2 \cdot m}{\pi \cdot (1-m)} - \frac{1}{8} \cdot \ln(1-m) \right] \tag{C.5}$$

Temperature numbers in Eq. C.1 and C.2, are as for stationary solids, θ_s^{kl}, for velocities in the same direction, θ_r^{kl} and for velocities in opposite directions, θ_c^{kl}. Where, the superscript "k" is for **u**niform or semi-**e**llipsoidal heat source and "l" for **a**verage or **m**aximum temperature rise.

Table C.1: Temperature numbers.

Uniform heat supply ($k = u$)	
Average ($l = a$)	Maximum ($l = m$)
$\theta_s^{ua} = \frac{8}{3\pi^2} = 0.27$	$\theta_s^{um} = \frac{1}{\pi} = 0.31831$
$\theta_r^{ua} = \frac{32\sqrt{2} \cdot \Gamma\left(\frac{3}{4}\right)}{5\pi^2} \Gamma\left(\frac{1}{4}\right) = 0.31$	$\theta_r^{um} = \frac{2\sqrt{2}}{\pi\sqrt{\pi}} = 0.508$
$\theta_c^{ua} = \frac{8\sqrt{2}}{5\pi\sqrt{\pi}} = 0.4064$	$\theta_r^{um} = \frac{2\sqrt{2}}{\pi\sqrt{\pi}} = 0.508$
Semi-ellipsoidal heat supply ($k = e$)	
Average ($l = a$)	Maximum ($l = m$)
$\theta_s^{ea} = \frac{9}{32} = 0.28125$	$\theta_s^{em} = \frac{3}{8} = 0.375$
$\theta_r^{ea} = 0.322991$	$\theta_r^{em} = 0.589487$
$\theta_c^{ea} = 0.437504$	$\theta_c^{em} = 0.700792$

Appendix D – Solution scheme of ML model with frictional heating

Once the load carried by the lubricant is determined, the friction force generated by shearing the lubricant is calculated as shown in Fig. D.

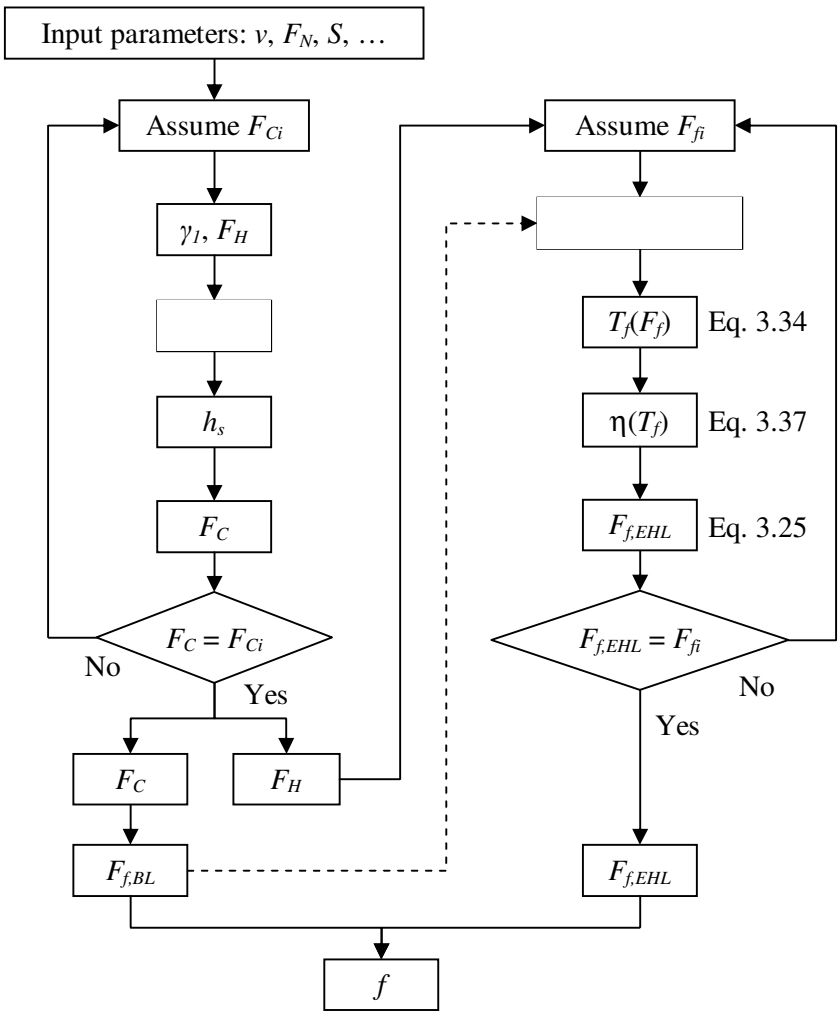

Fig. D Solution scheme for the calculation of the friction coefficient in ML regime including frictional heating of the lubricant.

The second part of the scheme (from the load carried by the lubricant, F_H and further) presents the method of solving the system of two equations (Eq. 3.34 and 3.25) for the unknowns T_f and $F_{f,EHL}$.

Appendix E – Hertz theory

For the general Hertzian problem of ellipsoid solids in contact, the required inputs are: R_{1x}, R_{1y}, R_{2x}, R_{2y}, the attack angle, Φ, normal load F_N and the combined elasticity modulus, E'.

(a) Simplified Hertz theory for elliptical contact:

In the case that the attack angle, $\Phi = 0$, the semi-axes of the contact ellipse are:

$$a = a^* \left(\frac{3F_N R}{E'} \right)^{\frac{1}{3}} \tag{E.1}$$

$$b = b^* \left(\frac{3F_N R}{E'} \right)^{\frac{1}{3}} \tag{E.2}$$

Normal approach:

$$\delta = \delta^* \left(\frac{9F_N{}^2}{8R(E')^2} \right)^{\frac{1}{3}} \tag{E.3}$$

Mean contact pressure:

$$p_m = \frac{F_N}{\pi ab} \tag{E.4}$$

Maximum Hertizan pressure:

$$p_0 = \frac{3}{2} p_m \tag{E.5}$$

Where,

$$\frac{1}{R} = \frac{1}{R_{1x}} + \frac{1}{R_{1y}} + \frac{1}{R_{2x}} + \frac{1}{R_{2y}} \tag{E.6}$$

$$a^* \approx \kappa^{\frac{1}{3}} \left[\frac{2}{\pi} E(m) \right]^{\frac{1}{3}} \tag{E.7}$$

$$b^* \approx \kappa^{\frac{-2}{3}} \left[\frac{2}{\pi} E(m) \right]^{\frac{1}{3}} \tag{E.8}$$

$$\delta^* \approx \kappa^{\frac{2}{3}} \left[\frac{2}{\pi} E(m) \right]^{\frac{-1}{3}} \left[\frac{2}{\pi} K(m) \right] \tag{E.9}$$

With the elliptical integrals in the approximate form proposed by Reussner [86]:

$$E(m) \approx \frac{\pi}{2}(1-m)\left[1+\frac{2m}{\pi(1-m)}-\frac{1}{8}\ln(1-m)\right] \tag{E.10}$$

$$K(m) \approx \frac{\pi}{2}(1-m)\left[1+\frac{2m}{\pi(1-m)}\ln\left(\frac{4}{\sqrt{1-m}}\right)-\frac{3}{8}\ln(1-m)\right] \tag{E.11}$$

and,

$$\kappa \approx \left[1+\sqrt{\frac{\ln(16/\vartheta)}{2\vartheta}}-\sqrt{\ln(4)}+0.16\ \ln(\vartheta)\right]^{-1} \tag{E.12}$$

$$m=\sqrt{1-\kappa^2} \quad \text{and} \quad \kappa=\frac{a}{b} \quad \text{for} \quad a<b \tag{E.13}$$

$$\vartheta=\frac{R_x}{R_y} \quad \text{for} \quad 0<\vartheta\le 1 \tag{E.14}$$

Where the principal combined radii of curvature, R_x and R_y, are given by:

$$\frac{1}{R_x}=\frac{1}{R_{1x}}+\frac{1}{R_{2x}} \quad \text{and} \quad \frac{1}{R_y}=\frac{1}{R_{1y}}+\frac{1}{R_{2y}} \tag{E.15}$$

(a) General Hertz theory for elliptical contact:

If the two contacting bodies make an angle, $\Phi \neq 0$, the principal radii of curvature in Eq. E.15 become:

$$\frac{1}{R_x}=\frac{1}{2}\sum\rho-\sqrt{\Delta} \ \text{and} \ \frac{1}{R_y}=\frac{1}{2}\sum\rho+\sqrt{\Delta} \tag{E.16}$$

and,

$$\sum\rho=\frac{1}{R_{1x}}+\frac{1}{R_{1y}}+\frac{1}{R_{2x}}+\frac{1}{R_{2y}} \tag{E.17}$$

$$\Delta=G_1^{\,2}+G_2^{\,2}+2G_1G_2\cos(4\varphi) \tag{E.18}$$

$$G_1=\frac{1}{2}\left(\frac{1}{R_{1x}}-\frac{1}{R_{1y}}\right) \quad \text{and} \quad G_2=\frac{1}{2}\left(\frac{1}{R_{2x}}-\frac{1}{R_{2y}}\right) \tag{E.19}$$

Here, the attack angle is redefined as:

$$2\varphi=\Phi \tag{E.20}$$

The angle made by the contact area with the rolling direction is given by:

$$\sin(2\beta) = -\frac{G_1 - G_2}{\sqrt{\Delta}}\sin(2\varphi) \quad \text{or} \quad \cos(2\beta) = \frac{G_1 + G_2}{\sqrt{\Delta}}\cos(2\varphi) \tag{E.21}$$

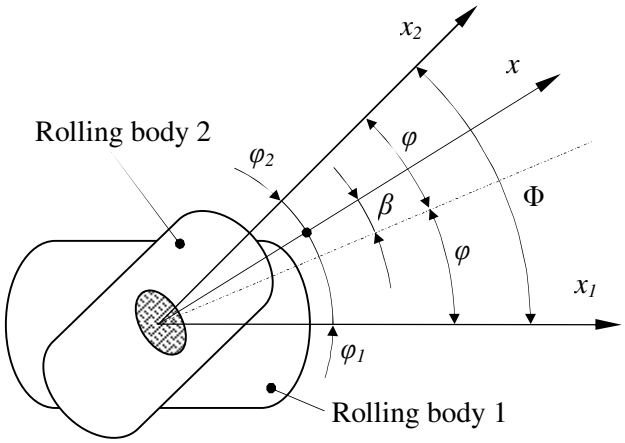

Fig. E Definition of angles at the oblique Hertzian contact.

The angle between the principal direction of the contact ellipse and the principal axis of the first rolling body, φ_1, is:

$$\varphi_1 = \varphi + \beta \tag{E.22}$$

And the angle between the contact area and the second body, φ_2, is:

$$\varphi_2 = \varphi - \beta \tag{E.23}$$

The above approximations for finding the shape of the contact ellipse quantified by the eccentricity, κ, as well as the approximations of Reussner [86] for the elliptical integrals, are very precise.

From the system of equations of Hertz, the next equation is derived [9]:

$$\vartheta = \frac{K(m) - E(m)}{\frac{E(m)}{1-m^2} - K(m)} \tag{E.24}$$

Where, the ellipticity integrals are as given in Eq. E.10 and E.11.

Eq. E.24 was solved numerically for finding the eccentricity, κ. Further, the semi axes of the contact ellipse as well as the approach were determined using Eq. E.1, E.2 and E.3.

Appendix F – Wheel and rail profiles

The standard UIC60 rail profile is defined by arcs of circles and it is geometrically given as a technical drawing. For keeping the same format as for the wheel, the circles are approximated by equations. Since the (not inclined) rail profile is symmetrical, only half of it will be described in four sections indexed as $i = [A, B, C, D]$ [87].

$$z(y_A) = -a_A + \sqrt{b_A{}^2 - y_A{}^2} \tag{F.1}$$

$$z(y_B) = -a_B + \sqrt{b_B{}^2 - (y_B - c_B)^2} \tag{F.2}$$

$$z(y_D) = -a_C + \sqrt{b_C{}^2 - (y_C - c_C)^2} \tag{F.3}$$

$$z(y_E) = a_D - b_D y_D \tag{F.4}$$

Where $y_i \in [y_{\min i}, y_{\max i}]$ is the considered segment.

Table F.1: Polynomial factors and sections for the standard UIC60 rail profile.

	A	*B*	*C*	*D*
a	300	80.1	14.91	705.74
b	300	80	13	20
c	–	7.7	23.02	–
y_{min}	0	10.5	26.0	36
y_{max}	10.5	26.0	36	37.16

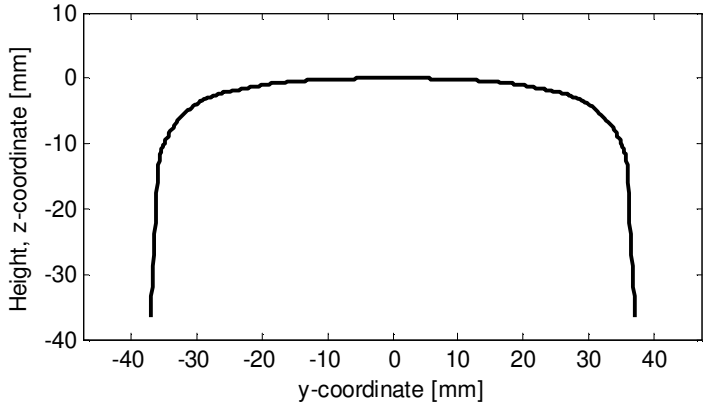

Fig. F.1 Standard UIC60 rail profile.

The standard S1002 wheel profile is defined by polynomials and divided in eight sections indexed as $i = [A, B, C, D, E, F, G, H]$ [87].

$$z(y_A) = a_A - b_A y_A \tag{F.5}$$

$$z(y_B) = a_B - b_B y_B + c_B y_B^{\,2} - d_B y_B^{\,3} + e_B y_B^{\,4} - f_B y_B^{\,5} + g_B y_B^{\,6} - h_B y_B^{\,7} + i_B y_B^{\,8} \tag{F.6}$$

$$z(y_C) = -a_C - b_C y_C - c_C y_C^{\,2} - d_C y_C^{\,3} - e_C y_C^{\,4} - f_C y_C^{\,5} - g_C y_C^{\,6} - h_C y_C^{\,7} \tag{F.7}$$

$$z(y_D) = a_D - \sqrt{b_D^{\,2} - (y_D + c_D)^2} \tag{F.8}$$

$$z(y_E) = -a_E - b_D y_D \tag{F.9}$$

$$z(y_F) = a_F + \sqrt{b_F^{\,2} - (y_F + c_F)^2} \tag{F.10}$$

$$z(y_G) = a_G + \sqrt{b_G^{\,2} - (y_G + c_G)^2} \tag{F.11}$$

$$z(y_H) = a_H + \sqrt{b_H^{\,2} - (y_H + c_H)^2} \tag{F.12}$$

Where $y_i \in [y_{\min i}, y_{\max i}]$ is the considered segment.

Table F.2: Polynomial factors and sections for the standard S1002 wheel profile.

	A	*B*	*C*	*D*
a	1.364	0.0	4.320×10^{3}	16.446
b	0.067	3.359×10^{-2}	1.038×10^{3}	13
c	–	1.566×10^{-3}	1.066×10^{2}	26.211
d	–	2.810×10^{-5}	6.051	–
e	–	5.844×10^{-8}	2.054×10^{-1}	–
f	–	1.562×10^{-8}	4.170×10-^{3}	–
g	–	5.309×10^{-15}	4.687×10^{-5}	–
h	–	5.958×10^{-12}	2.253×10^{-7}	–
i	–	2.647×10^{-13}	–	–
y_{min}	32.16	-26	-35	-38.427
y_{max}	60	32.16	-26	-35

	E	*F*	*G*	*H*
a	93.577	8.835	16	9.519
b	2.747	20	12	20.5
c	–	58.558	55	49.5
y_{min}	-39.764	-49.663	-62.765	-70
y_{max}	-38.427	-39.764	-49.663	-62.765

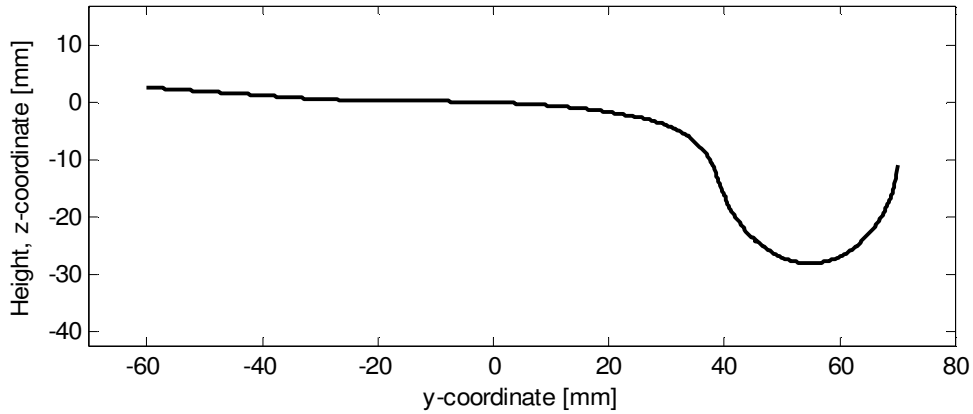

Fig. F.2 Standard S1002 wheel profile.

The wheelset and track gauges are shown schematically in Fig. F.3. The track gauge is measured between the points on the rail profile located inside the track at a distance of 14.1 mm from the common tangent to the profiles of both rails. Assuming the track is in a straight line, the aforementioned tangent will be horizontal. The wheel radius is measured at the mean wheel circle, usually at 70 mm from the back of the wheel. The inclination of the rail is usually 1/40 or 1/20.

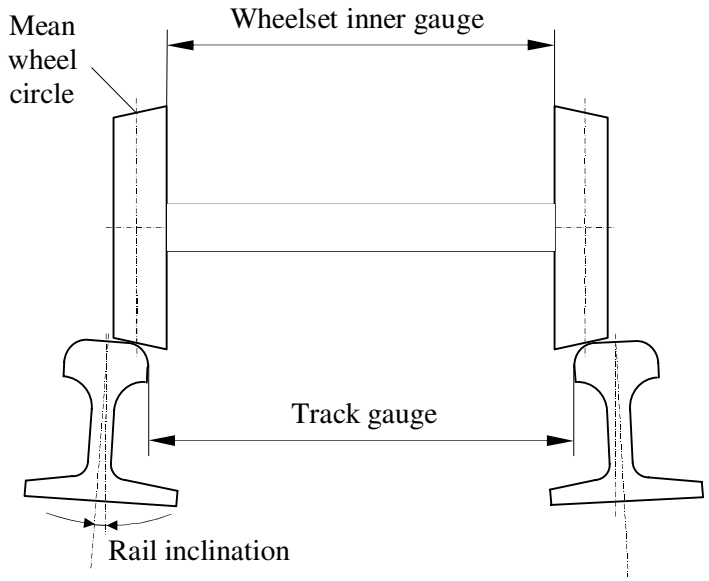

Fig. F.3 Wheelset and track main dimensions.

Appendix G – Numerical solution for Maxwell models

The Ordinary Differential Equation (ODE) given by Eq. 6.16 can be solved by several integration techniques, most of them are described in [88]. The most appropriate numerical techniques available for the present calculation are: Euler, Runge - Kutta and Bulirsch - Stoer using Richardson extrapolation.

When dealing with increased accuracy and computation speed, the most common method is the 4^{th} order Runge – Kutta (RK4) method, which estimates the solution at a given point. Using adaptive step size in combination with the RK4 increases also the accuracy and the computation speed. The Bulirsch – Stoer method in combination with Richardson extrapolation for adapting the step size (BSSTEP) gives a more accurate and faster solution for smooth functions only. Because the shear stress varies smoothly inside the contact area, the method was also considered here.

Using the exact analytical solution for the Maxwell model based on Newtonian lubricant behaviour (Appendix H), a comparison between the above methods is shown in Fig. G by plotting the percentage of error.

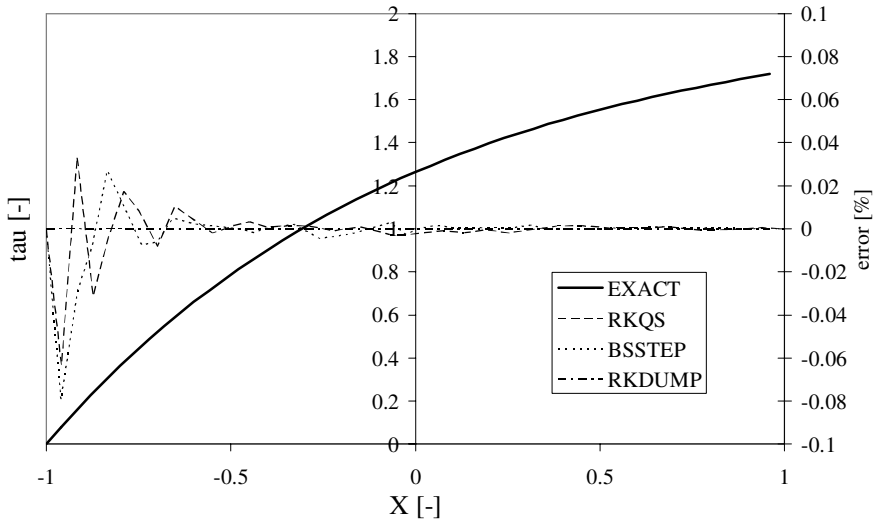

Fig. G Comparison between the numerical drivers.

In Fig. G, the three methods for solving an ODE are discussed. The solutions and the percentage error when compared with the exact analytical solution are shown. Abbreviations of the insert are described in Table G.

Table G: ODE algorithm description.

RKQS	Fourth order Runge – Kutta with adaptive step size
BSSTEP	Bulirsch – Stoer method with adaptive step size using Richardson extrapolation
RKDUMP	Fourth order Runge – Kutta with fixed step size (tabulates the results)

For all algorithms, the maximum error was set to 10^{-9} and, for the variable step size drivers only, the minimum step size was set to 10^{-5}.

All the presented drivers perform the calculation well. The errors are very low, also for the first steps of the methods using adaptive step size, and the time computation is very good. So the ultimate factor which made a differentiation possible between the three methods was the simplicity of calculating the future parameter in the model. And that is the friction force which will be determined by integrating the calculated shear stress over the contact area. When using an adaptive step size, the next integration is difficult because a new interpolation is necessary between the solutions found (for example a Spline interpolation) and further the values necessary for calculating the integrant can be tabulated. For the RKDUMP algorithm, these intermediate steps can be skipped, because the tabulation is dictated at the beginning of the ODE integration.

As a note, the Runge – Kutta with adaptive step size and Bulirsch – Stoer methods remain the methods with the highest performance in ODE integration. It is just the shape of the presented functions (shear models) which makes the usage of the adaptive step size useless. Therefore, the method chosen for solving the Maxwell based shear models is the 4^{th} order Runge – Kutta method with fixed step size (RKDUMP algorithm).

Appendix H – Analytical solution for Maxwell models

Maxwell based on Newtonian model (Eq. 6.4)

Johnson and Roberts [77] presented an analytical solution for calculating the shear stress over the contact area for the Maxwell Newtonian based model. In order to follow the integration procedure easily, the model is presented in dimensional form:

$$\dot{\gamma} = \begin{cases} \dfrac{1}{G'}\dfrac{d\tau}{dt} + \dfrac{\tau}{\eta} & \text{for} \quad \tau \le \tau_L \\ \dfrac{\tau_L}{\eta} & \text{for} \quad \tau > \tau_L \end{cases} \tag{H.1}$$

The analytical (general) solution for Eq. H.1 ($\tau \le \tau_L$) is given by:

$$\tau(t) = \frac{\int \exp\left(\dfrac{G'\cdot t}{\eta}\right)\cdot G'\cdot\dot{\gamma}\, dt + c_t}{\exp\left(\dfrac{G'\cdot t}{\eta}\right)} = \eta\cdot\dot{\gamma} + \frac{c_t}{\exp\left(\dfrac{G'\cdot t}{\eta}\right)} \tag{H.2}$$

Considering the shear stress at time $t = 0$, null, and using this as boundary condition, the integration constant becomes $c_t = -\eta\cdot\dot{\gamma}$, so the solution for the shear stress as a function of time is:

$$\tau(t) = \eta\cdot\dot{\gamma}\left[1 - \exp\left(-\frac{G'\cdot t}{\eta}\right)\right] \tag{H.3}$$

Now, changing the time variable to the contact ellipse coordinates (Fig. 6.10) by using Eq. 6.10, 6.11 and 6.12, the shear stress in Eq. H.3 becomes:

$$\tau(x, y) = \eta\cdot\dot{\gamma}\left[1 - \exp\left(\frac{x - x^+}{a\cdot D}\right)\right] \tag{H.4}$$

Or in dimensionless form:

$$\bar{\tau}(X, Y) = \xi\cdot\left[1 - \exp\left(\frac{X - X^+}{D}\right)\right] \tag{H.5}$$

With x^+ given by Eq. 6.12 and X^+ by Eq. 6.15.

Eq. H.5 gives the value of the shear stress, in a (X, Y) point inside the contact area of a rolling to sliding elliptical contact. A graphical representation of this distribution is presented in Fig. H.

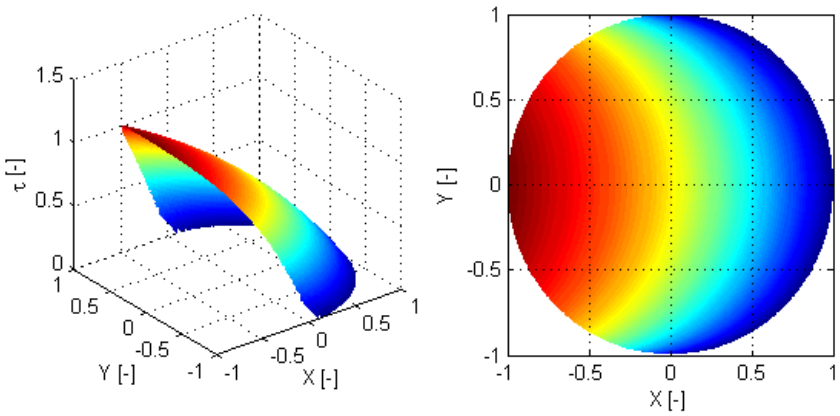

Fig. H Shear stress distribution within an elliptical contact.

Maxwell based on Eyring model (Eq. 6.5)

For the same considerations as in the previous analytical solution, the governing equation for such a model is given by:

$$\dot{\gamma} = \frac{1}{G'}\frac{d\tau}{dt} + \frac{\tau_0}{\eta}\cdot\sinh\frac{\tau}{\tau_0} \tag{H.6}$$

Where, $\dot{\gamma}$ is the shear rate given by Eq. 3.22 and τ_0 is the Eyring shear stress. Eq. H.6 is a first order differential equation and written in this form is a non exact function. In order to make the function exact, it must be rearranged as follows:

$$\frac{d\tau}{G'\cdot\frac{\tau_0}{\eta}\cdot\sinh\left(\frac{\tau}{\tau_0}\right) - G'\cdot\dot{\gamma}} + dt = 0 \tag{H.7}$$

The general solution for this equation is:

$$t - \frac{2\cdot\eta\cdot\tau_0}{G'\cdot\sqrt{\tau_0^{\,2}+\eta^2\cdot\dot{\gamma}^2}}\cdot\operatorname{atanh}\left[\frac{\tau_0+\eta\cdot\dot{\gamma}\tanh\left(\frac{\tau}{2\cdot\tau_0}\right)}{\sqrt{\tau_0^{\,2}+\eta^2\cdot\dot{\gamma}^2}}\right] = c_t \tag{H.8}$$

Using the boundary condition $\tau(0)=0$, the integration constant, c_t, is found to be:

$$c_t = -\frac{2\cdot\eta\cdot\tau_0}{G'\cdot\sqrt{\tau_0{}^2+\eta^2\cdot\dot{\gamma}^2}}\cdot \operatorname{atanh}\left(\frac{\tau_0}{\sqrt{\tau_0{}^2+\eta^2\cdot\dot{\gamma}^2}}\right) \tag{H.9}$$

So, the solution of Eq. H.7 is given by:

$$t = \frac{2\eta}{G'}\frac{1}{\sqrt{1+\xi^2}}\left\{\operatorname{atanh}\left[\frac{1}{\sqrt{1+\xi^2}}+\frac{\xi}{\sqrt{1+\xi^2}}\tanh\left(\frac{\bar{\tau}}{2}\right)\right]-\operatorname{atanh}\left(\frac{1}{\sqrt{1+\xi^2}}\right)\right\} \tag{H.10}$$

Where $\bar{\tau}$ is given by Eq. 6.1 and ξ by Eq. 6.2.

Considering the steady flow situation and the same rationing as presented in section 6.2.3.1, the shear stress variation over the elliptical domain is in its dimensionless form given by:

$$\bar{\tau}(X,Y) = 2\cdot\operatorname{atanh}\left\{\frac{\xi\cdot\tanh\left[\frac{\sqrt{1+\xi^2}}{2\cdot D}\left(X^+-X\right)\right]}{\sqrt{1+\xi^2}+\tanh\left[\frac{\sqrt{1+\xi^2}}{2\cdot D}\left(X^+-X\right)\right]}\right\} \tag{H.11}$$

Where $\bar{\tau}$ is given by Eq. 6.1, ξ by Eq. 6.2, D by Eq. 6.14 and X, X^+ by Eq. 6.15.

Appendix I – Friction generated by shearing a viscoelastic layer

The analytical result of the integration of the ordinary differential equation, given by Eq. H.4 can be partially solved analytical, as follows:

$$F_f = 2\cdot\eta\cdot\dot{\gamma}\int_0^b\int_{-x^+}^{x^+}\left\{1-\exp\left[\frac{1}{D}\cdot\left(\frac{x}{a}-\sqrt{1-\frac{y^2}{b^2}}\right)\right]\right\}\cdot dx\cdot dy \tag{I.1}$$

Further, after first integration:

$$F_f = 2\eta\dot{\gamma}\int_0^b\left[2a\sqrt{1-\frac{y^2}{b^2}}-aD+aD\cdot\exp\left(-\frac{2}{D}\sqrt{1-\frac{y^2}{b^2}}\right)\right]dy \tag{I.2}$$

Normalizing y by $Y=\frac{y}{b}\in[0,1]$, then $dy = b\cdot dY$ and the friction force can be written:

$$F_f = 2\cdot\eta\cdot\dot{\gamma}\cdot b\cdot\left[\int_0^1 2a\sqrt{1-Y^2}\,dY-\int_0^1 aD\cdot dY+\int_0^1 aD\cdot\exp\left(-\frac{2}{D}\sqrt{1-Y^2}\right)dY\right] \tag{I.3}$$

Solving the first two integrants, the final formulation of the friction force is given by:

$$F_f = 2\cdot\eta\cdot\dot{\gamma}\cdot a\cdot b\cdot\left[\frac{\pi}{2}-D+D\int_0^1\exp\left(-\frac{2}{D}\sqrt{1-Y^2}\right)dY\right] \tag{I.4}$$

In order to have a good formulation of the friction force, the integrant which couldn't be solved analytically, will be solved numerically and then an equation will be derived by using a fitting technique. Noting that the integrant result will be only a function of the Deborah number, D:

$$f(D)=\int_0^1\exp\left(-\frac{2}{D}\cdot\sqrt{1-Y^2}\right)\cdot dY \tag{I.5}$$

After solving this numerically, a form was determined by using a fitting technique:

$$f(D)=\begin{cases}a^{\diamond}\cdot\left\{1-\exp\left[-\left(b^{\diamond}\cdot\left(D-c^{\diamond}\right)\right)^{d^{\diamond}}\right]\right\} & \text{for}\quad D\in[0,1]\\ g^{\diamond\frac{1}{D}} & \text{for}\quad D\in[1,\infty]\end{cases} \tag{I.6}$$

The parameters in Eq. I.6 are: $a^{\diamond}=0.39$, $b^{\diamond}=0.978$, $c^{\diamond}=0.021$, $d^{\diamond}=2.076$ and $g^{\diamond}=0.231$.

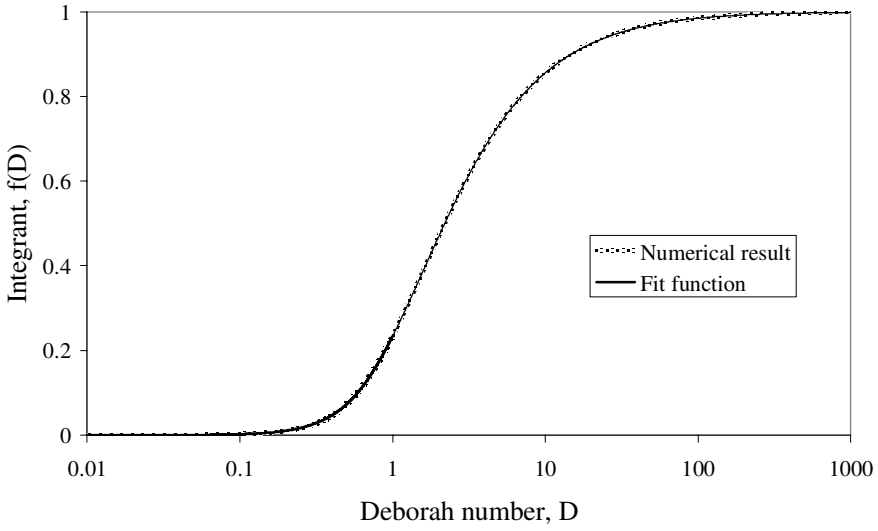

Fig. I Fitted curve after numerical calculation.

A comparison between numerical calculation of the integral (Eq. I.5) and the fitted function (Eq. I.6) is presented in Fig. I. It can be noticed that the numerical result and the fitted one are in good agreement, even on a logarithmic scale. The friction force becomes:

$$F_f = \begin{cases} 2 \cdot \eta \cdot \dot{\gamma} \cdot a \cdot b \cdot \left[\frac{\pi}{2} - D + a^{\diamond} D \left\{ 1 - \exp\left[- \left(b^{\diamond} \left(D - c^{\diamond} \right) \right)^{d^{\diamond}} \right] \right\} \right] & \text{for} \quad 0 \le D \le 1 \\ 2 \cdot \eta \cdot \dot{\gamma} \cdot a \cdot b \cdot \left[\frac{\pi}{2} - D + D \cdot g^{\diamond \frac{1}{D}} \right] & \text{for} \quad 1 \le D \le \infty \end{cases} \tag{I.7}$$

With $a^{\diamond}$, $b^{\diamond}$, $c^{\diamond}$, $d^{\diamond}$ and $g^{\diamond}$ are as given before.

Appendix J – Rheology (elasticity modulus, *G'*)

The elasticity modulus, *G*, is determined assuming viscoelastic behaviour of the interfacial layer in the full film lubrication regime, the procedure is described in detail in [81] and is summarized below. The governing equation for a viscoelastic Eyring based model is Eq. H.6. Making the approximation valid at low slip, that:

$$\frac{\tau_0}{\eta}\cdot\sinh\frac{\tau}{\tau_0}\approx\frac{\tau}{\eta} \tag{J.1}$$

Eq. H.6 becomes:

$$\dot{\gamma}=\frac{1}{G'}\frac{d\tau}{dt}+\frac{\tau}{\eta} \tag{J.2}$$

Integrating with respect to the shear stress, τ, next solution is found:

$$\tau=\eta\cdot\dot{\gamma}\left[1-\exp\left(-\frac{t}{t_r}\right)\right] \tag{J.3}$$

Where $t_r=\eta/G'$ is called relaxation time and is a few orders higher than the transit time $t=2\cdot a/U$, $U=v^+/2$ being the mean rolling velocity. Therefore, $t/t_r<<1$, so the shear stress can be written as $\tau=f\cdot p_m=G'\cdot t\cdot\dot{\gamma}$. Further, *G'* is found to be:

$$G'=\frac{p_m\cdot h\cdot f}{t\cdot U}=\frac{p_m\cdot h}{2\cdot a}tg(\alpha_0) \tag{J.4}$$

Where, $tg(\alpha_0)$ is the slope of the traction curve (Fig. 6.5 left) at zero slip, which for the considered interfacial layer is taken from Table 5.4.

References

[1] AWG Adhesion Working Group (2009), "Managing low adhesion", 4th Ed., www.awg-rail.co.uk.

[2] Fulford, C. R. (2004) "Review of low adhesion research", report published by the Rail Safety and Standards Board (RSSB), UK.

[3] Vasic, G., Franklin, F. and Kapoor, A. (2003), "New Rail Materials and Coatings", University of Sheffield, UK, RRUK Report A2/1, (prepared for RSSB).

[4] Cooper, P.R. and McEwen, I.J. (1976), "The development of Sandite – a liquid-sand adhesion improver", BR Research Report Ref: TM-TRIB-14(A).

[5] Kalousek, J., Hou, K., Magel, E. and Chiddick, K. (1996), "The benefits of friction management: a third body approach", Proceedings of the World Congress on Railway Research Conference, Colorado Springs, 461-468.

[6] Eadie, D.T., Santoro, M. and Powell, W. (2003), "Local control of noise and vibration with KELTRACK™ friction modifier and Protector® trackside application: an integrated solution", Journal of Sound and Vibration, 267, 3, 761-772.

[7] Snyder, T., Stone, D.H. and Kristan, J. (2003), "Wheel flat and out-of round formation and growth", Proceedings of the IEEE/ASME, 143-148.

[8] Carter, F.W. (1926), "On the action of a locomotive driving wheel", Proc. R. Soc., London, Series A, 151-157.

[9] Johnson, K.L. (1985), Contact mechanics, Cambridge University Press.

[10] Haines, D.J. and Ollerton, E. (1963), "Contact stress distributions on elliptical contact surfaces subjected to radial and tangential forces", Proc. Inst. Mech. Eng. 177, 95-104.

[11] Vermeulen, J. and Johnson, K.L. (1964), "Contact of nonspherical elastic bodies transmitting tangential forces", J. of App. Mech. 31, 338-340.

[12] Kalker, J.J. (1967), "On the rolling contact of two elastic bodies in the presence of dry friction", Ph.D. Thesis, TU Delft, Delft, The Netherlands.

[13] Kalker, J.J. (1990), "Three dimensional elastic bodies in rolling contact", Kluwer Academic Publishers, Dortrecht E.A.

[14] Kalker, J.J. (1991), "Wheel–rail rolling contact", Wear 144, 243-261.

[15] Damme, S., Nackenhorst, U., Wetzel, A. and Zastrau, B. (2002), "On the Numerical Analysis of the Wheel - Rail System in Rolling Contact", DFG Colloquium „System dynamics and long-term behaviour of vehicle, track and subgrade", Stuttgart, Germany, 13-15.

[16] Knothe, K., Wille, R. and Zastrau, W. (2001), “Advanced Contact Mechanics - Road and Rail”, Vehicle System Dynamics, 25, 4-5, 361-407, part: “Wheel-rail contact”, 379-397.

[17] Piotrowski, J. and Chollet, H. (2005), “Wheel-rail contact models for vehicle system dynamics including multi-point contact”, Vehicle System Dynamics, 35, 4, 361-407.

[18] Cretu, S. (2007), “The influence of roughness on pressure distribution and stress state of concentrated contacts subjected to normal loads”, Bul. Inst. Polit. Iasi, XLXIII (LVII), 1-2, s. Constructii de masini, 1-12.

[19] Pascal, J.P. and Sauvage, G. (1993), “The available methods to calculate the wheel/rail forces in non-Hertzian contact patches and rail damaging”, Vehicle System Dynamics, 22, 3-4, 263-275.

[20] Pascal, J.P. and Sauvage, G. (1991), “New method for reducing the multi-contact wheel/rail problem to one equivalent rigid contact patch”, Vehicle System Dynamics, 20, 1, 475-489.

[21] Pascal, J.P. (1993), “About multi Hertzian contact hypothesis and equivalent conicity in the case of S1002 and UIC60 analytical wheel/rail profiles”, Vehicle System Dynamics, 22, 2, 57-78.

[22] Arnold, M. and Netter, H. (1998), “Approximation of contact geometry in the dynamical simulation of wheel-rail”, Mathematical and Computer Modelling of Dynamical Systems, 4, 2, 162-184.

[23] Ayasse, J.B. and Chollet, H. (2005), “Determination of the wheel rail contact patch for semi-Hertzian conditions”, Vehicle System Dynamics, 43, 3, 159-170.

[24] Kalker, J.J. (1966), "Rolling with slip and spin in the presence of dry friction", Wear, 9, 20-38.

[25] Popov, V.L., Psakhie, S.G., Shilko, E.V. et al. (2002), “Friction coefficient in rail-wheel contacts as a function of material and loading parameters”, Physical Mesomechanics 5, 3, 17-24.

[26] Bucher, F., Dmitriev, A.I., Ertz, M., Knothe, K., Popov, V.L., Psakhie, S.G. and Shilko, E.V. (2006), “Multiscale simulation of dry friction in wheel/rail contact”, Wear, 261, 7-8, 874-884.

[27] Reynolds, O. (1886), “On the Theory of Lubrication and Its Application to Mr. Beauchamp Tower's Experiments, Including an Experimental Determination of the Viscosity of Olive Oil”, Philosophical Transactions of the Royal Society of London, 177, 157-234.

[28] Stribeck, R. (1902), “Die wesentlichen Eigenschaften der Gleit- und Rollenlager”, VDI-Zeitschrift 46, pp. 1341-1348, 1432-1438 and 1463-1470.

[29] Dowson, D. (1979), "History of Tribology", Printed by Longman Group Limited, London, 677 pages.

[30] Beagley, T.M. (1976), "The rheological properties of solid rail contaminants and their effects on wheel/rail adhesion", Proc. Inst. Mech. Eng. 190, 419-428.

[31] Baglin, K.P. and Archard, J.F. (1972), "An analytic solution of the elastohydrodynamic lubrication of materials of low elastic modulus", Proc. 2nd Symp. on Elastohydrodynamic Lubrication, Institution of Mechanical Engineers, London, C3.

[32] Wolveridge, P.E., Baglin, K.P. and Archard, J.F. (1971), "The starved lubrication of cylinders in line contact", Proc. Inst. Mech. Eng. 181, 1159-1169.

[33] Tomberger, C., Dietmaier, P., Sextro, W. and Six, K. (2009), "Friction in wheel-rail contact: a model comprising interfacial fluids, surface roughness and temperature", 8th International Conference on Contact Mechanics and Wear of Rail/Wheel Systems (CM2009), Firenze, Italy, September 15-18.

[34] Gelinck, E.R.M. and Schipper, D.J. (2000), "Calculation of Stribeck Curves for line contacts", Tribology International 33, 175-181.

[35] Liu, Q., Napel, W., Tripp, J.H., Lugt, P.M. and Meeuwenoord, R. (2009) "Friction in highly loaded mixed lubricated point contacts", Tribology Transactions 52, 3, 360-369.

[36] Greenwood, J.A. and Williamson, J.B.P. (1966), "Contact of nominally flat surfaces", Phil Trans R Soc London, Series A, 295, 300-319.

[37] Moes, H. (2000), "Lubrication and Beyond", lecture notes, University of Twente, Enschede, NL, www.tr.ctw.utwente.nl/research/publications.

[38] Faraon, I.C. (2005), "Mixed lubricated line contacts", Ph.D. Thesis, University of Twente, Enschede, The Netherlands.

[39] Zhao, Y., Maietta, D.M. and Chang, L. (2000), "An asperity microcontact model incorporating the transition from elastic deformation to fully plastic flow", ASME Journal of Tribology 122, 86-93.

[40] Johnson, K.L., Greenwood, J.A. and Poon, S.Y. (1972), "A simple theory of asperity contact in elastohydrodynamic lubrication", Wear 19, 91-108.

[41] Dowson, D. and Higginson, G.R. (1966), "Elasto-hydrodynamic lubrication - The fundamentals of roller and gear lubrication", Pergamon Press, Oxford.

[42] Nijenbaning, G., Venner, C.H. and Moes, H. (1994), "Film thickness in elastohydrodynamically lubricated elliptic contacts", Wear 176, 217–229.

[43] Roelands, C.J.A. (1966), "Correlation aspects of the viscosity - temperature -

pressure relationship of lubricated oils", Ph.D. thesis, Technische Hogeschool Delft, The Netherlands.

[44] Rooij, M.B. (1998), "Tribological aspects of unlubricated deepdrawing processes", Ph.D. thesis, University of Twente, Enschede, The Netherlands.

[45] Schipper, D.J. (1988), "Transitions in the Lubrication of Concentrated Contacts", Ph.D. thesis, University of Twente, Enschede, The Netherlands.

[46] Gelinck, E.R.M. (1999), "Mixed lubrication of line contacts", PhD thesis, University of Twente Enschede, The Netherlands.

[47] Blok, H. (1937), "Surface temperature under extreme pressure lubricating conditions", Proc. Second World Petroleum Cong. 3, 471 - 486.

[48] Johnson, K.L. and Greenwood, J.A. (1980), "Thermal analysis of an Eyring fluid in elastohydrodynamic traction", Wear 61, 353 - 374.

[49] Bos, J. and Moes, H. (1995), "Frictional Heating of Tribological Contacts", Journal of Tribology, 117, 171 - 177.

[50] Greenwood, J.A. and Kauzlarich, J.J. (1973), "Inlet shear heating in elastohydrodynamic lubrication", Transactions of the ASME, Journal of Lubrication Technology, 95, 417 - 426.

[51] Pandey, R.K. and Ghosh, M.K. (1996), "Thermal effects of film thickness and traction in rolling/sliding EHL line contacts – an accurate inlet zone analysis", Wear 192, 118 - 127.

[52] Barwell, F.T. (1987), "Thermal aspects of lubrication of concentrated contacts", Tribology International, Vol. 20, No. 3, 114 - 118.

[53] Wilson, W.R.D. and Sheu, S. (1983), "Effect of inlet shear heating due to sliding on elastohydrodynamic film thickness", Journal of Lubrication Technology, 105, 187 - 188.

[54] Faraon, I.C. and Schipper, D.J. (2007), "Stribeck curves for starved line contacts", Journal of Tribology 129, 181-187.

[55] Chevalier, F., Lubrecht, A.A., Cann, P.M.E., Colin, F. and Dalmaz, G. (1998), "Film thickness in starved EHL point contacts", Journal of Tribology 120, 126-133.

[56] Dowson, D. and Higginson, G.R. (1959), "A numerical solution to the elasto-hydrodynamic problem", J. of mech. Eng. Science, vol. 1, no. 1, 22-35.

[57] Damiens, B., Venner, C.H., Cann, P.M.E. and Lubrecht, A.A. (2004), "Starved lubrication of elliptical EHD contacts", Journal of Tribology 126, 105-111.

[58] Chittenden, R.J., Dowson, D., Dunn, J.F. and Taylor, C.M. (1985), "A theoretical analysis of the isothermal elastohydrodynamic lubrication of

concentrated contacts I. Direction of lubricant entrainment coincident with the major axis of the Hertzian contact ellipse", Proc. Roy. Soc. London, A, 397, 1813, 245-269.

[59] Chittenden, R.J., Dowson, D., Dunn, J.F. and Taylor, C.M. (1985), "A theoretical analysis of the isothermal elastohydrodynamic lubrication of concentrated contacts II. General case, with lubricant entrainment along either principal axis of the Hertzian contact ellipse or at some intermediate angle", Proc. Roy. Soc. London, A, 397, 1813, 271-294.

[60] Hamrock, B. J. and Dowson, D. (1977), "Isothermal Elastohydrodynamic Lubrication of Point Contacts, Part 3 - Fully Flooded Results", ASME Jour. of Lubr. Tech., 99, 264-276.

[61] Popovici, G. (2005), "Effects of lubricant starvation on performance of elasto-hydrodynamically Lubricated contacts", Ph.D. Thesis, University of Twente, Enschede, The Netherlands.

[62] Poon, S.Y. and Haynes, D.J. (1966), "Frictional behaviour of lubricated rolling-contact elements", Proc. Instn Mech. Engrs, Vol. 181, Pt. 1, No. 16, 363-389.

[63] Johnson, K.L. and Tevaarwerk, J.L. (1977), "Shear Behaviour of Elastohydrodynamic Oil Films", Proc. R. Soc. Lond., A, 356, 1685, 215-236.

[64] Fulford, C.R. (2004), "Review of low adhesion research", Report: CRF04002, Issue 1, Rail Safety and Standards Board.

[65] www.salientsystems.com

[66] Harrison, H., McCanney, T. and Cotter, J. (2002), "Recent developments in coefficient of friction measurements at the rail/wheel interface", Wear, 253, 114-123;

[67] www.portecrail.com

[68] Clem, G.K. (2001), "Tribometer for testing the efficiency of lubrication upon a railroad track surface", Patent No US 6,192,736 B1.

[69] Watkins, D.J. (1975), "Exploring adhesion with British Rail's tribometer train", Railway Eng. J., Vol. 4, No. 4, 6-13.

[70] www.kajo.de

[71] www.pph.wur.nl

[72] www.iris-vision.nl

[73] www.mathworks.com/products/matlab

[74] Savitzky, A. and Golay, M. J. E. (1964), "Smoothing and Differentiation of Data by Simplified Least Squares Procedures", Analytical Chemistry, 36 (8), pp 1627-1639.

[75] Botev, Z.I., Grotowski, J.F. and Kroese, D.P. (2009), "Kernel density estimation via diffusion", submitted to the Annals of Statistics.

[76] Popovici, R.I. and Schipper, D.J. (2008), "Modelling contact phenomena and those influenced by greases", presented at the 20th ELGI AGM April 2008, Lisbon – Portugal, published in Eurogrease ian/feb/mar 2009.

[77] Johnson, K.L. and Roberts, A.D. (1974), "Observations of viscoelastic behaviour of an elastohydrodynamic lubricant film", Proc. Roy. Soc. London, Series A, Vol. 337, No. 1609, 217-249.

[78] Bair, S. and Winer, W.O. (1979), "A rheological model for elastohydrodynamic contacts based on primary laboratory data", Journal of Lubrication Technology, 101, 258-265.

[79] Gecim, B. and Winer, W.O. (1980), "Lubricant limiting shear stress effect on EHD film thickness", Journal of Lubrication Technology 102, 213-221.

[80] Elsharkawy, A.A. and Hamrock, B.J. (1991), "Subsurface stresses in micro-EHL line contacts", Journal of Tribology 113, 645-657.

[81] Olaru, D.N. (2002), "Fundamente de lubrificatie", ISBN 973 8292 02 6, Edit. "Gh. Asachi", Iasi, Romania.

[82] Barus, C. (1893), "Isothermals, isopiestics and isometrics relative to viscosity", American Journal of Science 45, 87-96.

[83] Yasutomi, S., Bair, S. and Winer, W.O. (1984), "An application of a free volume model to lubricant rheology 1 – Dependence of viscosity on temperature and pressure", Journal of Tribology 106, 291-303.

[84] Sloetjes, J.W. (2006), "Micro-Elastohydrodynamic Lubrication in Concentrated Sliding Contacts" PhD thesis, University of Twente, the Netherlands.

[85] Briscoe, B.A. and Tabor, D. (1973), "Rheology of thin organic films", ASLE Transactions, 17, 3, 158-165.

[86] Reussner, H. (1977), "Druckflächenbelastung und Oberflächen Verschiebung im Wälzcontact von Rotationskörpen", Ph.D. Thesis University of Karlsruhe, Germany (in German).

[87] Take home project: FMN100-03, "Numerisk Analys för datorgrafik", Numerical Analysis, Centre for Mathematical Sciences, Lunds Universitet.

[88] Press, W.H., Flannery, Teukolsky, S.A. and Vetterling, W.T. (1992), "Numerical Recipes: the art of scientific computing. 2nd ed.", Cambridge University Press.